

## ABSTRACT

Title of Document: HETEROGENEOUS ORDERED  
MESOPOROUS CARBON/METAL OXIDE  
COMPOSITES FOR THE  
ELECTROCHEMICAL ENERGY STORAGE

Junkai Hu, Doctor of Philosophy, 2015

Directed By: Professor Sang Bok Lee, Department of  
Chemistry and Biochemistry

The combination of high electronic conductivity, enhanced ionic mobility, and large pore volume make ordered mesoporous carbons (OMCs) promising scaffolds for active energy storage materials. However, mesoporous structures and material morphology need to be more thoroughly addressed. This dissertation discusses the effects of mesoporous structures and material morphologies on the electrochemical performance of OMC/Fe<sub>2</sub>O<sub>3</sub> composites. In the first approach, Fe<sub>2</sub>O<sub>3</sub> was embedded into 1D cylindrical (FDU-15), 2D hexagonal (CMK-3), and 3D bicontinuous (CMK-8) symmetries of mesoporous carbons. These materials were used as supercapacitors for a systematic study of the effects of mesoporous architecture on the structure stability, ion mobility, and performance of mesoporous composite electrodes. The results show that the CMK-3 and CMK-8 synthesized by hard template method can provide high pore volume, but the instability of their mesostructures hinders the total electrode

performances upon oxide impregnation. In contrast, the FDU-15 from the soft template method can provide a stable mesostructure. However, it contains much smaller pore volume and surface area, leading to limited metal oxide loading and electrode capacitance. Based on these results, anodized aluminum oxide (AAO) and triblock copolymer F127 are used together as hard and soft templates to fabricate ordered mesoporous carbon nanowires (OMCNW) as a host material for  $\text{Fe}_2\text{O}_3$  nanoparticles. The synergistic effects in the dual template strategy provide a high pore volume and surface area, and the structure remains stable even with high metal oxide loading amounts. Additionally, the unique nanowire morphology and mesoporous structure of the OMCNW/ $\text{Fe}_2\text{O}_3$  facilitate high ionic mobility in the composite, leading to a large capacitance with good rate capability and cycling stability. I further evaluated this OMCNW/ $\text{Fe}_2\text{O}_3$  as a lithium-ion battery (LIB) anode, which showed that the porous symmetry, material morphology, and structure stability are even more important in the rate and cycling performances of LIBs. This work helps further the understanding and optimization of porous structures and morphologies of heterogeneous composites for next generation electrochemical energy storage materials.

HETEROGENEOUS ORDERED MESOPOROUS CARBON/METAL OXIDE  
COMPOSITES FOR THE ELECTROCHEMICAL ENERGY STORAGE

By

Junkai Hu

Dissertation submitted to the Faculty of the Graduate School of the  
University of Maryland, College Park, in partial fulfillment  
of the requirements for the degree of  
Doctor of Philosophy  
2015

Advisory Committee:  
Professor Sang Bok Lee, Chair  
Professor Neil Blough  
Professor Kyu Yong Choi  
Professor Bryan Eichhorn  
Professor YuHuang Wang

© Copyright by  
Junkai Hu  
2015

## **Dedication**

I would like to dedicate this dissertation to my parents and wife for their endless support.

## Acknowledgements

First and foremost, I am sincerely grateful to my advisor, Professor Sang Bok Lee, for his guidance and support throughout my graduate career. I truly appreciate his kindness and patience when I was struggling in my research. It was under his directing and encouragement that I learned how to think scientifically. His passion in science and open mind to new ideas continue inspiring me to pursue further in my projects.

I would like to thank Dr. Malachi Noked and Eleanor Gillette for their help to edit my papers, without you, this dissertation will be completely different. I would like to thank Dr. Sung Kyoung Kim for his warmly welcome when I enter the group. I would like to thank Stefanie Sherrill Wittenberg for her always answer my questions with smiles. I would like to thank Liz Nguyen for organizing happy hours and teach me the difference between beers. I would like to thank Jonathon Duay for valuable discussions regarding electrochemistry and Utah. I would like to thank Zhe Gui for her kindness helps in my experiments. I would like to thank Lauren Graham to share valuable information as a same year graduate student. I would like to thank Jaehee Song for teaching me Korea, especially how to write my name. I would like to thank Nikki Schneck for her passion for everything and told me my brake pads need to be changed. I would like to thank Nam Kim for his encouraging during my dissertation writing. I would like to thank Dongheun (Tony) Kim for the new bug-free microwave. I would like to thank Emily Sahadeo for proof reading of my desertation. I would like to thank Yang Wang for sharing his insteresting life through weichat.

I would like to thank Professor Gary Rubloff and his group for providing me many useful feedbacks in the joint group meeting. I would like to thank Professor Chunsheng Wang, Professor Yuhuang Wang, Professor Bryan Eichhorn, and Professor Zhihong Nie for their admittance to using their groups' instruments. I would like to thank Dr. Chuanfu Sun and Fudong Han for their collaborations in my projects.

I would like to thank my parents for their support throughout my life. And last but not least, I would like to thank my wife, Xiaocui, for her patient and support during these years.

## Table of Contents

<b>Dedication .....</b>	<b>ii</b>
<b>Acknowledgements .....</b>	<b>iii</b>
<b>Table of Contents .....</b>	<b>v</b>
<b>List of Tables.....</b>	<b>viii</b>
<b>List of Figures.....</b>	<b>ix</b>
<b>Abbreviations .....</b>	<b>xi</b>

### **Chapter 1 Ordered Mesoporous Carbon Based Heterogeneous Composites: Preparation and Application in Electrochemical Energy Storage .....**

<b>1.1 Introduction.....</b>	<b>2</b>
1.1.1 Background for Electrical Energy Storage Systems.....	2
1.1.2 Supercapacitors .....	3
1.1.3 Lithium-ion batteries.....	6
1.1.4 Ordered mesoporous carbon-based composite for electrochemical energy storage .....	7
<b>1.2 Synthetic strategies for OMC based composites .....</b>	<b>9</b>
1.2.1 Direct precipitation .....	13
1.2.2 Impregnation-decomposition .....	14
1.2.3 Surface reduction .....	17
1.2.4 Melt-diffusion .....	17
1.2.5 <i>In situ</i> polymerization .....	18
1.2.6 Co-polymerization .....	19
<b>1.3 Electrochemical energy storage of OMC based composites.....</b>	<b>22</b>
1.3.1 Supercapacitors .....	22
1.3.1.1 OMC/metal oxides .....	26
1.3.1.2 OMC/conducting polymers.....	28
1.3.2 Lithium-ion batteries.....	29
1.3.2.1 Anodic materials .....	30
1.3.2.2 Cathodic materials .....	34

### **Chapter 2 Capacitance Behavior of Ordered Mesoporous Carbon/Fe<sub>2</sub>O<sub>3</sub> Composites: Comparison Between 1D Cylindrical, 2D Hexagonal, and 3D Bicontinuous Mesostructures.....**

<b>2.1 Introduction.....</b>	<b>38</b>
<b>2.2 Experiment section.....</b>	<b>40</b>
2.2.1 Materials Preparation.....	40
2.2.2 Characterization.....	43

2.2.3 Electrochemical Measurement.....	44
2.3 Results and discussions.....	45
2.3.1 Structural and Textural Characterization of different structures OMC/Fe <sub>2</sub> O <sub>3</sub> composites.....	45
2.3.2 Electrochemical studies of different structures of OMC/Fe <sub>2</sub> O <sub>3</sub> composites.....	53
2.3.2.1 Electrochemical impedance spectroscopy (EIS) studies of mesostructure's influence on ion mobility.....	53
2.3.2.2 Influence of mesostructure on capacitance performance – electrochemical behavior of bare mesoporous carbons.....	57
2.3.2.3 Influence of mesostructure stability on capacitance performance – electrochemical behavior of OMC with loading of Fe <sub>2</sub> O <sub>3</sub> .....	59
2.4 Conclusion .....	65
<b>Chapter 3 Dual-Template Synthesis of Ordered Mesoporous Carbon/Fe<sub>2</sub>O<sub>3</sub>Nanowires: High Porosity and Structural Stability for Supercapacitors.....</b>	<b>66</b>
3.1 Introduction.....	67
3.2 Materials and Methods.....	70
3.2.1 Materials Preparation.....	70
3.2.2 Characterization.....	71
3.2.3 Electrochemical Measurement.....	72
3.3 Results and Discussions.....	73
3.3.1 Morphological and Structural Characterization.....	73
3.3.2 Electrochemical Studies on ion transportation and capacitance performances.....	83
3.4 Conclusions.....	90
<b>Chapter 4 Dual-Template Ordered Mesoporous Carbon/Fe<sub>2</sub>O<sub>3</sub> Nanowires as Lithium-Ion Batteries Anodes.....</b>	<b>92</b>
4.1 Introduction.....	93
4.2 Experiment Sections .....	97
4.2.1 Materials Preparation.....	97
4.2.2. Characterization.....	99
4.2.3 Electrochemical Measurements .....	100
4.3 Results and Discussions.....	101
4.3.1 Morphological and Structural Characterization.....	101
4.3.2 Electrochemical performance as anode materials of LIBs .....	109
4.4 Conclusions.....	119

<b>Chapter 5 Summary and Outlook.....</b>	<b>121</b>
<b>Publications .....</b>	<b>125</b>
<b>References .....</b>	<b>126</b>

## List of Tables

### Chapter 1

Table 1. 1 Representative chemical of physical reactions in different guest nanoparticle loading methods .....	11
Table 1. 2 OMC based hybrid materials for supercapacitors.....	23
Table 1. 3 OMC based hybrid materials for LIBs anode .....	31
Table 1. 4 MC based hybrid materials for LIBs cathode .....	34

### Chapter 2

Table 2. 1 N <sub>2</sub> adsorption–desorption properties of OMCs & OMC/Fe <sub>2</sub> O <sub>3</sub> composites.....	49
Table 2. 2 EIS parameters for different OMCs & OMC/Fe <sub>2</sub> O <sub>3</sub> composites .....	56

### Chapter 3

Table 3. 1 N <sub>2</sub> adsorption-desorption properties of OMCs composites .....	77
Table 3. 2 Mesopore volume change in OMCs & OMC/Fe <sub>2</sub> O <sub>3</sub> composites.....	81
Table 3. 3 Comparison of the electrochemical performance of iron oxide related nanomaterials .....	86
Table 3. 4 EIS parameters for different OMC/Fe <sub>2</sub> O <sub>3</sub> composites .....	88
Table 3. 5 Structural properties and electrochemical performance comparison of OMCs from different synthetic strategies as host materials of Fe <sub>2</sub> O <sub>3</sub> .....	90

### Chapter 4

Table 4. 1 N <sub>2</sub> adsorption-desorption properties of OMCs & OMC/Fe <sub>2</sub> O <sub>3</sub> composites.....	107
Table 4. 2 Estimated volume changes during lithiation process in OMC/Fe <sub>2</sub> O <sub>3</sub> composites.....	117

## List of Figures

### Chapter 1

Figure 1. 1 Schematic illustrations for different electrochemical energy storage devices.....	4
Figure 1. 2 Ragone Plot of capacitors and LIBs. ....	7
Figure 1. 3 Two strategies for the future energy storage devices.....	8
Figure 1. 4 Problems of nanomaterials and the corresponding solution.....	9
Figure 1. 5 Synthetic processes of the soft template method and the hard template method.....	10
Figure 1. 6 Different OMC structures.....	11
Figure 1. 7 Schematic illustrations for different strategies to embed guest nanoparticles into OMCs. ....	12

### Chapter 2

Figure 2. 1 Synthesis processes of FDU-15, CMK-3, and CMK-8 .....	41
Figure 2. 2 XPS spectrums of OMC/Fe <sub>2</sub> O <sub>3</sub> composites .....	46
Figure 2. 3 N <sub>2</sub> adsorption–desorption isotherms and pore size distributions of OMCs and their derived composites.....	47
Figure 2. 4 TEM images of different meso-structures OMCs & OMC/Fe <sub>2</sub> O <sub>3</sub> composites.....	50
Figure 2. 5 Schematic illustration of different mesostructure stabilities .....	51
Figure 2. 6 Nyquist plots and Bode plots for different OMCs and their composites .....	54
Figure 2. 7 Cyclic Voltammetry curves and specific capacitances of different OMCs and their derived composites.....	58
Figure 2. 8 CV curve and Specific capacitance of mesoporous Fe <sub>2</sub> O <sub>3</sub> .....	59
Figure 2. 9 Specific capacitance of OMCs, OMC/Fe <sub>2</sub> O <sub>3</sub> composites, and calculated capacitance of Fe <sub>2</sub> O <sub>3</sub> .....	61
Figure 2. 10 Cycling performances of FDU-15-20.0, CMK-3-19.7, and CMK-8-21.4 in 1 M Na <sub>2</sub> SO <sub>3</sub> solution at current density of 5 A g <sup>-1</sup> . ....	64

### Chapter 3

Figure 3. 1 Synthesis processes of OMCNW .....	71
Figure 3. 2 SEM images of different OMCs & OMC/Fe <sub>2</sub> O <sub>3</sub> composites with distinct morphologies.....	74
Figure 3. 3 TEM images of different mesostructures OMCs & OMC/Fe <sub>2</sub> O <sub>3</sub>	

composites.....	75
Figure 3. 4 N <sub>2</sub> adsorption-desorption isotherms and pore size distributions of OMCNW, FDU-15, CMK-8 and their derived Fe <sub>2</sub> O <sub>3</sub> composites.....	76
Figure 3. 5 Pore sizes and pore wall thickness of FDU-15 and OMCNW annealed at different temperatures. ....	79
Figure 3. 6 Schematic illustration of different mesostructure evolutions for mesoporous carbon synthesized with & without AAO.....	80
Figure 3. 7 XPS spectrums of OMC/Fe <sub>2</sub> O <sub>3</sub> composites .....	82
Figure 3. 8 CV curves, rate performance, and Nyquist plots for different mesostructured OMCs and OMC/Fe <sub>2</sub> O <sub>3</sub> composites.....	84
Figure 3. 9 Cycling performance of different OMC/Fe <sub>2</sub> O <sub>3</sub> composites .....	89

## Chapter 4

Figure 4. 1 XRD patterns, Raman Spectra, and XPS spectra of OMC/Fe <sub>2</sub> O <sub>3</sub> composites.....	102
Figure 4. 2 SEM images of different morphologies in OMCs and OMC/Fe <sub>2</sub> O <sub>3</sub> composites without HNO <sub>3</sub> treatment.....	103
Figure 4. 3 TEM images of different mesostructured OMCs and OMC/Fe <sub>2</sub> O <sub>3</sub> composites without HNO <sub>3</sub> treatment .....	104
Figure 4. 4 N <sub>2</sub> adsorption-desorption isotherms and Pore size distributions of OMCs and OMC/Fe <sub>2</sub> O <sub>3</sub> composites .....	106
Figure 4. 5 CV and GV curves of OMCNW/Fe <sub>2</sub> O <sub>3</sub> .....	109
Figure 4. 6 Rate capability, Nyquist plots, equivalent circuit, and Cycling performances of OMC/Fe <sub>2</sub> O <sub>3</sub> composites.....	110
Figure 4. 7 Comparison of rate performance in different structures OMCs.....	113
Figure 4. 8 Cycling performance of FDU-15, CMK-8, and OMCNW.....	116
Figure 4. 9 TEM images of different OMC/Fe <sub>2</sub> O <sub>3</sub> composites after 500 cycles at a current density of 0.5 A g <sup>-1</sup> .....	119

## Chapter 5

Figure 5. 1 Comparison of structure and electrochemical properties of OMCs from different synthesis strategies. ....	124
--	-----

## Abbreviations

AAO: anodic aluminum oxide

BET: Brunauer–Emmett–Teller

BJH: Barrett–Joyner–Halenda

CE: Coulombic efficiency

$C_{\text{int}}$ : intercalation capacitance

$CPE_{\text{ct}}$ : constant phase element for charge transfer process

CMK-3: carbon mesostructure from Korea, No. 3

CMK-5: carbon mesostructure from Korea, No. 5

CMK-8: carbon mesostructure from Korea, No. 8

CV: cyclic voltammetry

DMC: dimethyl carbonate

EC: ethylene carbonate

EDLC: electric double layer capacitors

EIS: electrochemical impedance spectroscopy

FDU-14: the 14<sup>th</sup> OMC discovered by Fudan University

FDU-15: the 15<sup>th</sup> OMC discovered by Fudan University

FDU-16: the 16<sup>th</sup> OMC discovered by Fudan University

F127: triblock copolymer Pluronic F127 ( $EO_{106}PO_{70}EO_{106}$ , MW=12600)

GMC: graphitic mesoporous carbon

GV: galvanostatic voltammetry

HRTEM: high-resolution transmission electron microscopy

ICP-AES: inductively coupled plasma-atomic emission spectroscopy

KIT-6: the 6<sup>th</sup> OMC discovered by Korea Advanced Institute of Science and Technology

LIB: lithium-ion battery

MO: metal oxide

NMP: N-Methyl-2-pyrrolidone

OMC: ordered mesoporous carbons

OMCNW: ordered mesoporous carbon nanowire

PANI: Polyaniline

PPy: polypyrrole

PVDF: poly-(vinylidene fluoride)

$R_s$ : solution resistance

$R_{ct}$ : charge transfer resistance

SBA-15: the 15<sup>th</sup> OMC discovered by University of California, Santa Barbara

SEI: solid electrolyte interface

SEM: scanning electron microscopy

$S_t$ : total surface area

TEM: transmission electron microscopy

TEOS: tetraethyl orthosilicate

$V_{meso}$ : mesopore ( $2 \text{ nm} < d < 50 \text{ nm}$ ) volume

$V_{micro}$ : micropore ( $d < 2$  nm) volume

$V_t$ : total pore volume

$\Delta V_{meso}$ : normalized mesopore volume change after  $Fe_2O_3$  loading based on original carbon mass

$\Delta V_t$ : total volume expansion

XPS: X-ray photoelectron spectroscopy

XRD: X-ray diffraction

$Z_w$ : Warburg impedance

$\tau$ : time constant

## **Chapter 1**

# **Ordered Mesoporous Carbon Based Heterogeneous Composites: Preparation and Application in Electrochemical Energy Storage**

## 1.1 Introduction

### 1.1.1 Background for Electrical Energy Storage Systems

With the huge consumption, limited reserves, and environmental issues associated with fossil fuels, the development of clean and renewable energy sources has gained a worldwide interest in the past decade. These novel energies, such as solar, wind and tidal energies, will eventually be transferred to electrical energy, which is the primary consumed energy form. However, the productions of these novel energies are not continuous because of the variation of natural conditions such as solar angle and wind power. On the other hand, the consumption of electricity is much larger during the day than at night, which will generate on-peak and off-peak fluctuations in energy. Therefore, high-performance energy storage devices are required for the stable and efficient utility of the next generation energies.

There are two important parameters which are usually used to compare the performance of electrical energy storage devices: the energy density and the power density. The former reveals how much energy can be stored in the device, while the latter reflects how fast that energy can be drained. These two parameters can be calculated as follows:

$$E_d = \frac{i \int V dt}{m} \quad (1.2)$$

$$P_d = \frac{E_d}{t} \quad (1.3)$$

where  $E_d$  is the energy density (in Wh kg<sup>-1</sup>),  $i$  is current,  $V$  is the maximal

potential difference applied to the electrodes,  $m$  is total mass,  $P_d$  is power density (in W kg<sup>-1</sup>), and  $t$  is charge/discharge time.

Depending on the device type, the energy density varies from 0.01 to 1,000 Wh kg<sup>-1</sup>, while the power density varies from 10 to 10,000 W kg<sup>-1</sup>. Among various energy storage systems, supercapacitors and lithium-ion batteries (LIBs) are the most promising devices. They have been widely applied in daily life, such as cell phones, laptops, and electric or hybrid vehicles. This widespread uses are due to their competitive energy and power densities. Despite that these two devices sometimes uses similar electrode materials (*i. e.* carbon, MnO<sub>2</sub>, Fe<sub>2</sub>O<sub>3</sub>, *etc.*), their charge storage mechanisms and electrochemical performances are quite different.

### 1.1.2 Supercapacitors

The conventional capacitor is made of two conductive plates separated by a dielectric media, as shown in Figure 1.1a. When a potential difference is applied to the two plates, positive and negative charges will be accumulated on different surfaces. For a given capacitor, the amount of charge ( $q$ ) is proportional to the potential applied ( $V$ ). Their ratio  $dq/dV$  is known as the capacitance ( $C$ ) of the capacitor. The unit of capacitance is farad (F), which represents a coulomb per volt. The capacitance of each capacitor is constant. For a simple parallel capacitor, the capacitance can be calculated from the following equation:

$$C = \frac{\epsilon_r \epsilon_0 A}{d} \quad (1.3)$$

Where  $\epsilon_r$  is the relative permittivity of dielectric media,  $\epsilon_0$  is the vacuum permittivity constant with the value of  $8.854 \times 10^{-12} \text{ F m}^{-1}$ ,  $A$  is the overlapped plate size, and  $d$  is the distance between two plates.

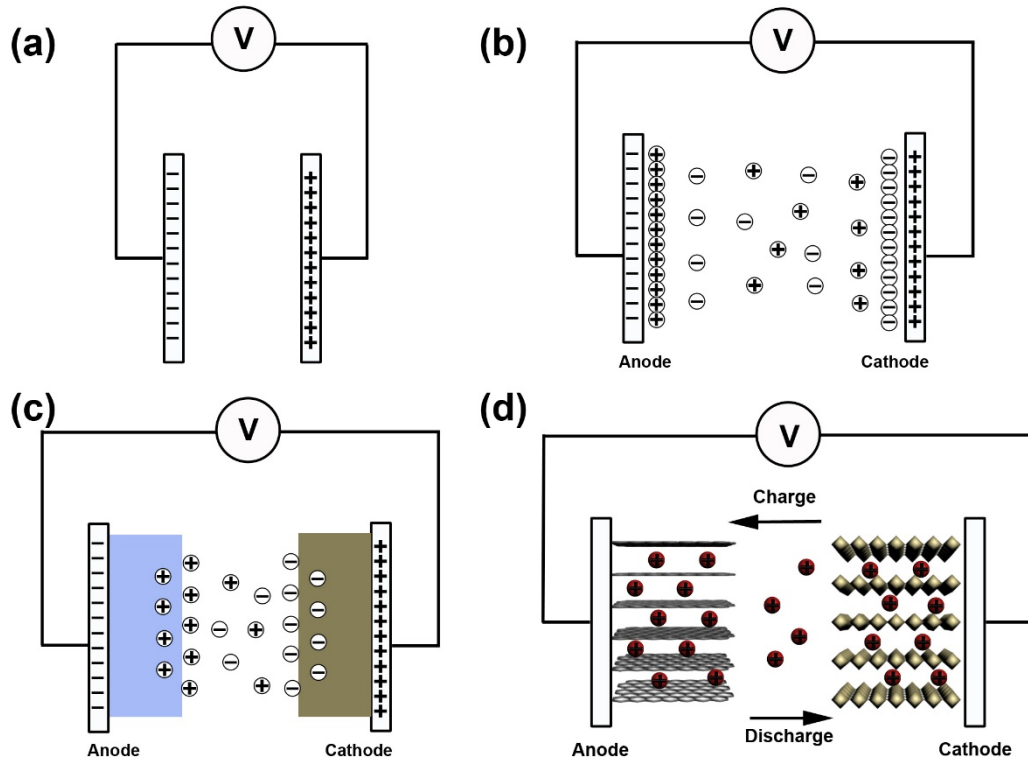


**Figure 1. 1 Schematic illustrations for different electrochemical energy storage devices.**

(a) conventional capacitor, (b) electric double layer capacitor, (c) pseudocapacitor, (d) Lithium-ion battery (The counter ions were neglected).

Due to the limited area, and large distance, the capacitance of a traditional capacitor is normally lower than  $10^{-2} \text{ F}$ , which cannot meet the requirements in many fields such as microelectronics and hybrid heavy duty platforms<sup>1</sup>. Therefore, electrochemical capacitors with much higher capacitance values were designed. The electrochemical capacitors are also called supercapacitors or ultracapacitors, and can

be categorized into electric double layer capacitors (EDLCs) and pseudocapacitors based on different charge storage mechanisms.

The EDLC is made of two high surface area electrodes separated by the electrolyte. The charge is stored by the charge separation at the electrode/electrolyte interface. The charge storage mode of EDLCs is similar to a conventional capacitor. However, in EDLCs, the  $d$  is the thickness of the double layer, which is typically only a few Angstroms for the aqueous electrolyte, and the area  $A$  can reach  $1000 \text{ m}^2 \text{ g}^{-1}$ . Hence, the EDLCs can present  $200 \text{ F g}^{-1}$  specific capacitance, which is several orders of magnitude higher than the traditional capacitors.<sup>2</sup>

The pseudocapacitors are usually made of metal oxides and conducting polymers. As shown in Figure 1.1b, the charge is stored by fast surface Faradaic processes which involves surface ion adsorption and insertion.<sup>3-5</sup> Since the near surface atoms are used for ion insertion, the capacitance of pseudocapacitors can achieve an even higher capacitance than EDLCs.<sup>6-8</sup>

Since the surface ion adsorption-desorption or the surface reaction processes are very fast, the charge and discharge rates in supercapacitors are normally very high. Therefore, supercapacitors can achieve very high power densities. However, because the reactions only take place near the surface, the energy densities of the supercapacitors are limited by their surface area and are typically smaller than batteries.

### 1.1.3 Lithium-ion batteries

LIB was first discovered and commercialized by SONY in the early 1990s by replacing the traditional lithium anode with graphite anode. This replacement greatly improved the safety and cell life, and made the LIB the most widely used secondary battery. A LIB is mainly composed of a negative lithium intercalation material (anode), a positive lithium intercalation material (cathode), an electrolyte, and a separator. During charge-discharge processes, the  $\text{Li}^+$  exchanges between the cathode and anode. Therefore, LIB is also referred as “rocking-chair battery” since the  $\text{Li}^+$  moves back and forth between two electrodes.

The cathode materials are often made of lithium-containing compound such as  $\text{LiMO}_2$  (M: Mn, Co, or Ni),  $\text{LiMPO}_4$  (M: Fe or Mn), or  $\text{LiMSiO}_4$  (M: Fe, Co, or Mn). The anode materials are typically carbon materials (*i. e.* graphite, graphene, carbon nanotubes, porous carbons *etc.*), metal oxide (*i. e.*  $\text{Fe}_2\text{O}_3$ ,  $\text{MnO}_2$ ,  $\text{NiO}$ , *etc.*), and metal or semiconductor (*i. e.* Si, Sn, *etc.*). The  $\text{Li}^+$  ions insert-desert at distinct voltages in anode and cathode, thus result in a high voltage in LIB. In addition, the energy storage sites in LIBs are not limited by the exposed electrode surface, which is different with supercapacitors. Since the bulk part can be utilized in  $\text{Li}^+$  insertion-desertion processes, LIBs can achieve higher energy density than supercapacitors. However, as the bulk reaction is much slower than the surface reaction or surface ion adsorption-desorption, the charge-discharge speed of LIB is relatively slower, result in a smaller power density compared with supercapacitors.

### 1.1.4 Ordered mesoporous carbon-based composite for electrochemical

#### energy storage

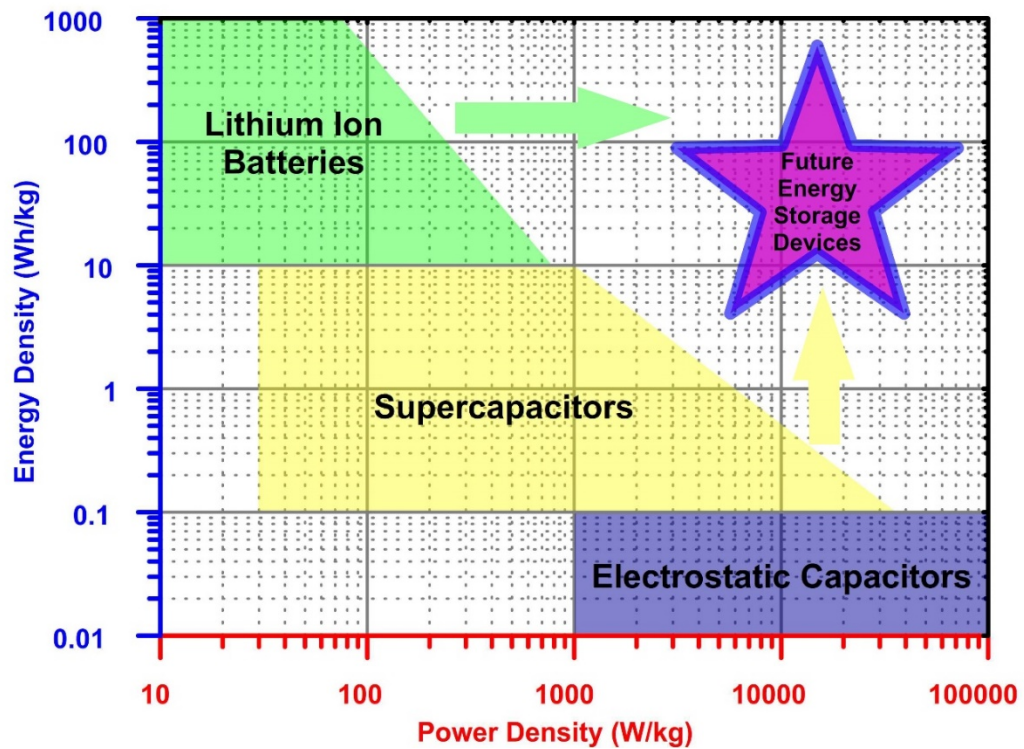
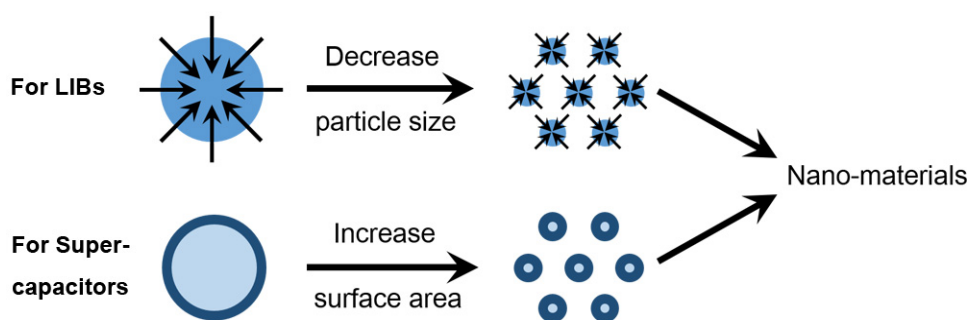


Figure 1. 2 Ragone Plot of capacitors and LIBs.

The difference between supercapacitors and LIBs regarding their energy densities and power densities can be visually seen in the Ragone plot.<sup>9</sup> In Figure 1.1.2, the LIBs with high energy densities but low power densities are located at the top left corner, while the supercapacitors with high power densities but low energy densities are located near bottom right. Future energy storage devices, however, require both high energy density and high power density, which is shown in top right of Ragone plot. As illustrated in Figure 1.3, start with supercapacitors or LIBs, there are two strategies to realize the future energy storage device. The first strategy is to increase the energy

density of supercapacitors. Since the energy stored in supercapacitors is proportional to the surface area, the most direct way to improve their energy density is to increase their surface area. The second strategy is to increase the power density of LIBs. As the lithium insertion-desertion speed is mainly limited by the diffusion length in the materials, decrease particle size is the most effective way to increase the power density of LIBs. Therefore, as shows in Figure 1.2, for both supercapacitors and LIBs, decrease the active materials size to the nanoscale can simultaneously improve their energy density and power density, which has been proved in many previous works.<sup>10, 11</sup>



**Figure 1. 3 Two strategies for the future energy storage devices.**

However, as shown in Figure 1.4 a, b, there are several side effects associated with the decreased particle size. The major problem is the decreased conductivity of the electrode due to the interrupted electron transportation pathways between separated nanoparticles. In addition, the nanoparticles are easier to aggregate during charge-discharge processes, which will hinder the ion transportation and results in unstable cycling performance. To address these problems, heterogeneous host-guest materials have been proposed. In this configuration, the guest nanosized materials are chosen to provide high energy density, while the host materials are designed to supply good

conductivity and ion transportation, and prevent the particle aggregation (Figure 1.4).

This combination ensures a better utilization and stability of the guest materials.

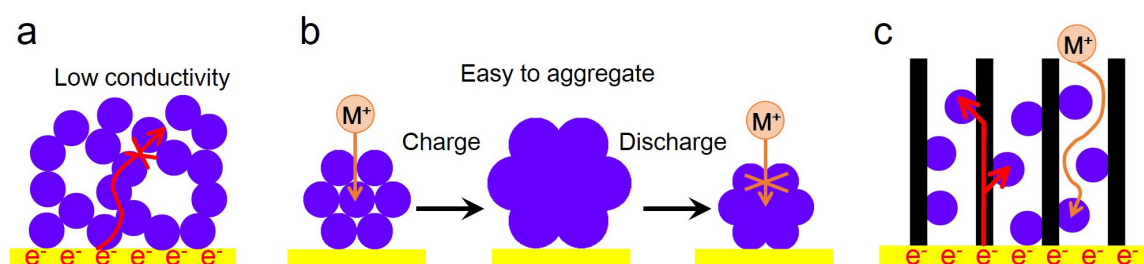


**Figure 1. 4 Problems of nanomaterials and the corresponding solution.**

(a, b) problems of nanomaterials, (c) advantages of host-guest materials.

Among various host materials, ordered mesoporous carbons (OMCs) have drawn much attention not only due to their excellent electrical conductivity, high corrosion resistance, high surface area, and large pore volume, but also due to the facility control of metal oxide nanoparticle size growing inside the well-defined mesopores.<sup>12</sup> In addition, the large volume in OMCs can effectively buffer the volume change of guest nanoparticles, while the carbon framework can prevent the particle aggregation during electrochemical processes – these factors can significantly enhance the cycling performance of the composite materials.<sup>13</sup> Therefore, there are hundreds of works in the literature focused on the OMC based composites for electrochemical energy storage. In the following sections, different synthetic strategies and energy storage applications will be briefly reviewed.

## 1.2 Synthetic strategies for OMC based composites

Until now, various of methods have been used to synthesize different OMCs

(Figure 1.6). Most of them can be categorized in two strategies: the hard template method and the soft template method.<sup>14</sup> The hard template method uses ordered porous solids, (e. g. mesoporous silica,<sup>15</sup> silica colloid,<sup>16</sup> and anodized aluminum oxide (AAO)<sup>17</sup> as the sacrificial mold to cast the carbon replica. The soft template method uses the surfactant, in most cases block copolymers, to form free micelles or liquid crystals as the structure directing agent.<sup>18</sup> Depending on the template and synthesis conditions, different mesostructures (e. g. 3D  $im\bar{3}m$ , Figure 1.6a, 1D  $p6mm$ , Figure 1.6b, and 3D  $ia\bar{3}d$ , Figure 1.6c) can be prepared with distinct pore size distributions. Since there are already many good reviews targeting on the synthesis methods of OMCs,<sup>14, 18,</sup><sup>19</sup> this section will not discuss it in detail. However, I will focus on different incorporation methods to embed guest materials into OMCs.

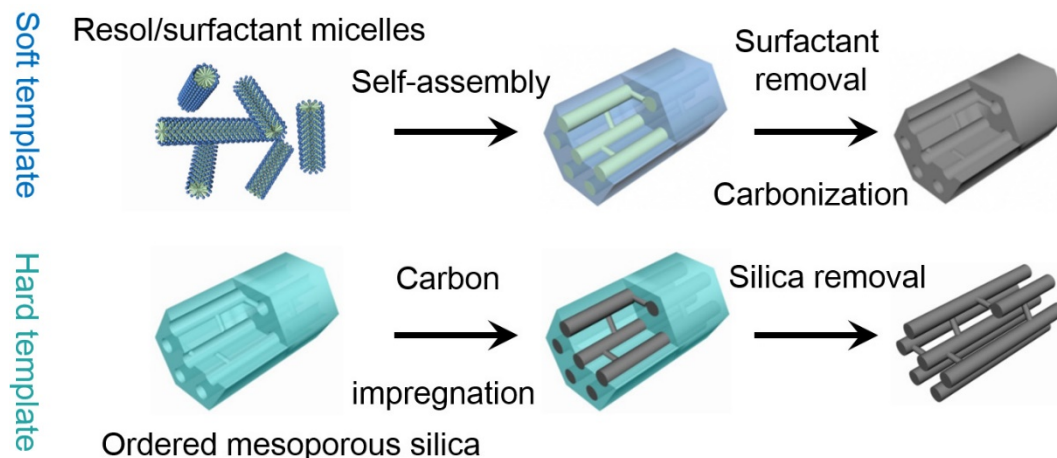


**Figure 1. 5 Synthetic processes of the soft template method and the hard template method.**

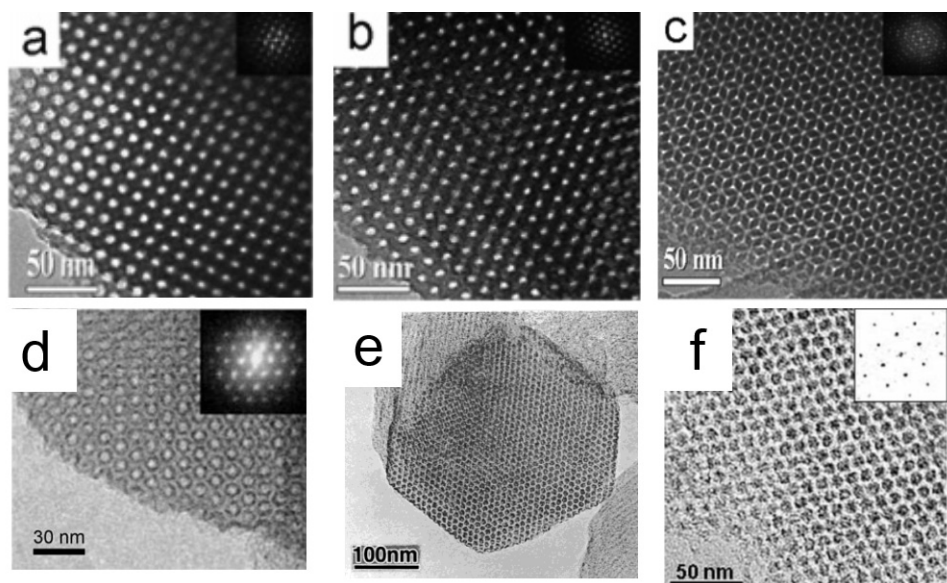


**Figure 1. 6 Different OMC structures.**

(a) FDU-16, (b) FDU-15, (c) FDU-14, (d) CMK-5 (e) CMK-3, (f) CMK-8. (reprinted from reference <sup>20-23</sup>)

**Table 1. 1 Representative chemical of physical reactions in different guest nanoparticle loading methods**

Preparing method	Reactions <sup>#</sup>
Direct precipitation	$M^{x+} + OH^{-} \rightarrow M(OH)_x \xrightarrow{\Delta} MO_{2/x} + H_2O \uparrow$
Impregnation-decomposition	$M(NO_3)_x \xrightarrow{\Delta} MO_{2/x} + NO_y \uparrow$
Surface reduction	$KMnO_4 \xrightarrow{Carbon} MnO_2$
Melt-diffusion	$S (s) \xrightarrow{\Delta} S (l) \xrightarrow{Solidification} S (s)$
<i>In situ</i> polymerization	$Monomer \xrightarrow{Oxidant} Polymer$

<sup>#</sup> M represents metal elements

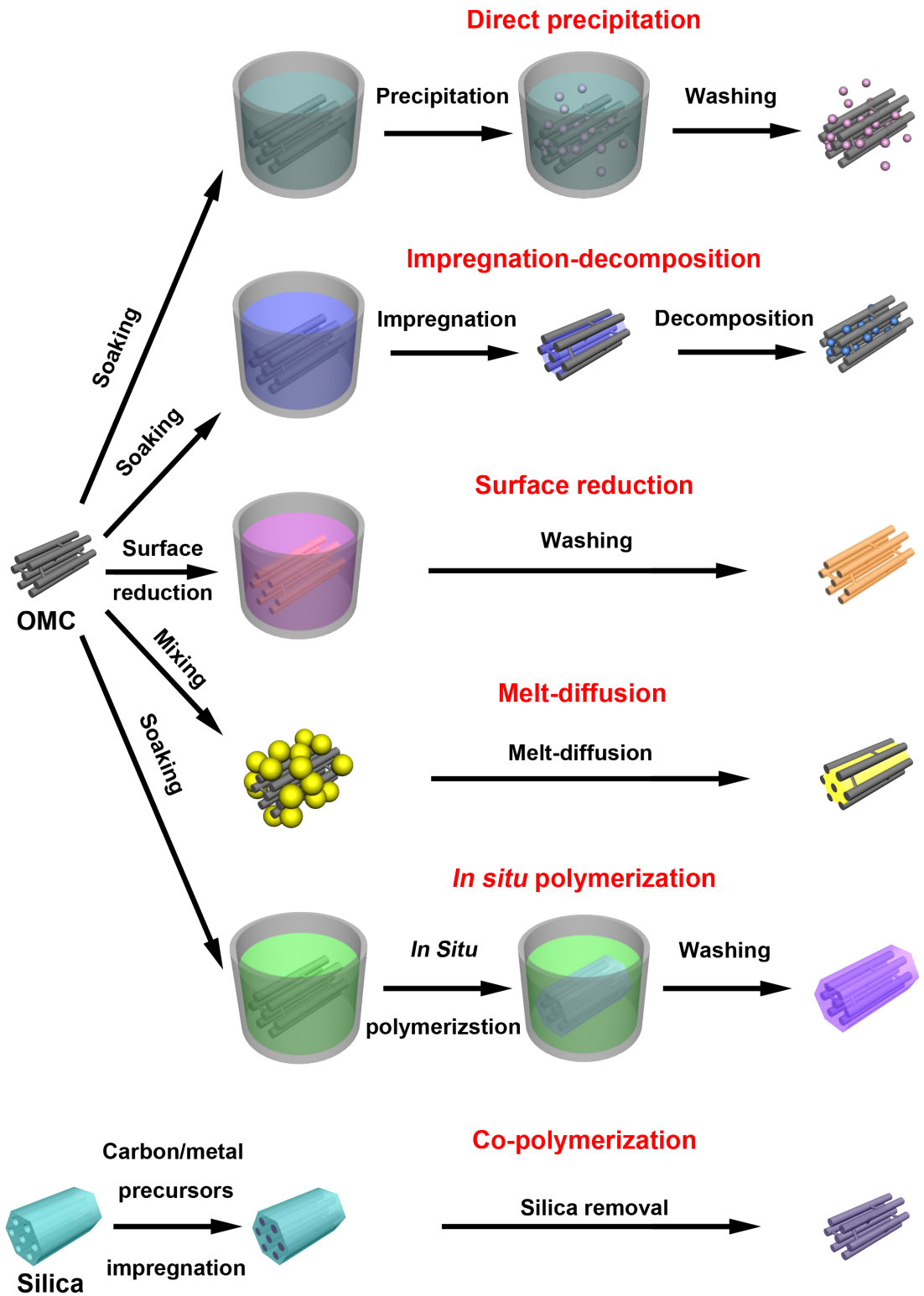


Figure 1. 7 Schematic illustrations for different strategies to embed guest nanoparticles into OMCs.

In general, most of the incorporation methods can be categorized into the following six strategies: the direct precipitation strategy, the impregnation-decomposition strategy, the surface reduction strategy, the melt-diffusion strategy, the *in situ* polymerization strategy, and the co-polymerization strategy. The schematic processes and typical reactions of these strategies are shown in Figure 1.7 and Table 1.1, and will be discussed in the following subsections. It should be pointed out that except the co-polymerization strategy, the other five strategies can be utilized to incorporate the guest materials to any forms of OMCs without distinguishing the porous structures. Therefore, when discussing each of these strategies, the detailed OMCs' mesostructures were neglected.

### 1.2.1 Direct precipitation

The simplest way for loading metal oxide or hydroxide into mesopores is direct precipitation method.  $\text{Fe}_2\text{O}_3$ ,<sup>24, 25</sup>  $\text{SnO}_2$ ,<sup>26-29</sup>  $\text{RuO}_2$ ,<sup>30</sup>  $\text{TiO}_2$ ,<sup>31</sup>  $\text{MoO}_2$ ,<sup>32</sup>  $\text{CuO}$ ,<sup>33</sup>  $\text{Co}(\text{OH})_2$ ,<sup>34</sup> and  $\text{Sn}$ ,<sup>26</sup> have been reported to be embedded in OMCs using this method. In general, the OMC powders were soaked in the solution containing metal salt (in most cases metal chloride), then  $\text{NH}_3 \cdot \text{H}_2\text{O}$  or  $\text{NaOH}$  solutions was added slowly to the above solution to increase the pH and precipitate the metal ions adsorbed on OMC. In some cases, the hydrothermal method was used to get the precipitate.<sup>25, 35</sup> The as prepared metal hydroxides were annealed under inert gas ( $\text{N}_2$  or  $\text{Ar}$ ) if the metal oxide is the targeted product.

Some salt can react with the solvent without adding a base. Yin's group<sup>32</sup> reported a solvothermal method to growth MoO<sub>2</sub> inside the mesopores of CMK-3. The precursor contains ammonium heptamolybdate, which could be reduced by the ethylene glycol solvent and form nanoparticles in the CMK-3. Chen's group<sup>26</sup> used SnCl<sub>2</sub> to directly reacted with water to the presence of mesoporous CMK-3. And the CMK-3/SnO<sub>2</sub>, CMK-3/Sn, or CMK-3/Sn/SnO<sub>2</sub> can be made by different post synthesis annealing conditions.

Although the direct precipitation method is widely applicable, the precipitation site was less controllable. Since the reaction takes place everywhere in the solution, it is hard to control the formation site of nanoparticles solely inside the mesopores. Even the OMC may act as crystal seeds at the initial stage of the reactions, and in most cases it is hard to grow exclusively nanoparticles inside the confined mesopores, where ion accessibility is prohibited compared with bulk solution. The particles formed outside the mesopores were generally bigger and less electronically accessible, which could potentially decrease the performance of the whole material. To address this problem, Li's group reported a modified precipitation method to grow SnO<sub>2</sub> in the OMC.<sup>35</sup> The mesopores of OMC were firstly filled by SnCl<sub>4</sub> aqueous solution, then exposed to NH<sub>3</sub> atmosphere; the reaction thus would only happen in the solutions inside the mesopores, leading to the selective growth of nanoparticles in the mesopores.

### **1.2.2 Impregnation-decomposition**

A more controllable incorporation strategy is the impregnation-decomposition method. As shown in Figure 1.7, the general synthesis includes three steps: the impregnation of the metal salt precursor, the solvent evaporation, and the thermal-decomposition of salt. The loading amount can be tuned via the concentration of the metal salt solution. Due to the capillary condensation in the mesopores, after solvent evaporation, the metal salt is predominantly located in the body of OMCs, leading to a selectively nanoparticle growth inside the mesopores. However, the amount of precursor and solvent evaporation speed still need to be carefully controlled to avoid the presence of metal salt outside the OMCs. Additionally, due to the hydrophobicity of carbon surface, sometimes it is hard for the hydrophilic solution to penetrate deeply into the core of the particles, resulting in a nonuniform growth of nanoparticles. Therefore, in some cases, ethanol was used instead of water to increase the affinity of solution with carbon.<sup>36-39</sup> However, since most of the salts are less soluble in ethanol, a more commonly used method is the  $\text{HNO}_3$ ,<sup>40</sup>  $\text{H}_2\text{SO}_4$ ,<sup>41</sup> or  $\text{H}_2\text{O}_2$ <sup>42, 43</sup> pre-treatment for OMCs to increase the hydrophilicity of carbon surface. In addition, sonication<sup>37</sup> and vacuum treatment<sup>44</sup> are also effective ways to increase solution penetration.

The most used salts were metal nitrates due to their high solubility in water. For the metals in the reactivity series between Mg and Cu, the gaseous nitrogen oxide species generated in decomposition process will flow out, and the desired metal oxide will remain in the mesopores matrix. Various metal oxides, including  $\text{MnO}_x$ ,<sup>45</sup>  $\text{Fe}_3\text{O}_4$ ,<sup>38</sup>  $\text{Fe}_2\text{O}_3$ ,<sup>44</sup>  $\text{V}_2\text{O}_3$ ,<sup>46</sup>  $\text{NiO}$ ,<sup>41</sup>  $\text{CoO}$ ,<sup>47</sup> and  $\text{Bi}_2\text{O}_3$ ,<sup>48</sup> have been synthesized inside the OMCs

using their corresponding nitrate salts.

Some of the metal nitrates have lower solubility or undesired decomposition products. In these cases, other precursors were used to get the desired materials. For example,  $\text{Ge}(\text{OC}_2\text{H}_5)_4$  was used for  $\text{GeO}_2$ ,<sup>42</sup>  $\text{H}_2\text{PtCl}_6$  was used for Pt,<sup>49</sup> indium acetate was used for  $\text{In}_2\text{O}_3$ ,<sup>50</sup>  $\text{SnCl}_4$  and  $\text{SnCl}_2$  were used for  $\text{SnO}_2$ <sup>43</sup> and  $\text{Sn}^{39}$ , respectively. In addition, metal oxide sol, which were generated by mixing metal oxide particles with  $\text{H}_2\text{O}_2$ , can be used as precursors to impregnate  $\text{MoO}_3$ <sup>51</sup> and  $\text{V}_2\text{O}_5$ <sup>52</sup>. Due to the excellent solubility, polyoxometalate (POM), particularly phosphomolybdic acid and phosphotungstic acid were used for the growth of  $\text{MoO}_2$ <sup>36, 53</sup> and  $\text{WO}_x$ ,<sup>40</sup> respectively.

A binary or ternary solutions were also used in impregnation-decomposition method to create some complicated compounds. For example, a promising cathode material  $\text{LiFePO}_4$  can be introduced in CMK-5 mesopores from the mixed precursors of  $\text{Fe}(\text{NO}_3)_3$ , lithium acetate, and  $\text{H}_3\text{PO}_4$  with the molar ratio of 1 : 1 : 1.<sup>54</sup>  $\text{Li}_4\text{Ti}_5\text{O}_{12}$  can be embedded into mesoporous CMK-3 by a combined tetrabutyl titanate and lithium acetate precursor.<sup>37</sup> A binary solution of  $\text{FeCl}_3$  and HF can be used for OMC/ $\text{FeF}_3$ , which is a cathodic material for LIBs.

One disadvantage of the impregnation-decomposition method is the limited guest nanoparticle loading amount. As the electrochemical performance of guest nanoparticles are generally better than mesoporous carbon itself, the larger loading amount is anticipated to get a better overall performance. However, the loading amount of guest nanoparticles by the impregnation-decomposition method is limited by the

precursor solubility and OMC pore volume, and normally less than 50 %. Although repeat impregnation-solvent evaporation processes can help to increase the loading amount,<sup>45, 55</sup> it can also increase the chance of nanoparticle growth outside the mesopores.

### **1.2.3 Surface reduction**

The surface reduction method is another effective strategy to get a homogeneous nanoparticle embedded in the mesopores of OMCs. This method was mostly used for MnO<sub>2</sub> nanoparticle growth.<sup>56-58</sup> In a typical synthesis process, the OMCs were soaked in the KMnO<sub>4</sub> aqueous solution for a given amount of time, then taken out and washed. During this process, the KMnO<sub>4</sub> is reduced by the carbon and forms MnO<sub>2</sub>. Since the reaction only occurs at the carbon/KMnO<sub>4</sub> interface, the MnO<sub>2</sub> nanoparticles were solely grown on the carbon surface, leading to a very uniform coating. The MnO<sub>2</sub> content can be adjusted via control of KMnO<sub>4</sub> concentration<sup>56</sup> or soaking time<sup>58</sup>. Besides MnO<sub>2</sub>, OMC/FeOOH can also be prepared via the reduction of K<sub>2</sub>FeO<sub>4</sub>.<sup>59</sup> It should be pointed out that the reduction of KMnO<sub>4</sub> is accompanied by the corrosion of the carbon framework, which is potentially harmful to the mesostructure of the composite. Therefore, the largest loading amount reported for this method is 35 wt%, which is moderate compared with other methods.

### **1.2.4 Melt-diffusion**

The melt-diffusion method is often used to incorporate sulfur in OMCs.<sup>60-62</sup> In this simple one step process, the physically mixed sulfur/OMCs were heated together at 155 °C. At this temperature the melted sulfur has the lowest viscosity and can penetrate into the mesopores in OMCs, and then after cool down the resulting composite can be directly used without further treatment. Due to the capillary condensation effect, the sulfur is predominantly located in the mesopores. Compared with impregnation-decomposition method, the liquid introduced by the melt-diffusion method is pure sulfur without other heteroatoms such as solvent or counter ions. Therefore, the mass loading of sulfur can be very high. However, the amount of sulfur needs be carefully controlled to not exceed the total mesopore volume, especially after the volume expansion in the fully lithiated state ( $\text{Li}_2\text{S}$ ). In addition, some post-heat treatments up to 300 °C were reported to evaporate the outer and part of the inter-porous sulfur to get a better sulfur utilizations.<sup>62</sup> Some other materials, *i. e.* Se,<sup>63</sup>  $\text{VO}_2$ ,<sup>64</sup> and phenanthrenequinone<sup>65</sup> can also be added to porous systems of OMCs via similar melt-diffusion method.

### **1.2.5 *In situ* polymerization**

Various conducting polymers, such as polyaniline (PANI),<sup>66</sup> polypyrrole (PPy),<sup>67</sup> and Poly(3,4-ethylenedioxythiophene) (PEDOT),<sup>68</sup> were successfully combined with OMCs via *in situ* polymerization. The synthesis procedure is quite similar to the direct precipitation method. In general, the OMC was dispersed in a monomer solution, then

an oxidant, normally the ammonium persulfate (APS) solution, was added dropwise to the above solution to polymerize the monomer. Similar to the direct precipitation method, the deposition sites in the *in situ* polymerization were also lacked control, resulting in a fully-filled mesopores and a covered OMC outer surface. Hence, the surface area can dramatically decrease from  $1300 \text{ m}^2 \text{ g}^{-1}$  in OMC, to  $35 \text{ m}^2 \text{ g}^{-1}$  after polymer growth.<sup>66</sup> In order to preserve the porous structure, several groups have tried to reduce the monomer amount to partially fill the mesopores.<sup>69, 70</sup> For some OMCs which use the mesoporous silica as a hard template, the silica can be removed after polymer growth, leaving the whole set of mesoporous system in OMC/polymer composites.<sup>71-73</sup>

The conducting polymer can be used as a protecting and conductive enhancement layer for other OMC based composites in the application of supercapacitor,<sup>74</sup> LIBs,<sup>75</sup> and Li-S batteries.<sup>76</sup> Lu.'s group,<sup>75</sup> have grown  $\text{Fe}_2\text{O}_3$  nanoparticles inside the mesopores of CMK-5 via the impregnation-decomposition method, and the CMK-5/ $\text{Fe}_2\text{O}_3$  composite was subsequently coated with polypyrrole via a vapor-phased *in situ* polymerization method. Instead of mixing monomers with oxidant in solution, they first fill the mesopores of the composite by  $\text{FeCl}_3$  oxidant, then expose it to pyrrole vapor, forming a much thinner but effective protection layer. This layer can effectively increase the capacity retention from 42 % to 97 % after 100 cycles.

### **1.2.6 Co-polymerization**

All of above methods built OMC nanostructures before incorporating guest nanoparticles. Such an approach requires multiple steps and is not very convenient. Therefore, many works tried to simplify the process by growing carbon framework and guest particles simultaneously.

The hard template derived OMC composites are easier to realize because the mesoporous silica framework can help to hold the mesostructure in the carbonization and guest material phase transformation processes. The synthesis procedure is similar to the synthesis of hard templated OMC, except the metal salts were added together with carbon precursors. For example, OMC/Si was synthesized by filling SBA-15 pores with butyl-terminated Si(Si-C<sub>4</sub>H<sub>9</sub>), followed by the annealing and SiO<sub>2</sub> etching. The silicon is wrapped by the carbon, forming the Si@C core-shell structure in the framework.<sup>77</sup> Several other OMC composites, such as OMC/NiO,<sup>78</sup> OMC/Sn,<sup>79</sup> and OMC/Mn<sub>3</sub>O<sub>4</sub>,<sup>80</sup> were also successfully fabricated by this one step method using mesoporous silica SBA-15 as a hard template.

The soft template derived OMC composites are much more complicated since they involve the surfactant / carbonizable oligomer / metal ions multicomponent interactions. Due to the different solubilities of carbon precursor and metal ions in the solvent, usually phase separation happens before the liquid crystal formation, producing a nonuniform distribution of carbon and metal oxide. Even if the uniform liquid crystal forms, since the mesostructure is not rigid, it might change in the following phase transformation or surfactant removal steps, leading to a disordered mesoporous

structure. Despite the complication, there were still a variety of metal oxides that have been successfully grown together with carbon to form ordered mesostructures. For example, tetraethyl orthosilicate (TEOS) can be added to FDU-15 synthesis precursors to form ordered mesoporous carbon/silica with any carbon/silica ratios.<sup>81</sup> Under carefully controlled conditions, other composite, such as OMC/TiO<sub>2</sub>,<sup>82-85</sup> OMC/SiO<sub>2</sub>/TiO<sub>2</sub>,<sup>86</sup> OMC/MoO<sub>2</sub>,<sup>87, 88</sup> OMC/Co<sub>3</sub>O<sub>4</sub>,<sup>89, 90</sup> OMC/VO<sub>x</sub>,<sup>90</sup> OMC/WO<sub>x</sub>,<sup>91</sup> OMC/Nb<sub>2</sub>O<sub>5</sub>,<sup>92</sup> and OMC/Ni,<sup>93</sup> were also successfully discovered.

An alternative strategy for the soft template method is to synthesize metal or metal oxide nanoparticles first, then embedded these nanoparticles in the OMC growth step. Silicon,<sup>94, 95</sup> iron oxide,<sup>96, 97</sup> and MnO<sup>98</sup> nanoparticles were co-deposited with ordered mesoporous carbon by this method.

Co-polymerization method combined the carbon synthesis process and guest material loading processes together, therefore, is usually more convenient than other incorporation strategies. In addition, the guest particles are embedded in the carbon framework, not occupying the mesopores, so it will not block the mesopores even with a large loading amount.<sup>81, 82, 91</sup> However, some special points still need to be considered when using this method. First, the annealing temperature needs to be carefully evaluated. The temperature should be higher than 700 °C to ensure enough carbon is graphitized, and normally the higher temperature will result in a better conductivity. However, the higher temperature might induce the crystal phase transformation of the metal or metal oxide, leading to a more densely packed crystal structure with less

activity for lithium or active ion insertion. In addition, some metal oxides will be reduced by carbon at high temperature, resulting in an inactive metal product or destruction of the carbon framework. Therefore, a moderate annealing temperature needs to be chosen to achieve a good conductivity while maintaining the active crystal structure. Second, as mentioned above, due to the complicated interactions between each species, the ordered mesostructure is hard to achieve. Hence, under the restrict synthesis condition, it is hard to control the guest material loading amount in the composite. Third, since the guest nanoparticles are created before or simultaneously with the mesopores, the size of nanoparticles are not confined by the mesopores. Hence, sometimes the larger size particles are formed by this method.<sup>54, 93-95</sup>

### **1.3 Electrochemical energy storage of OMC based composites**

#### **1.3.1 Supercapacitors**

Due to good conductivity, high porosity, and large surface area, OMCs themselves are good electrical double-layer capacitors.<sup>99</sup> However, due to the limitation of EDLCs, the capacitance of OMCs are normally less than  $200 \text{ F g}^{-1}$ ,<sup>2</sup> which is not satisfactory. On the other hand, the pseudocapacitive metal oxides often show larger capacitance than OMCs, but they suffer from bad conductivity, which limits their power performance.<sup>7</sup> One strategy to overcome the drawbacks of these two materials is to combine them together to make hybrid composites with balanced properties. In addition to better conductivity, the OMCs also provide a fast ion pathway through their channels,

and limit the metal oxide dimensions in their confined framework. All of these improve the utilizations of metal oxide and increases the overall electrochemical performance of the composites. Hence, as shown in Figure 1.1, there are a lot of work focusing on heterogeneous OMCs/metal oxides composites as high performance supercapacitors.

Besides metal oxides, conducting polymers are also often combined with OMCs. Upon loading, they can form nanostructures inside and outside the OMCs. These nanostructures can enhance their electrochemical utilizations, particularly at a high rate. The cycling performance is also improved because the OMCs can help stabilize the physical structure of the conducting polymer. Due to the different beneficial effects, these two kinds of composites will be discussed separately in this section.

**Table 1. 2 OMC based hybrid materials for supercapacitors**

Materials	Preparing method	Guest wt % <sup>a</sup>	Specific electrode capacitance <sup>b</sup>	Cycling stability	Voltage window <sup>c</sup>	Electrolyte <sup>d</sup>	Ref.
OMC/Metal oxide							
CMK-3/ V <sub>2</sub> O <sub>5</sub>	Impregnation- decomposition	NA	124 F g <sup>-1</sup> (0.2 A g <sup>-1</sup> )	NA	0 ~ 0.8 V vs. SCE	1 M KNO <sub>3</sub>	52
CMK-3/ VO <sub>2</sub>	Melt-diffusion	20 %	131 F g <sup>-1</sup> (0.2 A g <sup>-1</sup> )	NA	0 ~ 0.6 V vs. SCE	1 M KNO <sub>3</sub>	64
OMC/ VO <sub>x</sub> film	Co- polymerization	36.5 % <sup>c</sup>	215 F g <sup>-1</sup> (100 mV s <sup>-1</sup> )	74 % (500 <sup>th</sup> )	-1 ~ -0.4 V vs. Hg/Hg <sub>2</sub> SO <sub>4</sub>	1 M Na <sub>2</sub> SO <sub>4</sub>	90
CMK-3/ MnO <sub>2</sub>	Surface reduction	26 %	173 F g <sup>-1</sup> (5 mV s <sup>-1</sup> ) & 130 F g <sup>-1</sup> (50 mV s <sup>-1</sup> )	92 % (1000 <sup>th</sup> )	0 ~ 1 V vs. SCE	2 M KCl	56
FDU-15/ MnO <sub>2</sub>	Surface reduction	30 %	79 F g <sup>-1</sup> (2 mV s <sup>-1</sup> ) & 54 F g <sup>-1</sup> (100 mV s <sup>-1</sup> )	NA	-0.4 ~ 0.4 V vs. Hg/Hg <sub>2</sub> SO <sub>4</sub>	1 M Na <sub>2</sub> SO <sub>4</sub>	57

**Table 1. 2 OMC based hybrid materials for supercapacitors (Continued)**

Materials	Preparing method	Guest wt % <sup>a</sup>	Specific electrode capacitance <sup>b</sup>	Cycling stability	Voltage window <sup>c</sup>	Electrolyte <sup>d</sup>	Ref.
GMC <sup>f</sup> / MnO <sub>2</sub>	Surface reduction	35 %	160 F g <sup>-1</sup> (2 mV s <sup>-1</sup> ) & 127 F g <sup>-1</sup> (200 mV s <sup>-1</sup> )	NA	-0.4 ~ 0.4 V vs. Hg/Hg <sub>2</sub> SO <sub>4</sub>	1 M Na <sub>2</sub> SO <sub>4</sub>	58
OMC/ MnO	Co-polymerization	84.3 %	160 F g <sup>-1</sup> (1 A g <sup>-1</sup> ) & 41.2 F g <sup>-1</sup> (40 A g <sup>-1</sup> )	110 % (2500 <sup>th</sup> )	0 ~ 1 V vs. Ag/AgCl	0.5 M Na <sub>2</sub> SO <sub>4</sub>	98
N-OMC/ Fe <sub>2</sub> O <sub>3</sub>	Co-polymerization	30 %	235 F g <sup>-1</sup> (0.5 A g <sup>-1</sup> ) & 119 F g <sup>-1</sup> (10 A g <sup>-1</sup> )	95 % (380 <sup>th</sup> )	-1 ~ -0.2 V vs. Ag/AgCl	1 M Na <sub>2</sub> SO <sub>3</sub>	97
CMK-3/ FeOOH	Surface reduction	23 %	113 F g <sup>-1</sup> (2 mV s <sup>-1</sup> ) & 100 F g <sup>-1</sup> (10 mV s <sup>-1</sup> )	NA	0 ~ 1.8 V, 2 electrodes	6 M KOH	59
OMC/ CoO <sub>x</sub> film	Co-polymerization	17.5 % <sup>g</sup>	125 F g <sup>-1</sup> (100 mV s <sup>-1</sup> )	62 % (500 <sup>th</sup> )	-1 ~ -0.4 V vs. Hg/Hg <sub>2</sub> SO <sub>4</sub>	1 M Na <sub>2</sub> SO <sub>4</sub>	90
CMK-3/ NiO	Co-polymerization	10 %	170 F g <sup>-1</sup> (1.2 A g <sup>-1</sup> )	NA	-1.2 ~ -0.4 V vs. SCE	2 M KOH	78
OMC/ SnO <sub>2</sub>	Direct precipitation	57 %	67 F g <sup>-1</sup> (0.1 A g <sup>-1</sup> ) & 40 F g <sup>-1</sup> (2 A g <sup>-1</sup> ) <sup>h</sup>	80 % (2000 <sup>th</sup> )	0.5 ~ 4 V vs. C, asymmetric 2 electrodes	1 M LiPF <sub>6</sub> <sup>i</sup>	35
OMC/ Nb <sub>2</sub> O <sub>5</sub>	Co-polymerization	89 %	~300 F g <sup>-1</sup> (0.1 A g <sup>-1</sup> ) & 218 F g <sup>-1</sup> (5 A g <sup>-1</sup> )	80 % (4000 <sup>th</sup> )	1.1 ~ 3 V vs. Li/Li <sup>+</sup> , asymmetric 2 electrodes	1 M LiPF <sub>6</sub> <sup>j</sup>	92
OMC/ MoO <sub>2</sub>	Impregnation-decomposition	27 %	216 F cm <sup>-3</sup> (2 mV s <sup>-1</sup> )	90 % (50 <sup>th</sup> )	-0.3 ~ 0.4 V vs. SCE	1 M H <sub>2</sub> SO <sub>4</sub>	53
OMC/ MoO <sub>2</sub>	Co-polymerization	38 %	150 F g <sup>-1</sup> (2 mV s <sup>-1</sup> )	100 % (50 <sup>th</sup> )	-0.2 ~ 0.6 V vs. SCE	1 M H <sub>2</sub> SO <sub>4</sub>	88
OMC/ MoO <sub>3</sub>	Impregnation-decomposition	29.1 %	251.3 F g <sup>-1</sup> (5 mV s <sup>-1</sup> )	NA	-0.9 ~ 0.1 V vs. Hg/HgO	1 M KNO <sub>3</sub>	51
CMK-3/ RuO <sub>2</sub>	Direct precipitation	30.7 %	633 F g <sup>-1</sup> (1 mV s <sup>-1</sup> ) & 251 F g <sup>-1</sup> (100 mV s <sup>-1</sup> )	NA	0 ~ 0.8 V vs. Ag/AgCl	2 M KOH	100
CMK-3/ In <sub>2</sub> O <sub>3</sub>	Impregnation-decomposition	5 %	275 F g <sup>-1</sup> (5 mV s <sup>-1</sup> ) & 232 F g <sup>-1</sup> (100 mV s <sup>-1</sup> )	96 % (500 <sup>th</sup> )	-0.4 ~ 0.2 V	1 M Na <sub>2</sub> SO <sub>4</sub>	50

**Table 1. 2 OMC based hybrid materials for supercapacitors (Continued)**

Materials	Preparing method	Guest wt % <sup>a</sup>	Specific electrode capacitance <sup>b</sup>	Cycling stability	Voltage window <sup>c</sup>	Electrolyte <sup>d</sup>	Ref.
OMC/ WO <sub>3-x</sub>	Co-polymerization	76 %	103 F g <sup>-1</sup> (1 mV s <sup>-1</sup> )	NA	-0.2 ~ 0.8 V vs. Ag/AgCl	2 M H <sub>2</sub> SO <sub>4</sub>	91
OMC/ WO <sub>3-x</sub>	Impregnation-decomposition	33 %	175 F g <sup>-1</sup> (2 mV s <sup>-1</sup> )	133 % (1100 <sup>th</sup> )	-0.2 ~ 0.7 V vs. SCE	1 M H <sub>2</sub> SO <sub>4</sub>	40
OMC/ Bi <sub>2</sub> O <sub>3</sub>	Direct precipitation	10 %	232 F g <sup>-1</sup> (5 mV s <sup>-1</sup> ) & 153 F g <sup>-1</sup> (100 mV s <sup>-1</sup> )	79 % (1000 <sup>th</sup> )	-0.9 ~ 0.1 V vs. Hg/HgO	6 M KOH	48
CMK-3/ MnO <sub>2</sub> / PPy	Surface reduction & <i>In situ</i> polymerization	12 % MnO <sub>2</sub>	695 F g <sup>-1</sup> (0.3 A g <sup>-1</sup> ) & ~584 F g <sup>-1</sup> (3 A g <sup>-1</sup> )	88 % (1000 <sup>th</sup> )	-0 ~ 0.8 V, 2 electrodes	1 M H <sub>2</sub> SO <sub>4</sub>	74
OMC/Conducting polymer							
CMK-3/ PANI	<i>In situ</i> polymerization	70 %	900 F g <sup>-1</sup> (0.5 A g <sup>-1</sup> ) & 768 F g <sup>-1</sup> (5 A g <sup>-1</sup> )	95 % (3000 <sup>th</sup> )	-0.2 ~ 0.7 V vs. SCE	1 M H <sub>2</sub> SO <sub>4</sub>	66
CMK-3/ PANI	<i>In situ</i> polymerization	50 %	747 F g <sup>-1</sup> (0.1 A g <sup>-1</sup> ) & 492 F g <sup>-1</sup> (3 A g <sup>-1</sup> )	88 % (1000 <sup>th</sup> )	0 ~ 0.9 V vs. Hg/HgO	30 wt % KOH	69
OMC/ PANI	<i>In situ</i> polymerization	46.6 %	400 F g <sup>-1</sup> (1 A g <sup>-1</sup> ) & ~364 F g <sup>-1</sup> (20 A g <sup>-1</sup> )	80 % (1000 <sup>th</sup> )	-0.7 ~ 0 V vs. Hg/HgO	6 M KOH	70
CMK-3/ PANI	<i>In situ</i> polymerization	40 %	470 F g <sup>-1</sup> (0.1 A g <sup>-1</sup> ) & ~409 F g <sup>-1</sup> (2 A g <sup>-1</sup> )	90.4 % (1000 <sup>th</sup> )	-0.2 ~ 0.8 V, 2 electrodes	1 M H <sub>2</sub> SO <sub>4</sub>	73
OMC/ PANI	<i>In situ</i> polymerization	60 %	517 F g <sup>-1</sup> (0.1 A g <sup>-1</sup> ) & ~368 F g <sup>-1</sup> (5 A g <sup>-1</sup> )	91.5 % (1000 <sup>th</sup> )	-0 ~ 0.8 V, 2 electrodes	1 M H <sub>2</sub> SO <sub>4</sub>	72
OMC/ PANI	<i>In situ</i> polymerization	NA	343 F g <sup>-1</sup> (0.2 A g <sup>-1</sup> ) & 225 F g <sup>-1</sup> (10 A g <sup>-1</sup> )	95 % (2000 <sup>th</sup> )	-0.2 ~ 0.8 V, 2 electrodes	1 M H <sub>2</sub> SO <sub>4</sub>	71
CMK-5/ PANI	<i>In situ</i> polymerization	64 %	803 F g <sup>-1</sup> (0.1 A g <sup>-1</sup> ) & 272 F g <sup>-1</sup> (10 A g <sup>-1</sup> )	81 % (1000 <sup>th</sup> )	-0.2 ~ 0.8 V, 2 electrodes	2 M H <sub>2</sub> SO <sub>4</sub>	101
CMK-3/ PPy	<i>In situ</i> polymerization	82 %	427 F g <sup>-1</sup> (5 mA cm <sup>-2</sup> ) & ~370 F g <sup>-1</sup> (50 mA cm <sup>-2</sup> )	76 % (500 <sup>th</sup> )	-0.4 ~ 0.6 V vs. SCE	1 M H <sub>2</sub> SO <sub>4</sub>	67

<sup>a</sup> Based on guest materials mass, unless specified.<sup>b</sup> Based on the total mass of carbon and guest materials in the single electrode.

- <sup>c</sup> Based on three electrode system, unless specified.  
<sup>d</sup> In the aqueous electrode, unless specified.  
<sup>e</sup> Based on V and C mass.  
<sup>f</sup> GMC: graphitic mesoporous carbon annealed at 2600 °C  
<sup>g</sup> Based on Co and C mass.  
<sup>h</sup> based on total mass of anode and cathode  
<sup>i</sup> 1 M LiPF<sub>6</sub> in 1/1/1 EC/ DMC/EMC  
<sup>j</sup> 1 M LiPF<sub>6</sub> in 1/1 EC/DMC

### 1.3.1.1 OMC/metal oxides

The first metal oxide incorporated in the OMC was MnO<sub>2</sub>, which is one of the most promising pseudocapacitive materials due to its large theoretical capacitance (1370 F g<sup>-1</sup>),<sup>102</sup> high abundance, and good environmental compatibility. In 2006, Shi's group<sup>56</sup> embedded MnO<sub>2</sub> in CMK-3 carbon wall by KMnO<sub>4</sub> surface reduction method. N<sub>2</sub> adsorption-desorption showed that the MnO<sub>2</sub> is located in the pore walls without blocking mesopores; with only 26 wt % of MnO<sub>2</sub>, a specific capacitance can be doubled from 105 F g<sup>-1</sup> in CMK-3, to 220 F g<sup>-1</sup> for the composite, which corresponds to a very high MnO<sub>2</sub> capacitance of 547 F g<sup>-1</sup>. This excellent electrochemical performance is attributed to the good ion transport in the mesopores. Patel's group<sup>57</sup> incorporated the MnO<sub>2</sub> into soft templated OMC by a similar method. They found that the specific capacitance of MnO<sub>2</sub> decreases when the loading amount increases, and the capacitance of the composite stays similar if the MnO<sub>2</sub> wt % is larger than 21 %. These phenomena were explained by the decreased diffusion coefficient in a high loaded sample characterized by chronoamperometry. They further evaluated the influence of carbon conductivity by using a graphitic mesoporous carbon annealed at 2600 °C as host

materials.<sup>58</sup> The result showed that the increased conductivity can double the MnO<sub>2</sub> capacitance and greatly improve its rate performance.

Two-dimensional OMC thin films (<500 nm) embedded with cobalt and vanadium oxide can be synthesized by a soft template induced co-polymerization method. Interestingly, introducing Co or V species can enhance the mechanical strength and increase the OMC pore size up to 60 %. A significant capacitance enhancement was found in Co-containing (125 F g<sup>-1</sup>) and V-containing (215 F g<sup>-1</sup>) carbons compared with bare carbon (22 F g<sup>-1</sup>). The larger capacitance of V-containing carbons is majorly due to its small VO<sub>x</sub> particle size (<2 nm) compared with CoO<sub>x</sub> (>10 nm).

Other metal oxides, such as NiO,<sup>78</sup> MoO<sub>2</sub>,<sup>53, 88</sup> WO<sub>3-x</sub>,<sup>40, 91</sup> RuO<sub>2</sub>,<sup>100</sup> In<sub>2</sub>O<sub>3</sub>,<sup>50</sup> and Bi<sub>2</sub>O<sub>3</sub>,<sup>48</sup> have also been introduced into mesopores of different kinds of OMCs and showed improved capacitance performances, as summarized in Table 1.2.

The fast ion diffusion pathway and good electronic conductivity made the OMC/Metal oxide a good candidate for the hybrid supercapacitors (HSCs), which is the combination of battery and supercapacitor. The charge/discharge process in HSCs anodes are similar to LIBs, which involves lithium intercalation/deintercalation. The cathode part is made of a double layer capacitor, which adsorbs/desorbs counter ions during charge/discharge processes. The resulting hybrid device will exhibit balanced power density and energy density. For example, an HSC using mesoporous SnO<sub>2</sub> embedded OMC as anode, and a regular OMC as cathode can achieve a maximum energy density of 110Wh kg<sup>-1</sup> and a maximum power density of 2960 W kg<sup>-1</sup>.<sup>35</sup> Using

a soft template co-polymerization method, OMC/Nb<sub>2</sub>O<sub>5</sub> can be made with extremely high Nb<sub>2</sub>O<sub>5</sub> loading amount (87 %) and very large mesopores size (30 nm). By pairing with active carbon, the whole device can achieve 15 Wh kg<sup>-1</sup> energy density with the power density of 18510 W kg<sup>-1</sup>.

### 1.3.1.2 OMC/conducting polymers

Conducting polymers have gained a lot of interested as supercapacitors due to their good conductivity, high capacitance, low cost, and biocompatibility. However, a low mechanical stability of polymers during charge-discharge processes results in a low cycling performance, which limits their applications.<sup>103</sup> To address this problem, many efforts try to incorporate conducting polymer to strengthening the materials and improve their cycling performance.<sup>104</sup> Among them, OMC is a good candidate because it not only stabilizes the structures, but also enhances the ion accessibility by forming the unique nanostructures.

Polyaniline (PANI) is the most reported polymer for OMC/conducting polymer composite, probably due to its high theoretical capacitance and relatively lower conductivity (0.1-5 S cm<sup>-1</sup>)<sup>105</sup>. Xia's group<sup>66</sup> firstly synthesized the CMK-3/PANI composite via the *in situ* polymerization method. The PANI not only filled the mesopores, but also covered the OMC surface with whiskerlike nanostructures. Each of these thorns is about 80–100 nm in length and 10–20 nm in diameter. Due to the high theoretical capacitance and the high loading (70 wt %) PANI, an ultra-high capacitance of 900 F g<sup>-1</sup> was achieved at current density of 0.5 A g<sup>-1</sup>, with 85 % capacitance retention

at high current of  $5 \text{ A g}^{-1}$ , and excellent cycling stability of 5 % capacitance loss after 3000 cycles. However, as most of the mesopores were occupied by PANI, the surface area of OMC did not contribute to the total capacitance. In addition, the blocked mesopores limit the ion transportation in the composite particles, which prevents the full utilization of PANI located inside the mesopores. Therefore, many efforts were made to increase the composite porosity, as is discussed in section 2.5.<sup>69-73</sup> Generally, they all had improved surface area and pore volume. However, as shown in Table 1.2, due to the smaller PANI contents in their composite, the overall performances were still not satisfactory.

### **1.3.2 Lithium-ion batteries**

Similar to supercapacitors, OMCs were used as a charge transfer and a current collector for metal oxides or semiconductors for the LIBs. In addition, it can effectively reduce the guest nanoparticles' dimension and provide meso-channels as fast ion pathways, leading to an improved ion accessibility. More importantly, most of lithium intercalation processes for the metal oxide or semiconductor involves huge volume change, which would severely pulverize the particles and decrease their electrical connectivity. The OMCs framework can restrain the expansion, and the large volume can effectively buffer the volume change during cycling, resulting in a better cyclability.

Indeed, OMCs themselves are a good candidate as anode materials of LIBs. The theoretical capacity of graphite is  $372 \text{ mAh g}^{-1}$ , corresponding to the lithium

intercalation to form  $\text{LiC}_6$ . The practical performance of OMCs, however, was normally larger than the theoretical capacity. For example, CMK-3 has been reported to present  $1100 \text{ mAh g}^{-1}$  reversible capacity, which is about three times higher than the theoretical capacity.<sup>106</sup> The high capacities in OMCs are due to the abundant defect sites and surface functional groups, as well as the large surface area. Since most of the OMCs potential plateaus are  $< 0.5 \text{ V vs. Li/Li}^+$ , in order to utilize the OMCs own capacity, they were more often combined with anode materials rather than cathode materials.

### **1.3.2.1 Anodic materials**

Silicon is the most promising anode material for LIBs due to its abundant source (No. 2 element in Earth's crust) and high theoretical capacity ( $4200 \text{ mAh g}^{-1}$ ). However, the major problem of Si anode is its fast capacity fade upon cycling, which is due to the huge volume change (400%) during  $\text{Li}^+$  insertion-desertion processes. Therefore, as shown in Table 1.3, a lot of works reported incorporation of the Si into OMCs frameworks to diminish the volume change effect. For example, OMC/Si composite was fabricated by a hard template co-polymerization method using SBA-15 as a hard template.<sup>77</sup> The structure was like bundles of nanowires, which is similar to CMK-3. Each of these nanowires was 6.5 nm in diameter and was built up with the Si@C core-shell structure. The capacity at a current density of  $0.6 \text{ A g}^{-1}$  was  $3163 \text{ mAh g}^{-1}$ , which is close to the theoretical capacity. Due to the good conductivity of carbon shell and short  $\text{Li}^+$  diffusion length in nanowires, it had a good rate capability of 78 % at  $6 \text{ A g}^{-1}$ . More importantly, compared with bare silicon anode, which almost lost 100 % of its

capacity within 50 cycles,<sup>107</sup> the ordered mesoporous core-shell structured Si@C showed an excellent capacity retention of 87 % after 80 cycles. This result was primarily due to the improved connection between Si and C during cycling.

**Table 1. 3 OMC based hybrid materials for LIBs anode**

Materials	Preparing method	Guest wt %	Specific capacity <sup>a</sup>	Cycling stability	Ref.
OMC/Si	Co-polymerization	NA	3163 mAh g <sup>-1</sup> (0.6 A g <sup>-1</sup> ) & 2462 mAh g <sup>-1</sup> (6 A g <sup>-1</sup> )	87 % (6 A g <sup>-1</sup> , 80 <sup>th</sup> )	77
OMC/Si	Co-polymerization	49.5 %	499 mAh g <sup>-1</sup> (3 C)	> 100 % (1 C, 50 <sup>th</sup> )	94
OMC/Si	Co-polymerization	76 %	1410 mAh g <sup>-1</sup> (0.5 A g <sup>-1</sup> ) & 180 mAh g <sup>-1</sup> (10 A g <sup>-1</sup> )	72.2 % (0.5 A g <sup>-1</sup> , 100 <sup>th</sup> )	95
N-OMC/SiO <sub>2</sub>	Co-polymerization	54 %	778 mAh g <sup>-1</sup> (0.1 A g <sup>-1</sup> ) & 289 mAh g <sup>-1</sup> (1 A g <sup>-1</sup> )	~50 % (0.2 A g <sup>-1</sup> , 100 <sup>th</sup> )	108
OMC/SiO <sub>2</sub> /TiO <sub>2</sub>	Co-polymerization	44 % SiO <sub>2</sub> 12 % TiO <sub>2</sub>	490 mAh g <sup>-1</sup> (0.1 C) & 333 mAh g <sup>-1</sup> (0.5 C)	~70 % (0.5 C, 50 <sup>th</sup> )	86
OMC/TiO <sub>2</sub>	Co-polymerization	~70 %	197 mAh g <sup>-1</sup> (0.05 A g <sup>-1</sup> ) & 109 mAh g <sup>-1</sup> (1 A g <sup>-1</sup> )	~50 % (0.1 A g <sup>-1</sup> , 10 <sup>th</sup> )	84
OMC/TiO <sub>2</sub>	Co-polymerization	65 %	520 mAh g <sup>-1</sup> (0.035 A g <sup>-1</sup> ) & 98 mAh g <sup>-1</sup> (1.75 A g <sup>-1</sup> )	~75 % (0.035 A g <sup>-1</sup> , 80 <sup>th</sup> )	82
CMK-3/TiO <sub>2</sub>	Direct precipitation	15 %	560 mAh g <sup>-1</sup> (0.2 A g <sup>-1</sup> ) & 260 mAh g <sup>-1</sup> (1.6 A g <sup>-1</sup> )	~44 % (0.1 A g <sup>-1</sup> , 60 <sup>th</sup> )	31
CMK-8/V <sub>2</sub> O <sub>3</sub>	Impregnation-decomposition	73.7 %	541 mAh g <sup>-1</sup> (0.1 A g <sup>-1</sup> ) & 309 mAh g <sup>-1</sup> (2 A g <sup>-1</sup> )	78.2 % (0.1 A g <sup>-1</sup> , 180 <sup>th</sup> )	46
OMC/Mn <sub>3</sub> O <sub>4</sub>	Co-polymerization	20.3 %	795 mAh g <sup>-1</sup> (0.1 A g <sup>-1</sup> )	100 % (0.1 A g <sup>-1</sup> , 50 <sup>th</sup> )	80
OMC/MnO	Co-polymerization	84.3 %	900 mAh g <sup>-1</sup> (0.1 A g <sup>-1</sup> ) & 520 mAh g <sup>-1</sup> (2 A g <sup>-1</sup> )	82 % (0.1 A g <sup>-1</sup> , 80 <sup>th</sup> )	98
OMC/MnO <sub>x</sub>	Impregnation-decomposition	68.4 %	~950 mAh g <sup>-1</sup> (0.1 A g <sup>-1</sup> ) & ~600 mAh g <sup>-1</sup> (2 A g <sup>-1</sup> )	> 100 % (0.2 A g <sup>-1</sup> , 50 <sup>th</sup> )	45

**Table 1. 3 OMC based hybrid materials for LIBs anode (Continued)**

Materials	Preparing method	Guest wt %	Specific capacity <sup>a</sup>	Cycling stability	Ref.
OMC/ Fe <sub>3</sub> O <sub>4</sub>	Co- polymerization	39.4 %	577 mAh g <sup>-1</sup> (0.5 A g <sup>-1</sup> ) & 271 mAh g <sup>-1</sup> (10 A g <sup>-1</sup> )	NA	96
CMK-3/ Fe <sub>3</sub> O <sub>4</sub>	Impregnation- decomposition	41.57 %	970 mAh g <sup>-1</sup> (0.1 A g <sup>-1</sup> ) & 610 mAh g <sup>-1</sup> (1 A g <sup>-1</sup> )	> 100 % (1 A g <sup>-1</sup> , 100 <sup>th</sup> )	38
CMK-3/ FeO <sub>x</sub>	Direct precipitation	16 %	> 660 mAh g <sup>-1</sup> (0.1 A g <sup>-1</sup> ) & 320 mAh g <sup>-1</sup> (1.6 A g <sup>-1</sup> )	NA	25
CMK-5/ Fe <sub>2</sub> O <sub>3</sub>	Direct precipitation	47 %	683 mAh g <sup>-1</sup> (0.2 A g <sup>-1</sup> ) & 430 mAh g <sup>-1</sup> (1.5 A g <sup>-1</sup> )	99 % (0.2 A g <sup>-1</sup> , 100 <sup>th</sup> )	24
CMK-5/ Fe <sub>2</sub> O <sub>3</sub> /PPy	Impregnation- decomposition & <i>In situ</i> polymerization	47 % Fe <sub>2</sub> O <sub>3</sub> 6 % PPy	785 mAh g <sup>-1</sup> (0.2 A g <sup>-1</sup> ) & 430 mAh g <sup>-1</sup> (1.5 A g <sup>-1</sup> )	97 % (0.2 A g <sup>-1</sup> , 100 <sup>th</sup> )	75
OMC/ Co <sub>3</sub> O <sub>4</sub>	Co- polymerization	36.6 %	1130 mAh g <sup>-1</sup> (0.05 A g <sup>-1</sup> ) & 580 mAh g <sup>-1</sup> (1.5 A g <sup>-1</sup> )	> 100 % (0.1 A g <sup>-1</sup> , 100 <sup>th</sup> )	89
CMK-3/ NiO	Impregnation- decomposition	36.6 %	1152 mAh g <sup>-1</sup> (0.1 A g <sup>-1</sup> ) & 413 mAh g <sup>-1</sup> (3.2 A g <sup>-1</sup> )	88 % (1 A g <sup>-1</sup> , 50 <sup>th</sup> )	41
CMK-3/ CuO	Direct precipitation	11.5 %	747 mAh g <sup>-1</sup> (0.1 C) & 179 mAh g <sup>-1</sup> (25 C)	NA	33
OMC/ GeO <sub>2</sub>	Impregnation- decomposition	40 %	680 mAh g <sup>-1</sup> (0.3 A g <sup>-1</sup> ) & 120 mAh g <sup>-1</sup> (15 A g <sup>-1</sup> )	93 % (1.5 A g <sup>-1</sup> , 380 <sup>th</sup> )	42
CMK-3/ MoO <sub>2</sub>	Direct precipitation	45.3 %	1044 mAh g <sup>-1</sup> (0.1 A g <sup>-1</sup> ) & ~600 mAh g <sup>-1</sup> (1.6 A g <sup>-1</sup> )	99 % (0.1 A g <sup>-1</sup> , 50 <sup>th</sup> )	32
CMK-3/ MoO <sub>2</sub>	Direct precipitation	63 %	784 mAh g <sup>-1</sup> (0.05 A g <sup>-1</sup> ) & 490 mAh g <sup>-1</sup> (1 A g <sup>-1</sup> )	88 % (0.05 A g <sup>-1</sup> , 50 <sup>th</sup> )	36
CMK-3/ MoO <sub>2</sub>	Co- polymerization	38 %	571 mAh g <sup>-1</sup> (0.1 C) & 175 mAh g <sup>-1</sup> (2 C)	64.1 % (0.1 C, 30 <sup>th</sup> )	87
CMK- 3/Sn	Impregnation- decomposition	NA	400 mAh g <sup>-1</sup> (0.05C)	NA	39

**Table 1. 3 OMC based hybrid materials for LIBs anode (Continued)**

Materials	Preparing method	Guest wt %	Specific capacity <sup>a</sup>	Cycling stability	Ref.
OMC/ Sn	Co- polymerization	24.6 %	560 mAh g <sup>-1</sup> (0.1C) & 330 mAh g <sup>-1</sup> (2C)	100 % (0.1 C, 100 <sup>th</sup> )	79
CMK- 3/Sn/SnO <sub>2</sub>	Direct precipitation	58.2 %	799 mAh g <sup>-1</sup> (0.1 A g <sup>-1</sup> ) & 350 mAh g <sup>-1</sup> (0.8 A g <sup>-1</sup> )	84 % (0.1 A g <sup>-1</sup> , 50 <sup>th</sup> )	26
OMC/ SnO <sub>2</sub>	Direct precipitation	72 %	650 mAh g <sup>-1</sup> (0.2 A g <sup>-1</sup> ) & 334 mAh g <sup>-1</sup> (1 A g <sup>-1</sup> )	70.6 % (0.1 A g <sup>-1</sup> , 50 <sup>th</sup> )	27
CMK-3/ SnO <sub>2</sub>	Direct precipitation	20 %	946 mAh g <sup>-1</sup> (0.1 A g <sup>-1</sup> ) & 440 mAh g <sup>-1</sup> (1.6 A g <sup>-1</sup> )	54.7 % (0.1 A g <sup>-1</sup> , 100 <sup>th</sup> )	28
CMK-5/ SnO <sub>2</sub>	Direct precipitation	80 %	978 mAh g <sup>-1</sup> (0.2 A g <sup>-1</sup> ) & 600 mAh g <sup>-1</sup> (1.5 A g <sup>-1</sup> )	~100 % (0.2 A g <sup>-1</sup> , 100 <sup>th</sup> )	29
OMC/ SnO <sub>2</sub>	Impregnation- decomposition	40 %	650 mAh g <sup>-1</sup> (1.4 A g <sup>-1</sup> ) & 312 mAh g <sup>-1</sup> (0.14 A g <sup>-1</sup> )	48.4 % (1.4 A g <sup>-1</sup> , 2000 <sup>th</sup> )	43
CMK-3/ Li <sub>4</sub> Ti <sub>5</sub> O <sub>12</sub>	Impregnation- decomposition	84 %	121.3 mAh g <sup>-1</sup> (10 C) & 73.4 mAh g <sup>-1</sup> (80 C)	94.4 % (20 C, 1000 <sup>th</sup> )	37

<sup>a</sup> Based on the total mass of carbon and guest materials.

Zhou's group has embedded SnO<sub>2</sub> nanoparticles into CMK-5, an OMCs derived from the SBA-15 hard template. The composite showed 978 mAh g<sup>-1</sup> at a current density of 0.2 A g<sup>-1</sup>, which was even higher than the theoretical capacity of the SnO<sub>2</sub> (782 mAh g<sup>-1</sup>). The authors attributed this enormous capacity value to reaction 1, which is usually considered as electrochemically irreversible, but is thermodynamically reversible.



Because the reversibility is influenced by the conductivity of SnO<sub>2</sub> and the size of

Li<sub>2</sub>O and Sn, the nanosized particles in the conductive carbon network made the reaction 1 partially reversible, which increased the theoretical and practical capacity of SnO<sub>2</sub>. In addition, the authors calculated the volume change of SnO<sub>2</sub> during cycling. The result showed that the large volume in CMK-5 can effectively buffer the volume change of 80 wt% of SnO<sub>2</sub>. The cycling performance of 100 % capacity retention after 100 cycles proved their calculation, and showed the advantages of large volume OMCs for the guest anode material's loading. Many other active anode materials, including TiO<sub>2</sub>,<sup>31, 82-84</sup> FeO<sub>x</sub>,<sup>24, 25, 38, 75, 96</sup> MnO<sub>x</sub>,<sup>45, 80, 98</sup> and MoO<sub>2</sub>,<sup>32, 36, 87</sup> are summarized in Table 1.3.

### 1.3.2.2 Cathodic materials

**Table 1. 4 MC based hybrid materials for LIBs cathode**

Materials	Preparing method	Guest wt %	Specific capacity <sup>a</sup>	Cycling stability	Voltage window vs. Li/Li <sup>+</sup>	Ref.
CMK-5/ LiFePO <sub>4</sub>	Impregnation- decomposition	80 %	120 mAh g <sup>-1</sup> (0.017 A g <sup>-1</sup> ) & ~88 mAh g <sup>-1</sup> (0.17 A g <sup>-1</sup> )	> 90 % (0.017 A g <sup>-1</sup> , 50 <sup>th</sup> )	2.5 ~ 4.2 V	54
OMC/ FeF <sub>3</sub>	Impregnation- decomposition	80 %	165 mAh g <sup>-1</sup> (0.0237 A g <sup>-1</sup> ) & 69 mAh g <sup>-1</sup> (2.37 A g <sup>-1</sup> )	91.2 % (0.0237 A g <sup>-1</sup> , 50 <sup>th</sup> )	2 ~ 4.5 V	55
CMK-3/ PQ <sup>b</sup>	Melt-diffusion	31.5 %	220 mAh g <sup>-1</sup> (0.0257 A g <sup>-1</sup> ) & 113 mAh g <sup>-1</sup> (0.514 A g <sup>-1</sup> )	89 % (0.0257 A g <sup>-1</sup> , 50 <sup>th</sup> )	1.8 ~ 3.4 V	65

<sup>a</sup> Based on the total mass of carbon and guest materials.

<sup>b</sup> PQ: Phenanthrenequinone

Compared with anode materials, there are very few cathode materials embedded in OMCs. One reason, as discussed before, is due to less capacity contribution of carbon at high voltage. Another reason is the composite of cathode materials, such as LiMO<sub>2</sub> (M: Mn, Co, or Ni), LiMPO<sub>4</sub> (M: Fe or Mn), and LiMSiO<sub>4</sub> (M: Fe, Co, or Mn) involve

multi-elements, which is difficult to incorporate into carbon frameworks. However, as listed in Table 1.4, several successfully synthesized OMC based composites showed very promising rate performance and cycling stability, which reveals the potential use of OMCs as a cathodic hosting materials in the future.

#### **1.4. Summary and Overview of the Dissertation**

As discussed above, OMCs are good host materials for a variety of active electrochemical materials for supercapacitors and LIBs. The synergic effects between OMCs and guest nanoparticles produce better electrochemical performance than the single component. It is believed that the mesoporous structure, the structural stability, and the material morphology can significantly influence the ion transportation, electronic conductivity, and cycling stability. However, most of the literature focuses on the performance difference between heterogeneous composites and single-phase materials. So far, there was a lack of detailed study focusing on porous structures or material morphology induced electrochemical performance differences for OMC based composites.

In this dissertation, different OMC/Fe<sub>2</sub>O<sub>3</sub> composites were synthesized via the impregnation-decomposition method and were used as a model system to study the relationships between the morphology, the mesostructure, and the electrochemical performance with the emphasis on the porosity and the structure stability. Fe<sub>2</sub>O<sub>3</sub> is chosen due to its low cost, non-toxicity, and high capacitance/capacity for both supercapacitors and LIBs.<sup>109</sup> The impregnation-decomposition method is used because

of its controllable particle growth and wide applicability.

Chapter 2 addresses the influence of mesostructure on the electrochemical performance of OMC/Fe<sub>2</sub>O<sub>3</sub> composite for the supercapacitors' application. Three different structured OMCs, namely 1D *p6mm* FDU-15,<sup>110</sup> 2D *p6mm* CMK-3,<sup>21</sup> and 3D *la3d* CMK-8,<sup>111</sup> were synthesized by soft or hard template methods, and evaluated as host materials for Fe<sub>2</sub>O<sub>3</sub> nanoparticles. Based on the result in the Chapter 2, Chapter 3 developed a soft-hard dual template method to synthesize ordered mesoporous nanowires (OMCNW), which presents the advantages of both soft and hard template carbons and shows better capacitance performance as the host material. Chapter 3 also evaluates the unique 1D nanowires morphology influences on conductivity and ionic diffusion. Chapter 4 extends the application area from the supercapacitor to LIBs, and proves the major findings in Chapter 2 and 3 regarding the porous structure and morphology effects on electrochemical performance are also applicable for LIBs.

## **Chapter 2**

### **Capacitance Behavior of Ordered Mesoporous Carbon/Fe<sub>2</sub>O<sub>3</sub> Composites: Comparison Between 1D Cylindrical, 2D Hexagonal, and 3D Bicontinuous Mesostructures**

## 2.1 Introduction

Since the first synthesis in 1999<sup>112</sup>, ordered mesoporous carbons (OMCs) have been widely used as host materials for metal<sup>12, 113</sup>, metal oxide<sup>56, 59, 92, 114</sup>, sulfur<sup>60</sup>, or polymers<sup>115</sup> for electrochemical sensors<sup>115, 116</sup>, fuel cells<sup>12, 113</sup>, supercapacitors<sup>56, 59, 92, 97, 114, 117</sup>, lithium-ion batteries<sup>37, 43, 46</sup>, Li-O batteries<sup>47</sup>, and Li-S batteries<sup>60</sup> due to their high corrosion resistance, good electrical conductivity, high surface area, large pore volume, and easy handling. In addition, the well-defined porous dimensions were found to enable controlled metal or metal oxide nanoparticles impregnation into the porous scaffold<sup>12</sup>, facilitating higher material utilization for catalysis and energy storage. For example, Shi *et al.*, impregnated MnO<sub>2</sub> nanoparticles into mesoporous CMK-3 carbon and demonstrated a capacitance of 600 F g<sup>-1</sup> MnO<sub>2</sub><sup>56</sup>. Similarly, many other metal oxide nanoparticles, such as Nb<sub>2</sub>O<sub>5</sub><sup>92</sup>, Fe<sub>2</sub>O<sub>3</sub><sup>59</sup>, and Cu<sub>2</sub>O<sup>114</sup> showed enhanced electrochemical performances when impregnated into mesoporous CMK-3, compared to their pristine oxide counterparts. The enhanced performance was attributed not only to the better conductivity and small particle size, but also to the well-defined pore structure which facilitated the rapid ion mobility via meso-channels.

To date, most of the OMC related composites were based on CMK-3 which is made by mesoporous silica SBA-15 as hard template<sup>12, 37, 47, 56, 59, 113-117</sup>. The mesostructure of CMK-3 is maintained by the inter-pillars nano-bridges which were derived from the micropores (< 2nm) in the original silica templates<sup>21</sup>. These nano-bridges are very fragile upon heterogeneous nanoparticle loading process, which could

potentially break the mesostructure of CMK-3 and will further affect the accessibility of active species and electrochemical performance. However, this mesostructure stability issue has never been investigated.

Along with the stability, it is expected that other porous parameters of OMCs can also influence the electrochemical performance of OMC based composites, especially pore shape which can strongly affect ion mobility inside the pores. Therefore, a systematically comparison of electrochemical behaviors between different structured OMC composites is essential for a better understanding of the effects of pore structures on the performance. However, very few reports deal with non-CMK-3 composites and they all lack detailed investigation of the mesostructure's influence on the application<sup>43, 46, 60, 92, 97</sup>. Hence it is important to design controlled experiments with various OMCs structures synthesized and tested under similar conditions in order to better understand and optimize OMCs related composites based on their structure stabilities and porosities.

Iron oxide is one of the cheapest common oxides with very low toxicity and high theoretical capacity, which made it a good candidate for anodes in Li- or Na- ion batteries<sup>118</sup>. Furthermore, the operating voltage window for iron oxide faradaic activity is lower than other commonly used metal oxides, which makes it one of the promising anode materials for high energy density asymmetrical supercapacitors<sup>119</sup>. Additionally, studies have shown that the capacitive performance of iron oxide strongly depends on the ion mobility<sup>120, 121</sup>. In light of that, we chose OMC/iron oxide composites as the

model system to study the influence of structure on ion mobility and electrochemical performance.

In this work, we have synthesized 1D *p6mm* FDU-15<sup>110</sup>, 2D *p6mm* CMK-3<sup>21</sup>, and 3D *Ia3d* CMK-8<sup>111</sup> by soft or hard template methods, and impregnated different amounts of Fe<sub>2</sub>O<sub>3</sub> nanoparticles inside the mesopores using a uniform nanoparticle loading procedure. The pore structures and stabilities were characterized by N<sub>2</sub> adsorption–desorption and transmission electron microscopy (TEM), and the effect of structure on ion mobility was studied by electrochemical impedance spectroscopy (EIS). The capacitance performance of different mesostructures with different Fe<sub>2</sub>O<sub>3</sub> % was evaluated by cyclic voltammetry (CV) and the relationships among mesostructure, pore stability, ion mobility, and electrochemical performance were systematically investigated.

## **2.2 Experiment section.**

### **2.2.1 Materials Preparation.**

Different synthesis processes of OMCs are illustrated in Figure 2.1.

1D cylindrically structured FDU-15 was synthesized by a soft template method according to Ref.<sup>110</sup>, using triblock copolymer Pluronic F127 (EO<sub>106</sub>PO<sub>70</sub>EO<sub>106</sub>, MW=12600) as structure directing reagent and urea and formaldehyde as the carbon source. In a typical process, 1 g F127 was dissolved in 8.0 g ethanol. Then 5 g of 20 % resol precursors prepared by the literature method<sup>110</sup>, were added to the solution. The

mixture was stirred for 1 h and then transferred to a glass Petri dish, and left for 5–8 h at room temperature and 24 h at 100 °C to evaporate the ethanol. Then the gel was thermopolymerized in a 180 °C oven for 12 h. The as-made product was collected and ground into fine powder. Calcination was carried out in a tubular furnace at 600 °C for 3 h and subsequently 900 °C for 2 h under Ar flow. The heating rates were 1 °C min<sup>-1</sup> below 600 °C and 5 °C min<sup>-1</sup> above 600 °C.

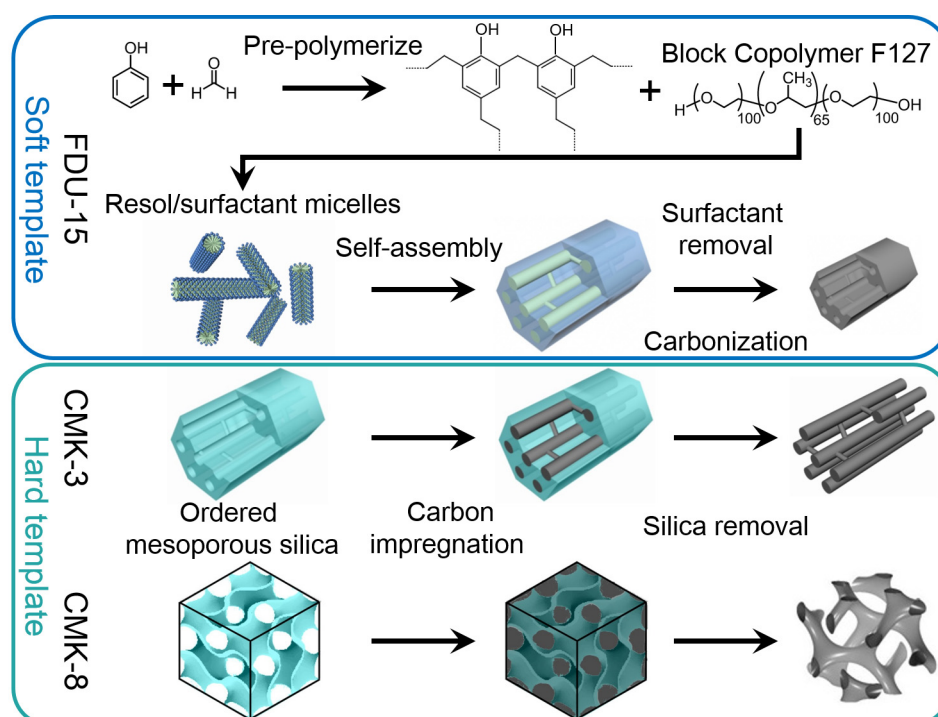


**Figure 2. 1 Synthesis processes of FDU-15, CMK-3, and CMK-8.**

2D hexagonally structured CMK-3 was synthesized by using mesoporous silica SBA-15 as a hard template<sup>21</sup>. The detailed synthesis method of SBA-15 was described in Ref.<sup>122</sup>. The carbon nanocasting process was as follows: 1.2 g of SBA-15 was added to a solution made of 1.5 g sucrose, 0.17 g of H<sub>2</sub>SO<sub>4</sub>, and 6 g H<sub>2</sub>O. The mixture was dried in oven at 100 °C for 6 h, and subsequently 160 °C for another 6 h. The silica

sample containing partially carbonized sucrose was treated again with a mixture of 0.96 g of sucrose, 0.11 g of H<sub>2</sub>SO<sub>4</sub> and 6 g of H<sub>2</sub>O, followed by a same drying process at 100 °C and 160 °C. The carbonization was carried out in a tubular furnace at 600 °C for 3 h, and subsequently 900 °C for 4 h under Ar flow, the heating rates were 1 °C min<sup>-1</sup> below 600 °C and 5 °C min<sup>-1</sup> above 600 °C. The silica was etched away by a 3 M NaOH solution three times at 50 °C. The template-free carbon product thus obtained was centrifuged and washed by D. I. water.

3D bicontinuous CMK-8 was also synthesized by a hard template method, with mesoporous silica KIT-6 as a template. The KIT-6 was synthesized according to Ref. <sup>123</sup>, with the molar ratio of 0.017 P123 / 1.67 TEOS / 1.67 *n*-butanol / 1.83 HCl / 195 H<sub>2</sub>O. The carbon nanocasting process was similar to CMK-3, with adjusted sucrose and sulfuric acid amounts to fit the pore volume of KIT-6. In brief, 1.2 g of KIT-6 was infiltrated by 1.17 g sucrose, 0.13 g of H<sub>2</sub>SO<sub>4</sub>, and 4.7 g H<sub>2</sub>O. After drying in an oven at 100 °C for 6 h, and 160 °C for another 6 h, the sample was treated again by a mixture of 0.62 g of sucrose, 0.07 g of H<sub>2</sub>SO<sub>4</sub> and 3.85 g of H<sub>2</sub>O, followed by the same drying process at 100 °C and 160 °C. The annealing process and silica removal processes were the same as CMK-3.

To improve the hydrophilicity of mesoporous carbon before electrochemical testing or Fe<sub>2</sub>O<sub>3</sub> loading, all three kinds of mesoporous carbon were treated with 70 % HNO<sub>3</sub> at 60 °C for 1 h and subsequently washed by D. I. water.

In order to grow Fe<sub>2</sub>O<sub>3</sub> nanoparticles inside mesopores, the carbons were soaked

in an  $\text{Fe}(\text{NO}_3)_3$  aqueous solution and a low pressure vacuum filtration process was used to remove any extra salt solution outside the mesopores. The mesoporous carbon with  $\text{Fe}(\text{NO}_3)_3$  solution was heated to 100 °C for 6 h to evaporate water, followed by 190 °C annealing in argon flow for 5 h to decompose  $\text{Fe}(\text{NO}_3)_3$  into  $\text{Fe}_2\text{O}_3$ . The loading amount of  $\text{Fe}_2\text{O}_3$  was controlled by the concentration of  $\text{Fe}(\text{NO}_3)_3$  solutions, which ranged from 3 % to 45 %. The final products were noted as FDU-15-x, CMK-3-x, and CMK-8-x, where x was the weight % of  $\text{Fe}_2\text{O}_3$  measured by ICP-OES.

### **2.2.2 Characterization.**

X-ray diffraction (XRD) patterns were recorded by Bruker Smart1000 (Bruker AXS Inc., USA) using  $\text{CuK}\alpha$  radiation. XPS analysis was done on a Kratos AXIS 165 spectrometer. The C 1s peak was calibrated at 284.8 eV. Images of OMCs and OMC/ $\text{Fe}_2\text{O}_3$  composites were acquired using a transmission electron microscopy (JEOL JEM 2100 FE-TEM).

Nitrogen ( $\text{N}_2$ ) adsorption-desorption isotherms were recorded with a Micromeritics ASAP 2020 Porosimeter Test Station. Samples were degassed (in vacuum) at 100 °C for 12 hours before the test. The specific surface areas were calculated using the BET method from the nitrogen adsorption data in the relative pressure range ( $P/P_0$ ) of 0.05–0.20. The porosity distribution was calculated from adsorption branch using the BJH (Barrett–Joyner–Halenda) equation.

The loading amount of  $\text{Fe}_2\text{O}_3$  was determined by inductively coupled plasma-

atomic emission spectroscopy (ICP-AES) characterization performed on a Perkin Elmer ICP Optima 4700. Intensities were measured at 259.939 nm for Fe. OMC/Fe<sub>2</sub>O<sub>3</sub> samples were dissolved in a freshly prepared concentrated HCl/ethanol solution and diluted to a known volume before being administered to the plasma. The final concentration of HCl and ethanol were 2 % and 0.8 %, respectively.

### **2.2.3 Electrochemical Measurement**

All the electrochemical studies were performed in a standard three-electrode system utilizing a bipotentiostat electrochemical test station (BI-STAT, Princeton Applied Research). The electrolyte was 1 M Na<sub>2</sub>SO<sub>3</sub> aqueous solution. Ag/AgCl was used as the reference electrode and glassy carbon was used as the counter electrode. To make the working electrode, a slurry of the mesoporous material, carbon black, and a poly-(vinylidene fluoride) (PVDF) binder at a weight ratio of 85:10:5 dispersed in N-Methyl-2-pyrrolidone (NMP) was cast onto a stainless steel foil with a loading of 0.5–1.0 mg/cm<sup>2</sup> using a doctor blade. After an overnight drying in a vacuum oven at 100 °C, the active materials were pressed on a nickel foam current collector. The potential window was -0.8 V to 0 V vs. Ag/AgCl. Electrochemical impedance spectroscopy (EIS) was also conducted with a frequency range from 20 kHz to 10 mHz at -0.15 V vs. Ag/AgCl.

All specific capacitance values were obtained using the data from the cyclic voltammetry (CV) curves through the following equation (the capacitance of Ni current

collector has been subtracted):

$$C_{sp} = \frac{\int_{-0.8}^0 IdV + \int_0^{-0.8} IdV}{2 \times 0.8 \times v \times mass} \quad (2.1)$$

where  $I$  is the current,  $V$  is the voltage vs. Ag/AgCl, 0.8 V is the voltage window,  $v$  is the scan rate, and  $mass$  is the mass of the mesoporous material.

## 2.3 Results and discussions

### 2.3.1 Structural and Textural Characterization of different structures

#### OMC/Fe<sub>2</sub>O<sub>3</sub> composites

X-ray photoelectron spectroscopy (XPS) was used to determine the valence state of the iron oxide. In order to get a good intensity, the samples with highest Fe<sub>2</sub>O<sub>3</sub> % were characterized and the results in the Fe 2p spectra region are shown in Figure 2.2. Regardless of the mesostructures, all of the samples show similar spectra; the broader peaks at 711 eV, 719 eV and 724 eV were in agreement with the reported value for Fe<sub>2</sub>O<sub>3</sub><sup>124</sup>. Due to the low anneal temperature of 190 °C and the small particle size, the Fe<sub>2</sub>O<sub>3</sub> nanoparticles have poor crystallinity and no peak can be detected by XRD (data not shown).

The mesostructure of the three different OMCs and their derived OMC/Fe<sub>2</sub>O<sub>3</sub> composites were compared by N<sub>2</sub> adsorption–desorption isotherms. The black curves in Figure 2.3 a-c shows isotherms of OMCs, which are all type-IV curves with typical mesoporous characteristics at P/P<sub>0</sub> of 0.4-0.6<sup>125</sup>. The pore parameters of OMCs are listed in Table 2.1. Although the pore diameter of CMK-3 (3.2 nm) is smaller than that

of FDU-15 and CMK-8 (3.8 nm), the difference is fairly small, and is not expected to dramatically affect Fe<sub>2</sub>O<sub>3</sub> loading and capacitance performance. It is noteworthy that the CMK-3 and CMK-8 made by hard template method have much larger surface area than the soft templated FDU-15. Additionally, the pore volume of CMK-3 (0.907 cm<sup>3</sup> g<sup>-1</sup>) and CMK-8 (1.178 cm<sup>3</sup> g<sup>-1</sup>) are about 2 fold higher than FDU-15 (0.327 cm<sup>3</sup> g<sup>-1</sup>). The small pore volume of FDU-15 limits the possible loading amount of Fe<sub>2</sub>O<sub>3</sub>, hence, the highest mass loading of Fe<sub>2</sub>O<sub>3</sub> in FDU-15 was only 20 %, compare with nearly 50 % Fe<sub>2</sub>O<sub>3</sub> content in the other two OMCs.

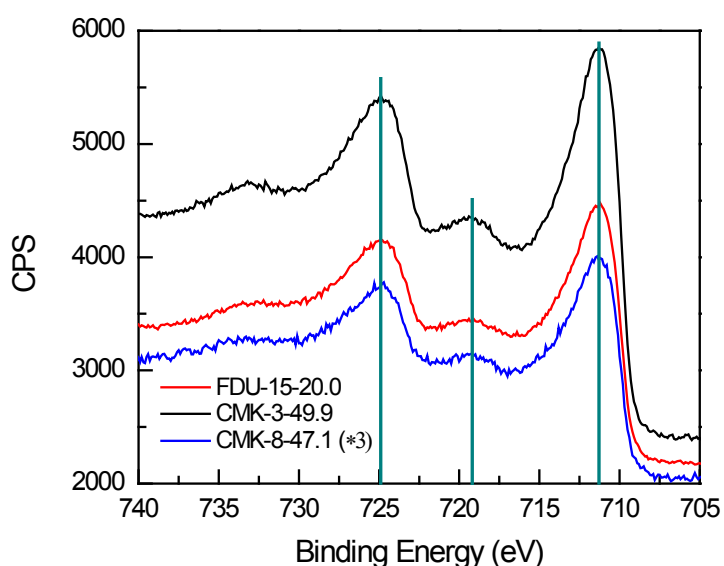


**Figure 2. 2 XPS spectrums of OMC/Fe<sub>2</sub>O<sub>3</sub> composites.**

Intensity of sample CMK-8-47.1 was multiplied by three in order to better reflect the peaks.

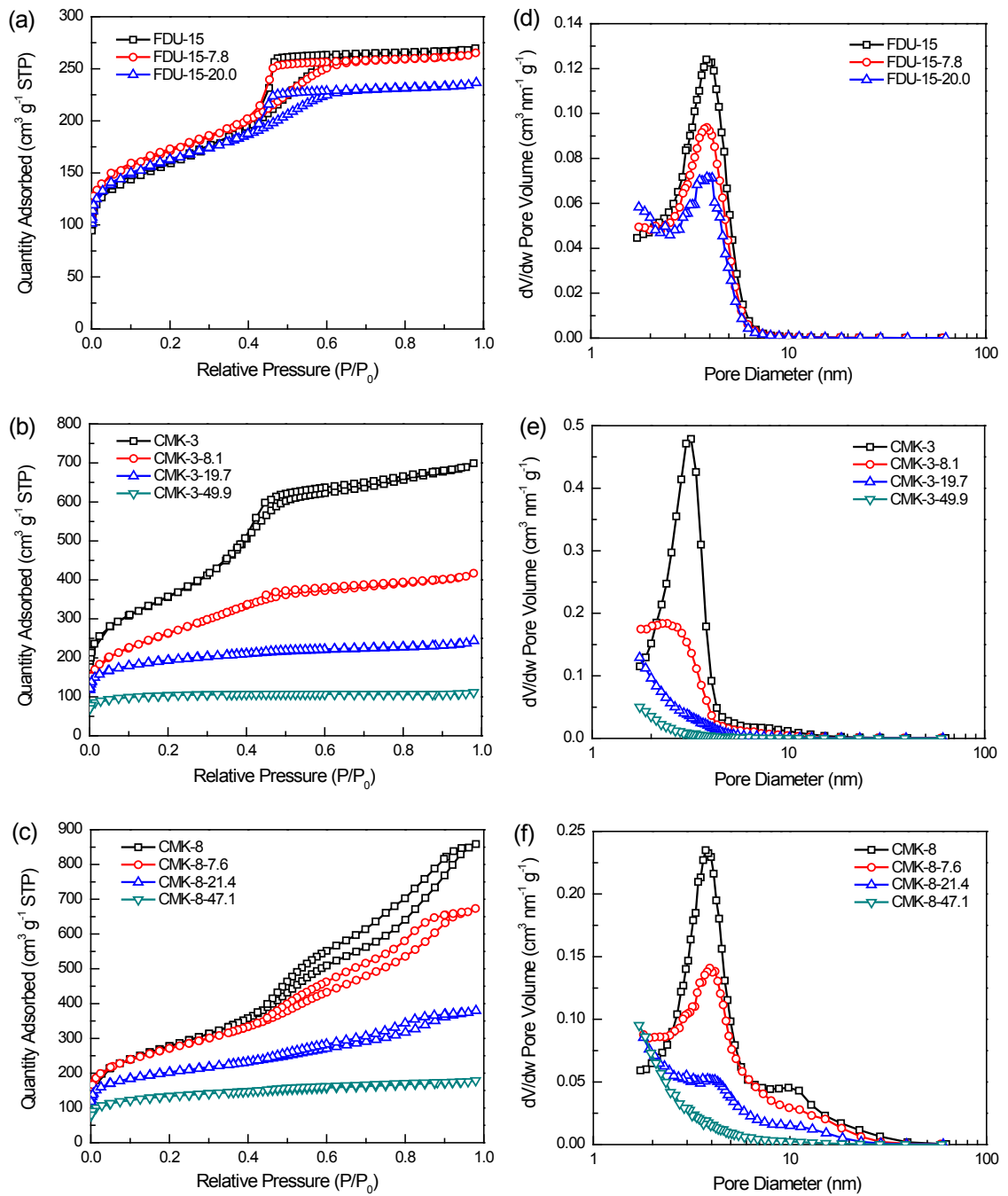


**Figure 2. 3 N<sub>2</sub> adsorption–desorption isotherms and pore size distributions of OMCs and their derived composites:**

(a-c) N<sub>2</sub> adsorption–desorption isotherms, (d-f) pore size distributions.

The trend of structure change upon impregnation of Fe<sub>2</sub>O<sub>3</sub> into various OMCs

were characterized by N<sub>2</sub> adsorption–desorption, which are shown in Figure 2.3 a-c. Based on the isotherms, the pore size distributions and detailed structure parameters are calculated and presented in Figure 2.3 d-f and in Table 2.1, respectively. Upon Fe<sub>2</sub>O<sub>3</sub> loading, the microporous volume did not change much in all of three mesostructures, indicating that the Fe<sub>2</sub>O<sub>3</sub> was mainly formed in the mesopores. For the 1D mesoporous FDU-15 based materials, pore diameters remained stable but there was a small decrease of mesopore volume which occurred with the increase of Fe<sub>2</sub>O<sub>3</sub> %. However, for the 3D mesoporous CMK-8 based composites, a dramatic decrease of mesopore volume happened during Fe<sub>2</sub>O<sub>3</sub> loading, and the mesoporosity disappeared at Fe<sub>2</sub>O<sub>3</sub> % of 47.1 %. The pore size and mesopore volume was even more significantly decreased in the 2D mesoporous CMK-3 based materials, and the composite lost its mesoporosity at only 19.7 % of Fe<sub>2</sub>O<sub>3</sub> content.

In order to quantitatively characterize the variation of mesopore volume in different mesostructures during Fe<sub>2</sub>O<sub>3</sub> incorporation, we have calculated the absolute ( $\Delta V_{meso}$ ) and relative ( $\Delta V_{meso} \%$ ) mesopore volume difference between OMC/Fe<sub>2</sub>O<sub>3</sub> composites and their corresponding OMCs through the following equations:

$$\Delta V_{meso} = V_{meso-C} - V_{meso-CFe} / (1 - Fe_2O_3 \%) \quad (2.2)$$

$$\Delta V_{meso} \% = \frac{\Delta V_{meso}}{V_{meso-C}} \times 100 \quad (2.3)$$

Here,  $V_{meso-CFe}$  and  $V_{meso-C}$  are mesopore volume of OMC/Fe<sub>2</sub>O<sub>3</sub> composite and mesopore volume of pure OMC,  $Fe_2O_3 \%$  is the mass percentage of Fe<sub>2</sub>O<sub>3</sub> in the OMC/Fe<sub>2</sub>O<sub>3</sub> composite, so that  $V_{meso-CFe} / (1 - Fe_2O_3 wt\%)$  is the mesopore

volume of OMC/Fe<sub>2</sub>O<sub>3</sub> composite normalized by the initial carbon mass.

**Table 2. 1 N<sub>2</sub> adsorption–desorption properties of OMCs & OMC/Fe<sub>2</sub>O<sub>3</sub> composites\***

Sample ID	$d$ (nm)	$S_t$ (m <sup>2</sup> g <sup>-1</sup> )	$V_t$ (cm <sup>3</sup> g <sup>-1</sup> )	$V_{meso}$ (cm <sup>3</sup> g <sup>-1</sup> )	$V_{micro}$ (cm <sup>3</sup> g <sup>-1</sup> )	$\Delta V_{meso}$ (cm <sup>3</sup> g <sup>-1</sup> )	$\Delta V_{meso}$ (%)
FDU-15	3.8	554	0.327	0.311	0.016	-	-
FDU-15-7.8	3.9	593	0.263	0.248	0.015	0.043	13.8
FDU-15-20.0	3.8	564	0.216	0.199	0.017	0.064	20.7
CMK-3	3.2	1266	0.907	0.873	0.034	-	-
CMK-3-8.1	2.4	819	0.442	0.392	0.050	0.448	51.3
CMK-3-19.7	< 1.7	672	0.184	0.147	0.037	0.692	79.2
CMK-3-49.9	< 1.7	380	0.032	0.020	0.012	0.834	95.6
CMK-8	3.8	992	1.178	1.158	0.020	-	-
CMK-8-7.6	3.9	958	0.858	0.836	0.022	0.256	22.1
CMK-8-21.4	3.8	707	0.415	0.394	0.021	0.661	57.1
CMK-8-47.1	< 1.7	469	0.153	0.123	0.030	0.932	80.5

\* All data are calculated from adsorption branch:

$d$ : pore diameter;

$S_t$  and  $V_t$ : total surface area and pore volume;

$V_{meso}$ : mesopore (2 nm <  $d$  < 50 nm) volume;

$V_{micro}$ : micropore ( $d$  < 2 nm) volume;

$\Delta V_{meso}$ : mesopore volume change after Fe<sub>2</sub>O<sub>3</sub> loading based on carbon mass.

$\Delta V_{meso}$  %: normalized mesopore volume change after Fe<sub>2</sub>O<sub>3</sub> loading based on original carbon.

The detailed data are listed in Table 2.1. Considering the densities of Fe<sub>2</sub>O<sub>3</sub> nanoparticles are same regardless of the host material mesostructures, the mesopores'

volume decrease should be similar in different OMCs. However, the trend of mesoporosity lost was quite different between soft templated OMC (FDU-15) and hard templated OMCs (CMK3 and CMK-8). For same level of  $\text{Fe}_2\text{O}_3$  %, the  $\Delta V_{meso}$  of FDU-15/ $\text{Fe}_2\text{O}_3$  was one order of magnitude lower than  $\Delta V_{meso}$  of CMK-3/ $\text{Fe}_2\text{O}_3$  and CMK-8/ $\text{Fe}_2\text{O}_3$ . Therefore, some factor other than  $\text{Fe}_2\text{O}_3$  accommodation was responsible for the mesoporosity decrease in the hard templated OMCs/ $\text{Fe}_2\text{O}_3$ .

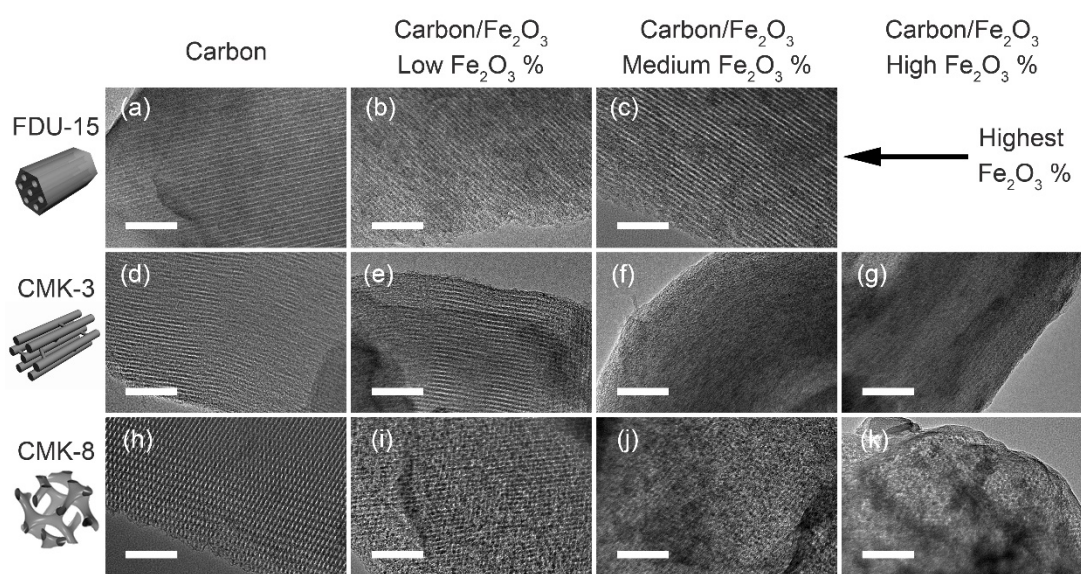


**Figure 2. 4 TEM images of different meso-structures OMCs & OMC/ $\text{Fe}_2\text{O}_3$  composites.**

(a) FDU-15, (b) FDU-15-7.8, (c) FDU-15-20.0, (d) CMK-3, (e) CMK-3-8.1, (f) CMK-3-19.7, (g) CMK-3-49.9, (h) CMK-8, (i) CMK-8-7.6, (j) CMK-8-21.4, and (k) CMK-8-47.1. All scale bars are 100 nm.

TEM was carried out to further investigate the influence of  $\text{Fe}_2\text{O}_3$  impregnation on the evolution of the OMCs' mesostructure. Figure 2.4 compared TEM images of the three different OMCs with various loading amounts of  $\text{Fe}_2\text{O}_3$ . As demonstrated, FDU-

15 maintained its parallel mesostructure, while the ordered mesoporous architecture of CMK-3 and CMK-8 degraded upon impregnation of oxide material. The clear loss of the ordered mesostructure after loading of 19.7 % of Fe<sub>2</sub>O<sub>3</sub> in CMK-3 (Figure 2.4f) and 47.1 % of Fe<sub>2</sub>O<sub>3</sub> in CMK-8 (Figure 2.4k) is in very good agreement with the results obtained from the N<sub>2</sub> adsorption–desorption isotherms discussed above, hence we attribute the change of pore volume and pore size distribution to the destruction of the mesoporous architecture upon loading of oxide.

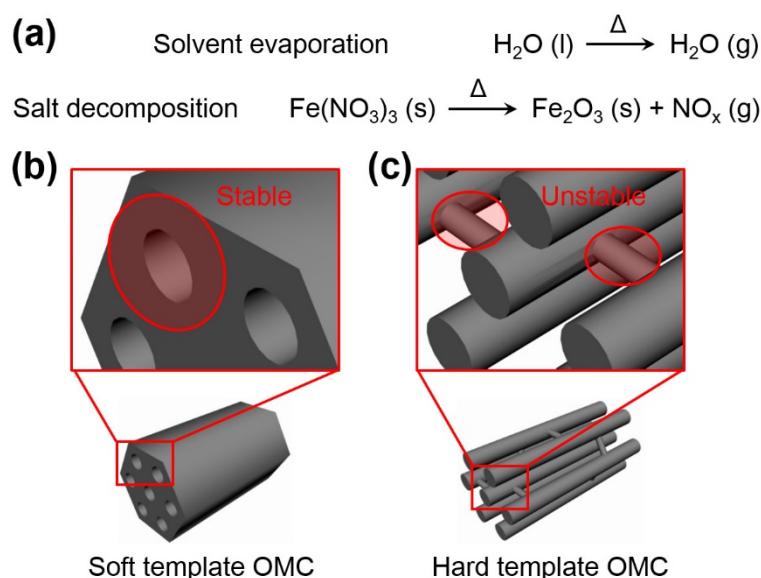


**Figure 2. 5 Schematic illustration of different mesostructure stabilities.**

(a) chemical reactions during Fe<sub>2</sub>O<sub>3</sub> loading processes, (b) soft template OMC architecture, (c) hard template OMC architecture.

Considering the results from N<sub>2</sub> adsorption-desorption and TEM together, it is clear that the different mesostructure variations were caused by the different stabilities of the carbon framework. As shown in Figure 2.5b, for 1D FDU-15 made by the soft template method, the carbon is reported to grow around the surfactant micelles, which

formed the rigid arch-like carbon network<sup>110</sup>. On the other hand, for the 2D CMK-3 and 3D CMK-8 made from the hard template method, the adjacent pillars in CMK-3 or two sets of carbon networks in CMK-8 were connected by nano-bridges which were derived from the micropores (< 2 nm) in the original SBA-15 or KIT-6 silica templates (Figure 2.5c)<sup>20, 21</sup>. We attribute the destruction of the mesoporous structure in the 2D and 3D OMCs to the fragility of those nano-bridges: during the solvent evaporation or salt decomposition in Fe<sub>2</sub>O<sub>3</sub> growth process, the released gases (H<sub>2</sub>O and NO<sub>x</sub>) as well as volume changes during the Fe(NO<sub>3</sub>)<sub>3</sub> to Fe<sub>2</sub>O<sub>3</sub> transformation (Figure 2.5a) could easily break the nano-bridges and cause the collapse of mesoporous architecture. While in FDU-15, the rigid carbon framework could prevent the collapse and maintain the structure and pore size. Furthermore, when comparing the  $\Delta V_{meso}$  % of the two types of hard template derived OMCs, it is noteworthy that more mesopores volume was kept in CMK-8/Fe<sub>2</sub>O<sub>3</sub>, indicating a more stable mesostructure in CMK-8. This might be because the 3D carbon network in CMK-8 can help to maintain the mesostructure after the inter-framework bridge collapse. Overall, the mesostructure stability upon Fe<sub>2</sub>O<sub>3</sub> loading is 1D FDU-15 > 3D CMK-8 > 2D CMK-3. The trend of structural stability is also evident in the surface area variation between OMCs and their derived OMC/Fe<sub>2</sub>O<sub>3</sub>. For FDU-15, when introducing small amount of Fe<sub>2</sub>O<sub>3</sub> nanoparticles in the mesopores, the inner surface roughness of mesopores is increased, leading to a larger surface area of FDU-15-7.8 than FDU-15. Further increases in Fe<sub>2</sub>O<sub>3</sub> loading then slightly decrease surface area due to the increased nanoparticle size and composite density. However, in

the case of the CMK-3 and CMK-8 systems, owing to the unstable mesostructures, the rapid loss of mesoporosity leads to dramatically decreased surface areas which overwhelm any surface roughness increase with increased Fe<sub>2</sub>O<sub>3</sub> %.

## **2.3.2 Electrochemical studies of different structures of OMC/Fe<sub>2</sub>O<sub>3</sub> composites**

### **2.3.2.1 Electrochemical impedance spectroscopy (EIS) studies of mesostructure's influence on ion mobility**

EIS was used to evaluate the effects of mesostructure on the ion mobility inside the mesoporous systems. Figure 2.6 a-c shows Nyquist plots of OMCs and OMC/Fe<sub>2</sub>O<sub>3</sub> composites. Qualitatively, all plots are similar in shape, beginning with a semi-circle or arc at high frequencies, followed by a straight line inclined at an angle of around 45° to the real axis in the medium frequency region, and a nearly vertical line in the low frequency region. Previous work suggested that such a pattern of the EIS can be fit by an equivalent Randles circuit<sup>119, 121, 126-129</sup>, as shown in the inset of Figure 2.6a.

Comparing different samples, the solution resistance ( $R_s$ ) showed similar values (~ 2.2 Ω) for all the measured EIS. For the materials with same mesostructure, the charge transfer resistance ( $R_{ct}$ ) slightly increased with raising Fe<sub>2</sub>O<sub>3</sub> % in the OMC/Fe<sub>2</sub>O<sub>3</sub> composites. This is because the Faradaic processes at Fe<sub>2</sub>O<sub>3</sub> are normally slower than the ion adsorption at the carbon surface. Comparison of different mesostructured OMC/Fe<sub>2</sub>O<sub>3</sub> composites with similar Fe<sub>2</sub>O<sub>3</sub> %, *e.g.*, FDU-15-7.8,

CMK-3-8.1, and CMK-8-7.6, demonstrated very similar  $R_{ct}$  values, indicating comparable redox reactivity of  $\text{Fe}_2\text{O}_3$  among these samples.

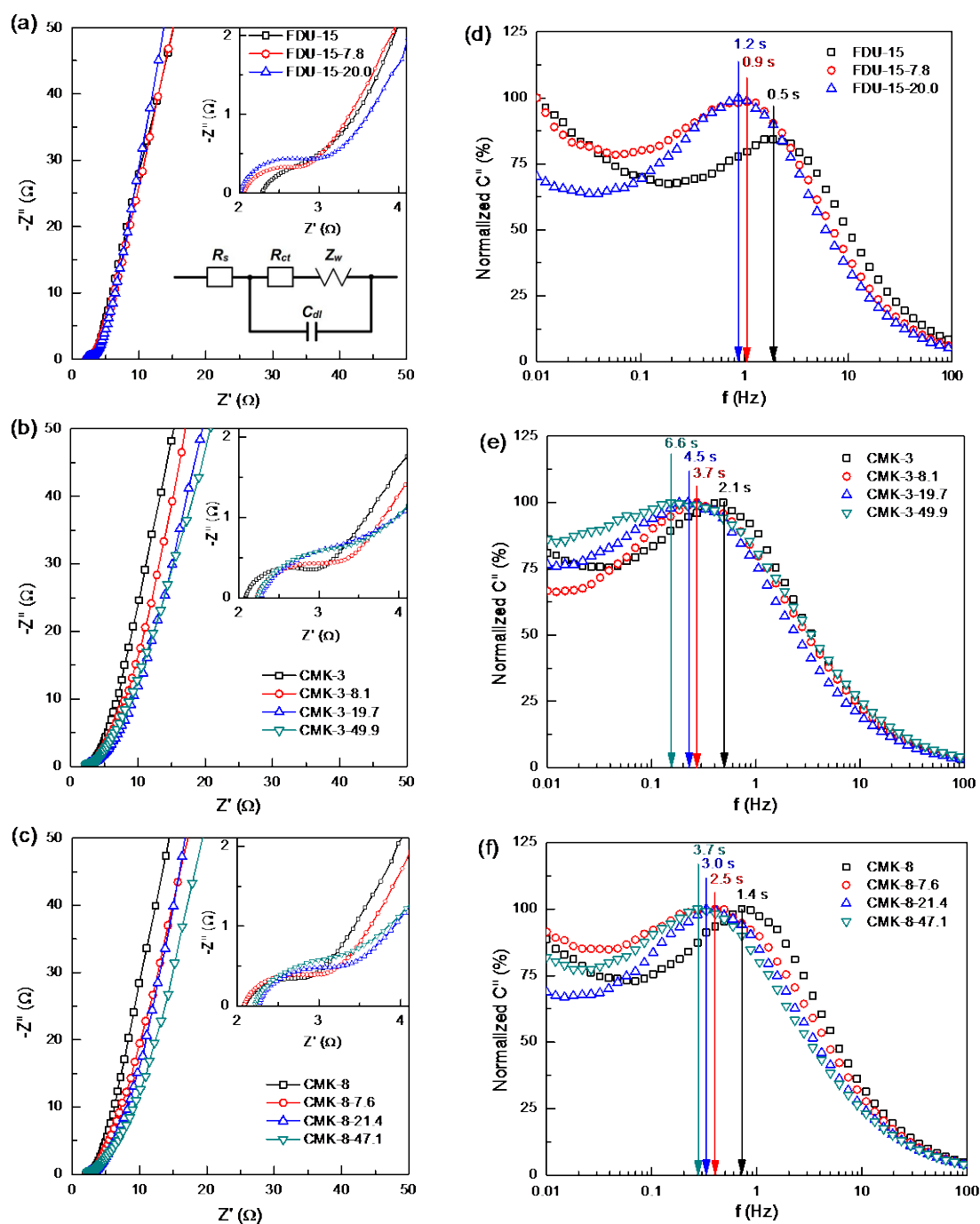


**Figure 2. 6 Nyquist plots and Bode plots for different OMCs and their composites.**

(a-c) Nyquist plots, (d-f) Bode plots. Inset of (a): the equivalent Randles circuit.

The straight line with 45° angle at the medium frequency region ascribes to the Warburg impedance ( $Z_w$ ), which reflects the ion transportation process in the porous electrode. As listed in Table 2.2, unlike  $R_s$  and  $R_{ct}$ ,  $Z_w$  were quite different in each sample, implying a large difference of ion mobility in diverse pore architectures. The trend of  $Z_w$  in the various OMCs is 1D FDU-15 (0.8Ω) < 3D CMK-8 (2.0 Ω) < 2D CMK-3 (2.5 Ω), indicating better ionic mobility in the 1D mesostructure. This is because of the small tortuosity of 1D channels ( $\sim 1$ ) compared with 2D and 3D structures ( $> 1$ ). Introducing Fe<sub>2</sub>O<sub>3</sub> would add surface roughness which will slightly increase the tortuosity of the mesopores, and should lead to a small decrease in the ion mobility inside the pores. As expected, the  $Z_w$  increased in FDU-15-7.8 (1.4 Ω) and FDU-15-20.0 (2.1 Ω). However, the value of  $Z_w$  in FDU-15/Fe<sub>2</sub>O<sub>3</sub> was still very small even compared with bare CMK-3 and CMK-8, indicating that a clear ionic pathway was maintained in the FDU-15 structure, even at high mass loading amounts. On the contrary, in the 2D CMK-3, which is the least stable structure, the ion transportation rapidly decreased with addition of Fe<sub>2</sub>O<sub>3</sub> nanoparticles. The  $Z_w$  of CMK-3-8.1 and CMK-3-19.7 were 5.2 Ω and 6.5 Ω, which were more than 3 times larger than FDU-15-7.8 and FDU-15-20.0, respectively. This implies significant loss of ion mobility caused by the greatly increased tortuosity in the collapsed CMK-3 structure. In the 3D mesoporous CMK-8 structure, the value of  $Z_w$  in CMK-8-7.6 (4.3 Ω), CMK-8-21.4 (5.4 Ω) and CMK-8-47.1 (6.8 Ω) was slightly smaller than in CMK-3/Fe<sub>2</sub>O<sub>3</sub> with similar Fe<sub>2</sub>O<sub>3</sub> content, but still much larger than in FDU-15/Fe<sub>2</sub>O<sub>3</sub> composites. This

observation is consistent with a moderate tortuosity increase which would be expected from the disruption of the 3D mesoporous network with medium stability.

**Table 2. 2 EIS parameters for different OMCs & OMC/Fe<sub>2</sub>O<sub>3</sub> composites**

Sample ID	$R_s$ ( $\Omega$ )	$R_{ct}$ ( $\Omega$ )	$Z_w$ ( $\Omega$ )	$\tau$ (s)
FDU-15	2.3	0.6	0.8	0.5
FDU-15-7.8	2.1	0.9	1.4	0.9
FDU-15-20.0	2.0	1.1	2.1	1.2
CMK-3	2.1	1.0	2.5	2.1
CMK-3-8.1	2.2	1.1	5.2	3.7
CMK-3-19.7	2.3	1.3	6.5	4.5
CMK-3-49.9	2.2	1.3	7.6	6.6
CMK-8	2.1	0.9	2.0	1.4
CMK-8-7.6	2.1	1.0	4.3	2.5
CMK-8-21.4	2.3	1.1	5.4	3.0
CMK-8-47.1	2.2	1.3	6.8	3.7

Another important parameter for ion mobility is the dielectric relaxation time constant ( $\tau$ ), which provides a measure for the rate capability and ion transport through a porous electrode. Generally, a small  $\tau$  means faster ion mobility in the pores. As shown in Figure 2.6 d-f,  $\tau$  can be deduced from the Bode plot of the imaginary capacitance,  $C''(\omega)$ , in which  $\tau$  is the inverse of relaxation frequency ( $f_R$ ), which is the frequency at the maximum  $C''$ . The  $C''(\omega)$  can be calculated according to the following equation:

$$C''(\omega) = \frac{Z'(\omega)}{\omega|Z(\omega)|^2} \quad (2.4)$$

where  $\omega$  is the angular frequency,  $Z'(\omega)$  is the real part of impedance, and  $|Z(\omega)|$  is the impedance modulus.<sup>127, 128, 130</sup> The time constant of different mesoporous materials are listed in Table 2.2. The change of  $\tau$  can be attributed to  $R_{ct}$  and  $Z_w$  and reflects conjugation of both parameters. Hence, for same mesostructures,  $\tau$  will increase with an increase of  $\text{Fe}_2\text{O}_3$  %. Additionally, the FDU-15 series samples showed the smallest  $\tau$  less than 1.2 s, even compared with pure hard templated carbon CMK-3 (2.1 s) and CMK-8 (1.4 s), indicating again, that the well preserved 1D channels of FDU-15 facilitate ion mobility. In addition, at similar  $\text{Fe}_2\text{O}_3$  %, the 3D CMK-8 had a smaller  $\tau$  than 2D CMK-3, which supports other observations that the 3D structure is more stable than the 2D structure.

### **2.3.2.2 Influence of mesostructure on capacitance performance – electrochemical behavior of bare mesoporous carbons**

We first investigated the capacitance performance of bare mesoporous carbons without loading of  $\text{Fe}_2\text{O}_3$  to study the effect of pore shape on the ion mobility within the pores. The black curves in Figure 2.7 a-c shows the cyclic voltammetry (CV) of different structured OMCs at scan rate of  $5 \text{ mV s}^{-1}$ . All of OMCs showed relatively flat, rectangular-shaped CV curves, which are typical for electrochemical double-layer capacitors<sup>131, 132</sup>. Based on the CV curves, the specific capacitances of FDU-15, CMK-3, and CMK-8 at scan rate of  $5 \text{ mV s}^{-1}$  are 87, 126, and  $113 \text{ F g}^{-1}$ , respectively, which is a trend mostly determined by their total surface area. The corresponding specific

capacitances by total surface area are 15.7, 10.0, and 11.4  $\mu\text{F cm}^{-2}$  for FDU-15, CMK-3, and CMK-8, respectively, which are in the same range of the reported OMCs' capacitances<sup>2, 133-136</sup>. The relative area capacitance values of FDU-15 > CMK-8 > CMK-3 are in good agreement with the previous comparison studies between different structured OMCs<sup>133, 134, 137</sup>.

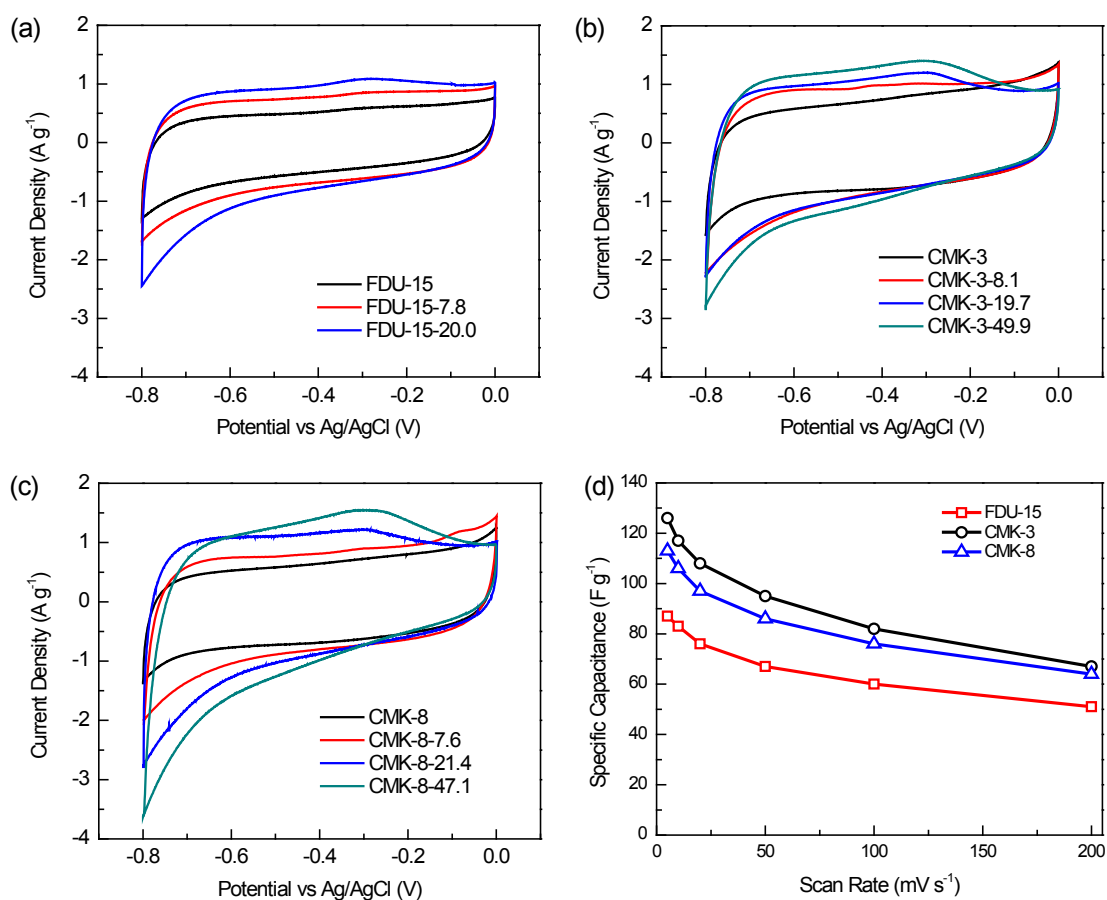


**Figure 2. 7 Cyclic Voltammetry curves and specific capacitances of different OMCs and their derived composites.**

(a-c) CV curves at scan rate of 5 mV s<sup>-1</sup>, (d) specific capacitances at different scan rates.

Figure 2.7d present the capacitance of the various OMCs as a function of the scan-rate. Although the capacitance of 1D FDU-15 is smaller than the other two OMCs, the

capacitance retention between  $5 \text{ mV s}^{-1}$  and  $200 \text{ mV s}^{-1}$  ( $C_{200\text{mV}}/C_{5\text{mV}}$ ) of the FDU-15 (59 %) was higher than CMK-3 (53 %) and CMK-8 (57 %), indicates faster ion mobility in the 1D mesoporous FDU-15, which is in very good agreement with the trends found for  $Z_w$  and  $\tau$  values in the EIS measurements.

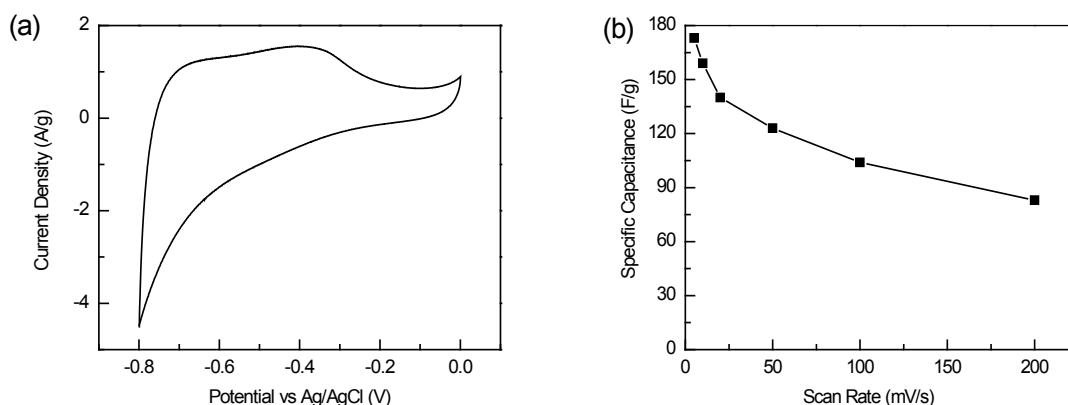


**Figure 2. 8 CV curve and Specific capacitance of mesoporous Fe<sub>2</sub>O<sub>3</sub>.**

(a) CV curve in 1M Na<sub>2</sub>SO<sub>3</sub> at scan rate of  $5 \text{ mV s}^{-1}$ , (b) Specific capacitance at different scan rate. The mesoporous Fe<sub>2</sub>O<sub>3</sub> was synthesized using SBA-15 as hard template and Fe(NO<sub>3</sub>)<sub>2</sub> as iron source.

### 2.3.2.3 Influence of mesostructure stability on capacitance performance – electrochemical behavior of OMC with loading of Fe<sub>2</sub>O<sub>3</sub>

Figure 2.7 a-c compared the CV curves of OMCs and OMC/Fe<sub>2</sub>O<sub>3</sub> composites. As the Fe<sub>2</sub>O<sub>3</sub> % increases, the CV curves gradually deviate from the ideal rectangular shape of EDLCs, mostly due to the broad peaks at  $\sim -0.3 \text{ V}$  and  $< -0.6 \text{ V}$ , which are typical for iron oxide in Na<sub>2</sub>SO<sub>3</sub> aqueous electrolyte<sup>120, 138-142</sup> and are due to the redox reactions between sulfite anions adsorbed on Fe<sub>2</sub>O<sub>3</sub> and redox reactions between Fe(II) and Fe(III)

The capacitances of three types of mesoporous carbons with various loading amounts of Fe<sub>2</sub>O<sub>3</sub> (~ 8 % to ~ 50 %) at different scan rates are presented in Figure 2.9 a-c. Based on the Fe<sub>2</sub>O<sub>3</sub> loading amount and capacitance difference of carbon and carbon/Fe<sub>2</sub>O<sub>3</sub>, the specific capacitance of Fe<sub>2</sub>O<sub>3</sub> can be calculated from the following equation:

$$C_{Fe_2O_3} = \frac{C_{total} - C_C \times (1 - Fe_2O_3 \%) }{Fe_2O_3 \%} \quad (2.5)$$

In which  $C_{Fe_2O_3}$ ,  $C_C$ , and  $C_{total}$  are specific capacitances of Fe<sub>2</sub>O<sub>3</sub>, OMC, and the OMC/Fe<sub>2</sub>O<sub>3</sub> composite, respectively, and  $Fe_2O_3 \%$  is the mass percentage of Fe<sub>2</sub>O<sub>3</sub> in the OMC/Fe<sub>2</sub>O<sub>3</sub> composite. The calculated Fe<sub>2</sub>O<sub>3</sub> capacitances as function of loading amount are shown in Figure 2.9 d-f.

Even with only ~8 % of Fe<sub>2</sub>O<sub>3</sub>, the electrode gained 30-50 % increase in the total capacitance from the Fe<sub>2</sub>O<sub>3</sub> contribution. The demonstrated capacitances attributed to Fe<sub>2</sub>O<sub>3</sub> in all of our OMCs, *e.g.*, FDU-15-7.8 (677 F g<sup>-1</sup>), CMK-8-7.6 (587 F g<sup>-1</sup>), and CMK-3-8.1 (570 F g<sup>-1</sup>), were much higher than the values previously reported for Fe<sub>3</sub>O<sub>4</sub> nanoparticles (37.9 F g<sup>-1</sup> <sup>129</sup> and 174 F g<sup>-1</sup> <sup>142</sup>), Fe<sub>3</sub>O<sub>4</sub>/Fe<sub>2</sub>O<sub>3</sub> films (118.2 F g<sup>-1</sup> <sup>138</sup> and 210 F g<sup>-1</sup> <sup>140</sup>), Fe<sub>3</sub>O<sub>4</sub> in CNT/Fe<sub>3</sub>O<sub>4</sub> composites (128 F g<sup>-1</sup> <sup>143</sup>), and even for mesoporous Fe<sub>2</sub>O<sub>3</sub> synthesized by same method but without carbon (173 F g<sup>-1</sup>, Figure 2.8). Hence, we demonstrate that loading of Fe<sub>2</sub>O<sub>3</sub> into the mesoporous OMCs induced synergic effect in which the conductive carbon scaffold, with free ionic mobility in the

mesoporous structure, enabled optimized utilization of Fe<sub>2</sub>O<sub>3</sub> capacitance.

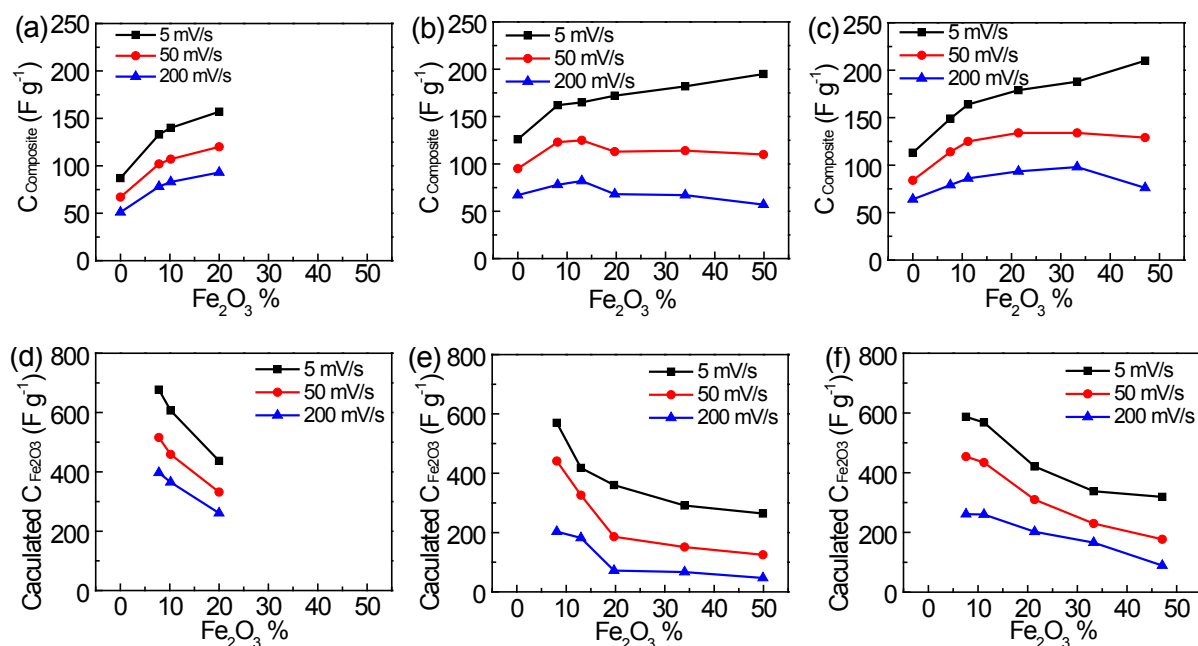


**Figure 2. 9 Specific capacitance of OMCs, OMC/Fe<sub>2</sub>O<sub>3</sub> composites, and calculated capacitance of Fe<sub>2</sub>O<sub>3</sub>.**

(a-c) Specific capacitance of OMCs and OMC/Fe<sub>2</sub>O<sub>3</sub> composites in (a) FDU-15 system, (b) CMK-3 system, and (c) CMK-8 system, (d-f) calculated capacitance of Fe<sub>2</sub>O<sub>3</sub> with different Fe<sub>2</sub>O<sub>3</sub> % in (d) FDU-15 system, (e) CMK-3 system, and (f) CMK-8 system, the scan rates are 5 mV s<sup>-1</sup>, 50 mV s<sup>-1</sup>, and 200 mV s<sup>-1</sup>.

As the specific capacitance of metal oxide is much higher than mesoporous carbon, there is incentive to load as much oxide as possible into the carbon scaffold. However, due to the small pore volume of FDU-15, the highest possible Fe<sub>2</sub>O<sub>3</sub> loading amount is only 20 %. Therefore, only the capacitances of low and medium Fe<sub>2</sub>O<sub>3</sub> % are presented in FDU-15/Fe<sub>2</sub>O<sub>3</sub> samples. On the contrary, CMK-8 and CMK-3 benefit from their larger pore volume and can achieve up to ~ 50 % of Fe<sub>2</sub>O<sub>3</sub> loading. Our results showed

that with the highest Fe<sub>2</sub>O<sub>3</sub> loading, the iron oxide enabled 50-90 % increase in the total capacitance of the electrode at slow scan rates. On the other hand, as been reported previously in OMC/MnO<sub>2</sub><sup>58</sup> and nitrogen-enriched mesoporous carbons/RuO<sub>2</sub> systems<sup>144</sup>, loading larger amounts of guest metal oxides will decrease the pore volume and may clog the pores, induce formation of larger oxide particles, and hinder the ion mobility and electrolyte penetration into the composite. This is clearly demonstrated in Figure 2.9 d-f, which show the decreased  $C_{Fe_2O_3}$  with increasing Fe<sub>2</sub>O<sub>3</sub> %, regardless of mesostructure.

Additionally, due to the different structure stability, it is expected that the electrochemical performance of 1D, 2D, and 3D mesostructured OMC/Fe<sub>2</sub>O<sub>3</sub> composites behave differently with increasing Fe<sub>2</sub>O<sub>3</sub> %. This is proved by comparing values of  $C_{Fe_2O_3}$  and rate performances of the composites in different mesostructures.

In the 1D mesoporous FDU-15/Fe<sub>2</sub>O<sub>3</sub>, the capacitances at medium and high scan rates kept increasing with the addition of more Fe<sub>2</sub>O<sub>3</sub> (Figure 2.9a). Regardless of Fe<sub>2</sub>O<sub>3</sub> content, the  $C_{200mV}/C_{5mV}$  was 59%, which is same as pure FDU-15. Even at rate of 200 mV s<sup>-1</sup>, the calculated Fe<sub>2</sub>O<sub>3</sub> capacitance in the highest Fe<sub>2</sub>O<sub>3</sub> loaded sample FDU-15-20.0 was 261 F g<sup>-1</sup>. We attribute this positive trend to the stability of the mesostructure as demonstrated by the TEM and N<sub>2</sub> adsorption–desorption isotherms.

On the contrary, in the commonly used 2D CMK-3 system, as observed in N<sub>2</sub> adsorption–desorption and TEM, most of the mesopores were collapsed before Fe<sub>2</sub>O<sub>3</sub> content increased to ~20 %. Zhi's group<sup>145</sup> reported that in the range of 1.5 nm – 3 nm,

decrease in pore size will strongly prohibit the ion accessibility in the mesopores. In CMK-3 samples, the pore diameter dramatically decreased from 3.2 nm in CMK-3 to less than 1.7 nm in CMK-3-19.7. This pore size decreases together with a reduction of pore volume which results in a composite capacitance drop between 12.6 % and 19.7 % under medium and high scan rates (Figure 2.9b). The  $C_{200\text{mV}}/C_{5\text{mV}}$  of 2D mesoporous composite dropped from 53 % in CMK-3, to 40 % in CMK-3-19.7. The calculated  $\text{Fe}_2\text{O}_3$  capacitance in CMK-3-19.7 was  $190 \text{ F g}^{-1}$  and  $72 \text{ F g}^{-1}$  at  $50 \text{ mV s}^{-1}$  and  $200 \text{ mV s}^{-1}$  (Figure 2.9e), which were only 56% and 27% of the values in FDU-15-20.0 at the same scan rates. This is in agreement with the prohibited ion mobility detected by EIS. Although CMK-3 can load a large amount of  $\text{Fe}_2\text{O}_3$ , due to the completely collapsed mesopores, the capacitance of CMK-3-49.9 is even smaller than pure CMK-3 at the rate of  $200 \text{ mV s}^{-1}$ , which results in only 29 % of the  $C_{200\text{mV}}/C_{5\text{mV}}$ . This small capacitance and poor rate performance can also attributed to the hindered ion transportation in the collapsed mesopores, which leading to less utilization of both  $\text{Fe}_2\text{O}_3$  and carbon.

In the case of 3D mesoporous CMK-8/ $\text{Fe}_2\text{O}_3$ , which has moderate structure stability and ion accessibility, both composite capacitance and calculated  $\text{Fe}_2\text{O}_3$  capacitance stand between FDU-15/ $\text{Fe}_2\text{O}_3$  and CMK-3/ $\text{Fe}_2\text{O}_3$ . The CMK-8-21.4 has 179 and  $93 \text{ F g}^{-1}$  of total capacitance at  $5 \text{ mV s}^{-1}$  and  $200 \text{ mV s}^{-1}$ , which results in 52 % of  $C_{200\text{mV}}/C_{5\text{mV}}$ . Compared with 57 % of  $C_{200\text{mV}}/C_{5\text{mV}}$  in CMK-8, the moderate decrease of  $C_{200\text{mV}}/C_{5\text{mV}}$  is due to the partially broken 3D porous system. However, as revealed

by N<sub>2</sub> adsorption–desorption and TEM, at highest loading of 47.1 %, most of the mesopores have collapsed, resulting in a small pore volume and < 1.7 nm pore diameter, which is similar as CMK-3-19.7. Therefore, although CMK-8-47.1 shows 210 F g<sup>-1</sup> total capacitance at 5 mV s<sup>-1</sup>, it only preserves 36 % of that capacitance at 200 mV s<sup>-1</sup> due to the limited ion accessibility.

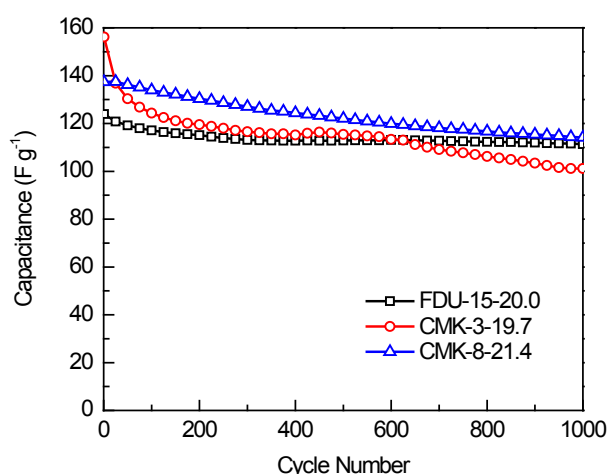


**Figure 2. 10 Cycling performances of FDU-15-20.0, CMK-3-19.7, and CMK-8-21.4 in 1 M Na<sub>2</sub>SO<sub>3</sub> solution at current density of 5 A g<sup>-1</sup>.**

The above discussion clearly reveals the correlations between structural stability and rate performance. Beside rate performance, the cycling performance is also expected to be influenced by the structure stability. Here, the cycling stabilities of medium Fe<sub>2</sub>O<sub>3</sub> loaded samples were evaluated by galvanostatic charge-discharge method at current density of 5 A g<sup>-1</sup>. From Figure 2.20, after 1000 cycles, the capacitance retention of FDU-15-20.0, CMK-8-21.4, and CMK-3-19.7 are 89.8 %, 83.1 %, and 64.8%, respectively, which is in good agreement with their structure stability.

## 2.4 Conclusion

Three OMCs with 1D cylindrical, 2D hexagonal, and 3D bicontinuous symmetries were synthesized and used as host materials for OMC/Fe<sub>2</sub>O<sub>3</sub> composites. The influences of mesostructure and structure stability on the ion mobility were systematically characterized, and their effects on capacitance performance were fully studied. Our results show that although the high surface area and pore volume lead to a large carbon capacitance and Fe<sub>2</sub>O<sub>3</sub> % in 2D mesoporous CMK-3, the intrinsically unstable mesostructure results in an unfavorable ionic accessibility and bad rate performance. On the other hand, 1D mesoporous FDU-15 from a soft template method has the most stable structure and provides the best structure for ion mobility. Therefore, when loaded with Fe<sub>2</sub>O<sub>3</sub>, it has the best rate performance, cycling stability, and Fe<sub>2</sub>O<sub>3</sub> specific capacitance. The surface area and stability of the 3D CMK-8/Fe<sub>2</sub>O<sub>3</sub> composites is between the above two materials, so that it can achieve the highest total capacitance at low scan rate. But the unstable mesostructure limited their high rate performance, especially for the high Fe<sub>2</sub>O<sub>3</sub> % samples. Clearly, there is a trade-off between ion transportation, mesostructure stability, and structural parameters such as surface area, pore size, and pore volume. In order to get a better electrochemical performance of mesoporous carbon/metal oxide composite, an ideal host material should combine the advantages of both soft template OMCs and hard template OMCs to maximize surface area and pore volume, while also maximizing structural stability and ion access.

## **Chapter 3**

### **Dual-Template Synthesis of Ordered Mesoporous**

### **Carbon/Fe<sub>2</sub>O<sub>3</sub>Nanowires: High Porosity and Structural Stability for**

### **Supercapacitors**

### 3.1 Introduction

Electrochemical capacitors (ECs), also called supercapacitors, have attracted great interest due to their high specific power with reasonable energy density and excellent cycling stability. In general, the ECs can be categorized into electric double layer capacitors (EDLCs) and pseudocapacitors via their different charge-storage modes.<sup>2,3</sup> The EDLCs are mainly made from carbon based materials and the energy is stored by the charge separation at the electrode/electrolyte interface;<sup>2</sup> while the pseudocapacitors are mostly composed of transition metal oxide which store charges by fast Faradaic processes involving electrochemical redox reactions.<sup>3,4</sup> The specific capacitance of EDLCs is limited by the total surface area of the electrode and typically not very high.<sup>103,146</sup> The specific capacitance of pseudocapacitors, where redox reactions are involved, can utilize the inner part of materials and is not limited by surface area, hence it is anticipated to be higher than EDLCs.<sup>6-8</sup> However, the most important consideration of supercapacitors is their high specific power, which is limited severely by the low conductivity of the metal oxides used in most of pseudocapacitors. One strategy to obtain both specific high power and high energy is the fabrication of heterogeneous carbon/metal oxide composites for ECs, as demonstrated in many previous reports.<sup>147-150</sup> Among numerous carbon materials, ordered mesoporous carbons (OMCs) are good candidates as the host materials for the heterogeneous energy storage composites.<sup>50,56,59,92,97,114,117</sup> This is due to their intrinsic properties, such as large electrical conductivity, high porosity, high surface area, high corrosion resistance, and easy

handling. In addition, the confined metal oxide nanoparticle dimensions inside the mesopores could facilitate higher material utilization for electrochemical redox reactions.<sup>12</sup>

In general, there are two typical strategies to synthesize OMCs:<sup>14</sup> the hard template method which uses ordered porous solids, such as mesoporous silica,<sup>15</sup> silica colloid,<sup>16</sup> and anodized aluminum oxide (AAO),<sup>17</sup> for casting a mold of the carbon replica; and the soft template method which uses surfactant micelles as the structure directing reagent.<sup>18</sup> The soft template method was demonstrated to preserve the desired mesoscale architecture of the hosting carbon material. However, due to the low surface area and pore volume of the carbon made by this method,<sup>134, 151</sup> the loading of oxide and the energy density are still limited.<sup>44</sup> The hard templated carbons are reported to have larger pore volume and surface area,<sup>136</sup> which leads to higher mass loading of oxide and higher energy.<sup>58, 114</sup> However, the mesopore architecture of the hosting carbon gradually collapses upon oxide loading, which prevented the full utilization of the inner part of the materials and limits their high rate performances.<sup>44</sup> Clearly, the soft or hard templated OMC/Fe<sub>2</sub>O<sub>3</sub> composites have their own intrinsic drawbacks and merits. An ideal host OMC should have both the larger surface area and pore volume and the stable structural to achieve both high energy and power densities.

Besides the porous structure, the particle size and morphology of carbon can also influence the electrochemical performance. Xia's group<sup>152</sup> and Chen's group<sup>153</sup> have compared the electrochemical performance of ordered mesoporous carbon CMK-3 with

different particle lengths and the results have shown that the shorter length results in higher capacitance and rate performance due to their short pathway for rapid ion diffusion. Similarly, Chan's group<sup>154</sup> have synthesized mesoporous hollow carbon spheres with different shell thickness, and found that spheres with thicker shells have hindered rate performance, due to poor ion transport. Clearly, decreasing particle size can help to shorten the ionic transport distance and improve the electrochemical performance. However, reduced particle size can also increase the number of solid-solid interfaces and will decrease electronic connectivity. To overcome this, 1D nanowire morphology is very promising due to short ion access pathways through the small nano-scale radius and efficient charge transport along its micro-scale axis.<sup>5, 6, 155, 156</sup> However, to the best of our knowledge, the structure and energy storage properties of ordered porous carbon/metal oxide nanowires have not yet been investigated.

Using a dual template strategy presented herein we synthesized ordered mesoporous carbon nanowires (OMCNW) that demonstrate the advantages of both the soft and hard template method by achieving a high pore volume and surface area with stable mesoporous structure. Furthermore, for the 1<sup>st</sup> time, we incorporated Fe<sub>2</sub>O<sub>3</sub> nanoparticles into the OMCNW to fabricate OMCNW/metal oxide composites. The dual template strategy provides the opportunity to produce optimized structural characteristics which are not accessible using any single template. Here, the combination of the unique nanowire morphology provided by the hard template and mesopores provided by the soft and hard templates facilitates high Fe<sub>2</sub>O<sub>3</sub> loading along

with excellent ionic mobility. These structural features directly contribute to the high carbon and Fe<sub>2</sub>O<sub>3</sub> capacitance, excellent rate performance and long cycle life of the OMCNWs.

## **3.2 Materials and Methods**

### **3.2.1 Materials Preparation**

Dual template ordered mesoporous nanowires were prepared similarly as soft template FDU-15,<sup>44</sup> except that AAO membrane was used as hard template (Figure 3.1). In general, 0.5 g F127 was dissolved in 4.0 g ethanol. Then 3.75 g of 20 % resol precursors prepared by literature method<sup>110</sup> were added to the solution. The mixture was stirred for 1 h and then transferred to a glass Petri dish with an ethanol pre-wetted AAO, and left for 5–8 h at room temperature and 24 h at 100 °C to evaporate the ethanol. Then the gel was thermopolymerized in an 180 °C oven for 12 h, and the top resin outside of AAO was removed by a stainless steel blade. The remaining AAO with the resin inside the pores were annealed in a tubular furnace at 600 °C for 3 h and subsequently 900 °C for 2 h under Ar flow. The heating rates were 1 °C min<sup>-1</sup> below 600 °C and 5 °C min<sup>-1</sup> above 600 °C. The AAO membrane was dissolved by 3 M NaOH at 140 °C for 8 h in an autoclave, and the residual product was washed by distilled water several times.

For comparison, soft templated FDU-15 and hard templated CMK-8 were chosen from our previous work,<sup>44</sup> using triblock copolymer Pluronic F127 ( $\text{EO}_{106}\text{PO}_{70}\text{EO}_{106}$ , MW=12600) and mesoporous silica KIT-6 as structure directing reagent, respectively.

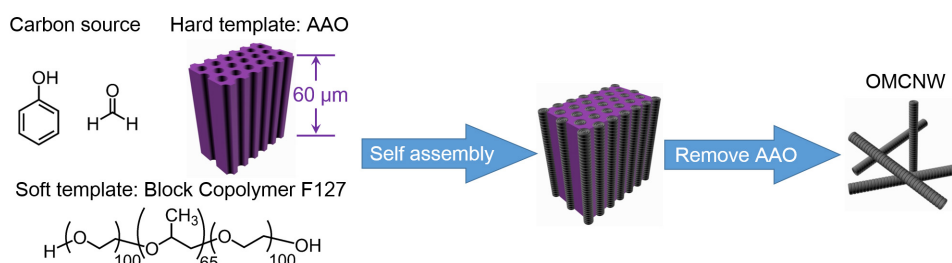


**Figure 3. 1 Synthesis processes of OMCNW.**

To improve the hydrophilicity of OMCs, before electrochemical testing or  $\text{Fe}_2\text{O}_3$  loading, all three kinds of OMCs were treated with 70%  $\text{HNO}_3$  at 60  $^\circ\text{C}$  for 1 h and subsequently washed by D. I. water. In order to grow  $\text{Fe}_2\text{O}_3$  nanoparticles inside mesopores, the carbons were soaked in a 45 %  $\text{Fe}(\text{NO}_3)_3$  aqueous solution and a low pressure vacuum filtration process was used to remove any extra salt solution outside the mesopores. The mesoporous carbon with  $\text{Fe}(\text{NO}_3)_3$  solution was heated to 100  $^\circ\text{C}$  for 6 h to evaporate water, followed by 190  $^\circ\text{C}$  annealing in argon flow for 5 h to decompose  $\text{Fe}(\text{NO}_3)_3$  into  $\text{Fe}_2\text{O}_3$ . The final products were noted as OMCNW-54.2, FDU-15-20.0, and CMK-8-47.1, where the last numbers were the weight percentages of  $\text{Fe}_2\text{O}_3$  measured by ICP-OES.

### 3.2.2 Characterization

X-ray diffraction (XRD) patterns were recorded by Bruker Smart1000 (Bruker AXS Inc., USA) using  $\text{CuK}\alpha$  radiation. XPS analysis was done on a Kratos AXIS 165

spectrometer. The C 1s peak was calibrated at 284.8 eV. Images of mesoporous carbon and carbon/Fe<sub>2</sub>O<sub>3</sub> composites were acquired using a scanning electron microscopy (Hitachi SU-70 SEM, operated at an acceleration voltage of 5 kV) and a transmission electron microscopy (JEOL JEM 2100 FE-TEM, 200 kV).

Nitrogen (N<sub>2</sub>) adsorption-desorption isotherms were recorded with a Micromeritics ASAP 2020 Porosimeter Test Station. Samples were degassed (in vacuum) at 100 °C for 12 hours before the test. The specific surface areas were calculated using the BET method from the nitrogen adsorption branch in the relative pressure range (P/P<sub>0</sub>) of 0.05–0.20. The porosity distribution was calculated from adsorption branch using the BJH (Barrett–Joyner–Halenda) equation.

The loading amount of Fe<sub>2</sub>O<sub>3</sub> was determined by inductively coupled plasma-atomic emission spectroscopy (ICP-AES) characterization performed on a Perkin Elmer ICP Optima 4700. Intensities were measured at 259.939 nm for Fe. Mesoporous carbon/Fe<sub>2</sub>O<sub>3</sub> samples were dissolved in a freshly prepared concentrated HCl/ethanol solution and diluted to a known volume before being administered to the plasma. The final concentration of HCl and ethanol were 2 % and 0.8 %, respectively.

### **3.2.3 Electrochemical Measurement**

All the electrochemical studies were performed in a standard three-electrode system utilizing a bipotentiostat (BI-STAT, Princeton Applied Research) electrochemical test station. The electrolyte was 1 M Na<sub>2</sub>SO<sub>3</sub> aqueous solution.

Ag/AgCl was used as the reference electrode and glassy carbon was used as the counter electrode. To make the working electrode, a slurry of the mesoporous material, carbon black, and a poly-(vinylidene fluoride) (PVDF) binder at a weight ratio of 85:10:5 was cast onto a stainless steel foil with a loading of 0.5–1.0 mg/cm<sup>2</sup> using a doctor blade. After an overnight drying in a vacuum oven at 100 °C, the active materials were pressed on a nickel foam current collector. The potential window was -0.8 V to 0 V vs. Ag/AgCl. Electrochemical impedance spectroscopy (EIS) was also conducted with a frequency range from 20 kHz to 10 mHz at -0.15 V vs. Ag/AgCl.

### **3.3 Results and Discussions**

#### **3.3.1 Morphological and Structural Characterization**

The structure and electrochemical performance of dual templated OMCNW/Fe<sub>2</sub>O<sub>3</sub> were compared with soft template only FDU-15/Fe<sub>2</sub>O<sub>3</sub>, which was prepared using the same soft template in the OMCNW but without the hard template, AAO. The dual-templated structure was also compared to a hard template only structure, CMK-8/Fe<sub>2</sub>O<sub>3</sub>, which has previously been shown to have the best overall performance among different mesostructured OMC/Fe<sub>2</sub>O<sub>3</sub>.<sup>44</sup>

Figure 3.2 presents SEM images of the three types of OMCs and OMC/Fe<sub>2</sub>O<sub>3</sub> composites. When using the soft and hard template methods, as shown in Figure 3.2 a-d, carbon materials with irregular shape were obtained. Additionally, loading of those OMCs with Fe<sub>2</sub>O<sub>3</sub> does not affect the morphology.

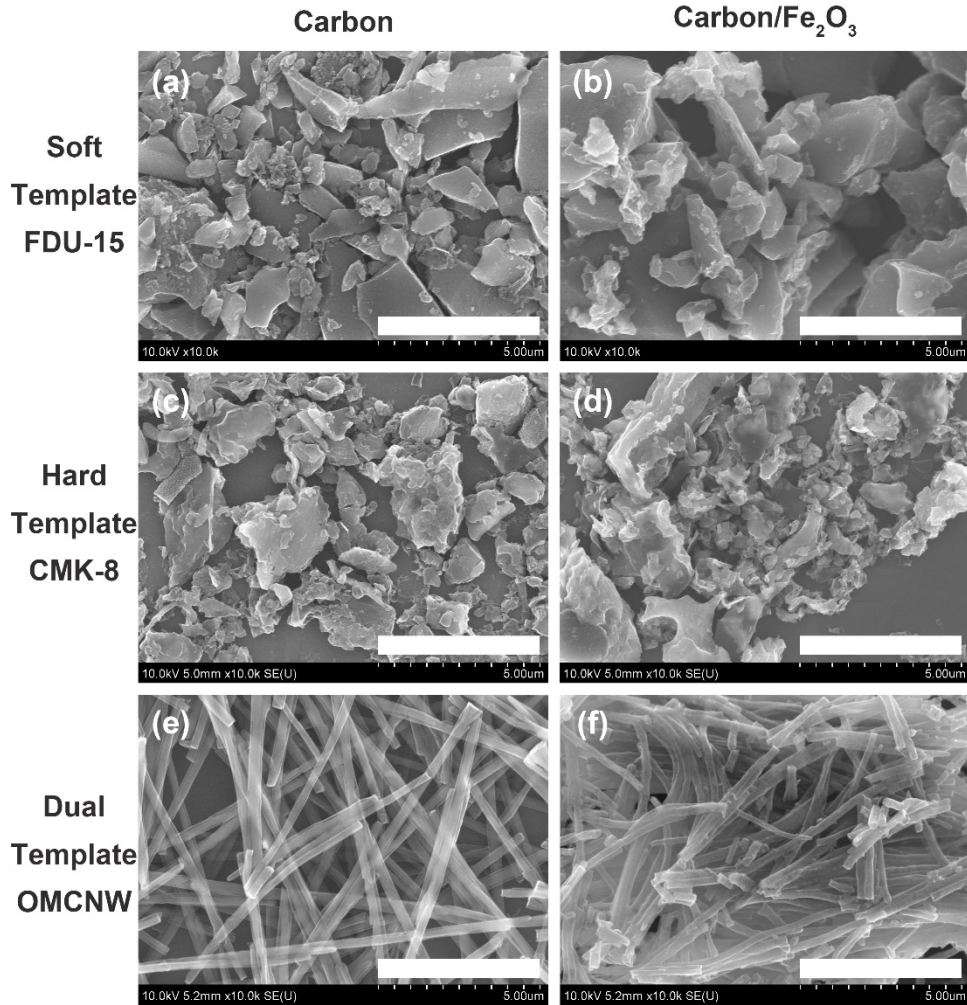


**Figure 3. 2 SEM images of different OMCs & OMC/Fe<sub>2</sub>O<sub>3</sub> composites with distinct morphologies:**

(a) FDU-15, (b) FDU-15-20.0, (c) CMK-8, (d) CMK-8-47.1, (e) OMCNW, (f) OMCNW-54.2. All scale bars are 5  $\mu$ m.

The material produced using the dual template strategy has a well-defined nanowire morphology with around 200 nm diameter and more than 10  $\mu$ m length which is consistent with the original hard template pore dimensions (Figure 3.2e). This suggests that the surfactant induced growth within the pores of the AAO hard template.

Furthermore, as clearly demonstrated in Figure 3.2f, the morphology of the OMCNWs was maintained even after the impregnation of the oxide. No  $\text{Fe}_2\text{O}_3$  particles can be detected outside the nanowires, indicating the selective growth of  $\text{Fe}_2\text{O}_3$  nanoparticles inside the mesoporous system in the impregnation-decomposition processes.

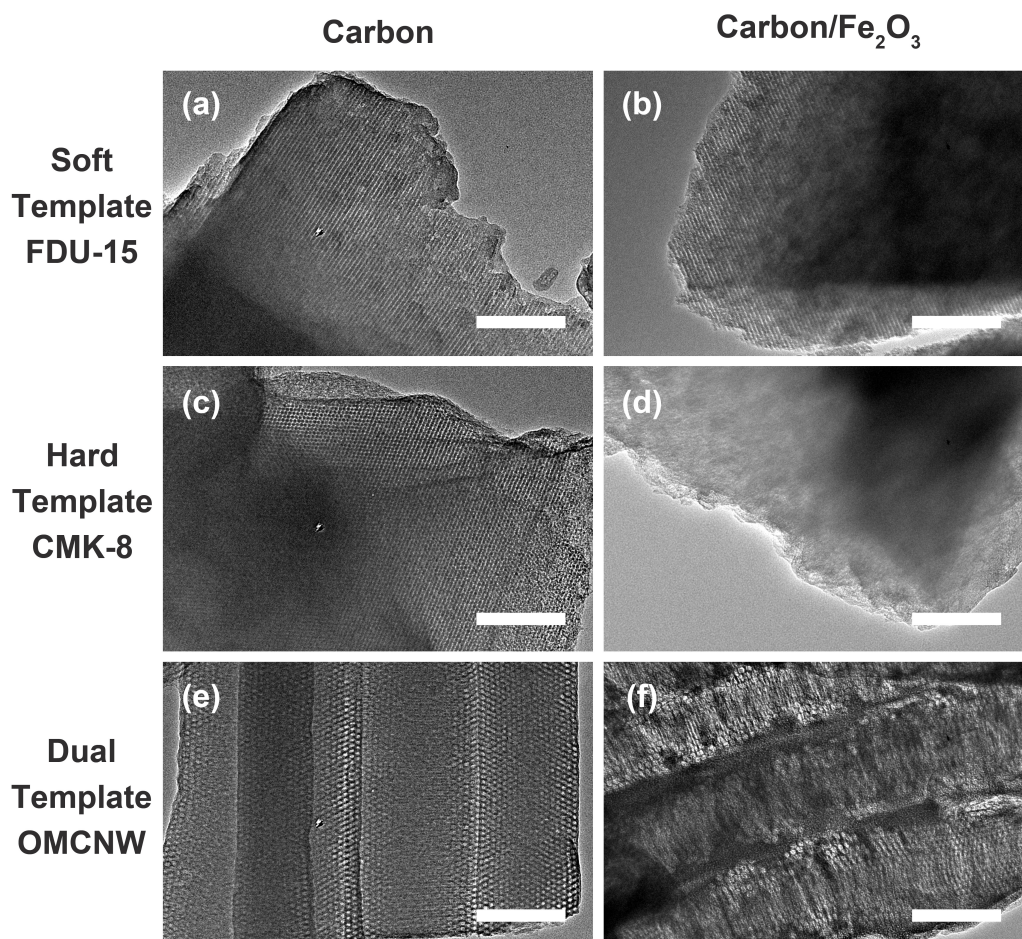


**Figure 3. 3 TEM images of different mesostructures OMCs & OMC/ $\text{Fe}_2\text{O}_3$  composites:**

(a) FDU-15, (b) FDU-15-20.0, (c) CMK-8, (d) CMK-8-47.1, (e) OMCNW, (f) OMCNW-54.2. All scale bars are 200 nm.

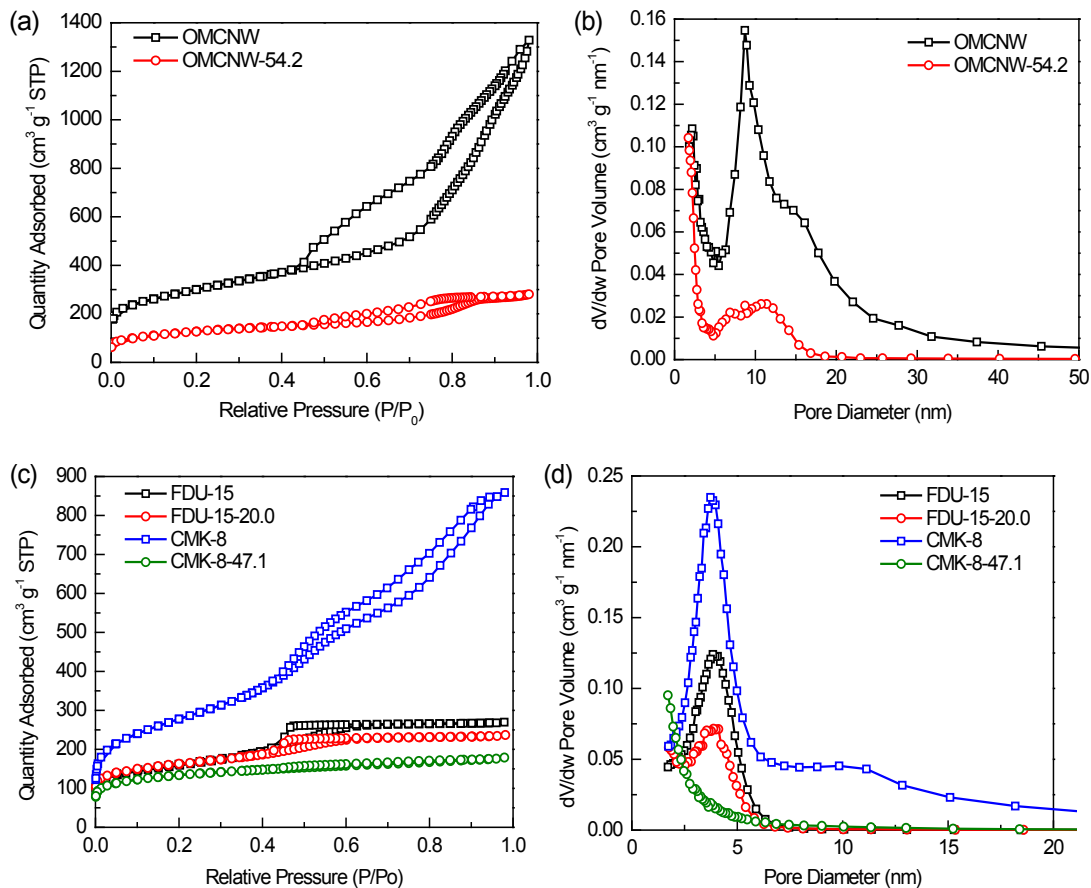


**Figure 3. 4 N<sub>2</sub> adsorption-desorption isotherms and pore size distributions of OMCNW, FDU-15, CMK-8 and their derived Fe<sub>2</sub>O<sub>3</sub> composites**

(a, c) N<sub>2</sub> adsorption-desorption isotherms, (b, d) pore size distributions.

The porous structures of OMCs and OMC/Fe<sub>2</sub>O<sub>3</sub> composites was further characterized by transmission electron microscopy (TEM) and N<sub>2</sub> adsorption-desorption isotherms. Soft templated FDU-15 (Figure 3.3a) and hard templated CMK-8 (Figure 3.3c) show typical 1D column and 3D bicontinuous structures with pore diameters of ~4 nm. In contrast, TEM image along the length of the OMCNW prepared using dual templates (Figure 3.3e) shows the combined effects of both templates. The parallel arrays of straight hexagonal mesopores derived from soft template are reshaped to the

circular hexagonal mesopores due to the curvature of the hard template AAO pores. In addition to the pore shape, the pore diameter is increased to  $\sim 9$  nm compared with single templated FDU-15 and CMK-8.

The  $N_2$  adsorption-desorption isotherm of OMCNW (Figure 3.4a, black) shows the mesoporous characteristics of a type-IV curve,<sup>125</sup> which is similar with FDU-15 and CMK-3 (Figure 3.4c). A broad pore size distribution with a clear peak at the diameter of 8.7 nm is obtained for OMCNW (Figure 3.4b, black), which is more than doubled of pore size in FDU-15 and CMK-3 (both are 3.8 nm, Figure 3.4d), and matches well with TEM observation. Table 3.1 lists the structure parameters of OMCNW, FDU-15 and CMK-8. The total surface area and pore volume of OMCNW are  $1063 \text{ cm}^2 \text{ g}^{-1}$  and  $1.950 \text{ cm}^3 \text{ g}^{-1}$ , which are 2 and 6 times greater than those of the soft template OMC (FDU-15), and are even larger than the hard templated CMK-8.

**Table 3. 1  $N_2$  adsorption-desorption properties of OMCs composites\***

Sample ID	Soft Template FDU-15	Hard Template CMK-8	Dual Template OMCNW
$d$ (nm)	3.8	3.8	8.7
$S_t$ ( $\text{m}^2 \text{ g}^{-1}$ )	554	992	1063
$V_t$ ( $\text{cm}^3 \text{ g}^{-1}$ )	0.327	1.178	1.950

\* All data are calculated from adsorption branches.

$d$ : pore diameter;

$S_t$  and  $V_t$ : total surface area and pore volume;

Since both dual template OMCNWs and soft template FDU-15 were synthesized using the same surfactant under the same conditions, we attribute the large difference in their surface area and pore volume to the AAO hard template. In order to observe the

differences in the pore structures as they evolve during the annealing process, N<sub>2</sub> adsorption-desorption and high-resolution TEM (HRTEM) of FDU-15 and OMCNW annealed at 350 °C and 900 °C were used to compare the size and wall thickness of their mesopores (Figure 3.5). For FDU-15, the HRTEMs (Figure 3.5 c, e) show the mesopore wall slightly shrank from ~7 nm at 350 °C to ~6 nm at 900 °C, which is due to the volume decrease of the resin polymer during the carbonization process.<sup>23</sup> Along with this slight change in wall thickness, a ~40 % decrease in the diameter of the mesopores is observed, decreasing from 6.1 nm at 350 °C (Figure 3.4d) to 3.8 nm at 900 °C (Figure 3.5 a). The shrinkage of both mesopore and pore wall lead to a decrease in the unit cell parameter from ~13 nm at 350 °C to ~10 nm at 900 °C, as previously reported.<sup>23</sup> OMCNW undergoes similar mesopore wall thinning (Figure 3.5 d, f), however, the OMCNW pore diameter increases from 7.7 nm at 350 °C (Figure 3.5 b) to 8.7 nm at 900 °C (Figure 3.3 b), which is different from the shrinkage of the pore size in FDU-15. This difference in behavior would suggest that there is a strong interaction between the resin polymer and AAO surface since they both have a large number of hydroxyl groups.<sup>157</sup> This interaction could help to maintain nanowires' diameter and unit cell parameter during the carbonization process.<sup>158</sup> Therefore, extra space is added to the mesopores in the OMCNW from the pore wall contraction. These AAO induced different structure evolutions are illustrated in Figure 3.6. Overall, the strong interactions between AAO pores and nanowires help to double the pore size and decrease the pore wall thickness, which leads to an enlarged surface area and larger

pore volume. The increase in surface area and pore volume can enhance carbon capacitance and  $\text{Fe}_2\text{O}_3$  loading, thus improve the electrochemical performance of OMCNW/ $\text{Fe}_2\text{O}_3$ .

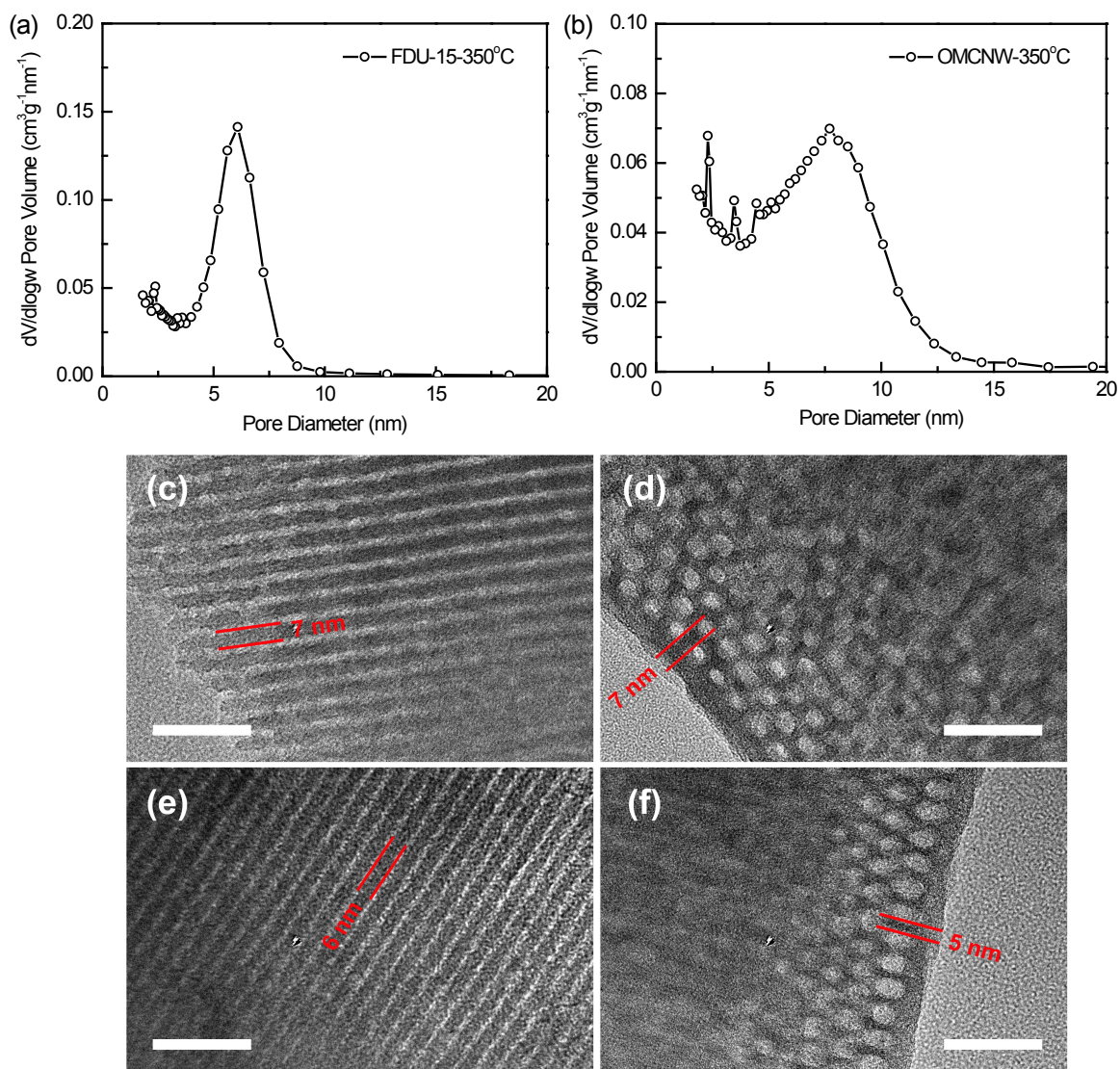


**Figure 3. 5 Pore sizes and pore wall thickness of FDU-15 and OMCNW annealed at different temperatures.**

(a, b) Pore size distribution of (a) FDU-15 annealed at 350 °C, (b) OMCNW annealed at 350 °C. (c-f) High-resolution TEM of (c) FDU-15 annealed at 350 °C, (d) OMCNW annealed at 350 °C, (e) FDU-15 annealed at 900 °C, (f) OMCNW annealed at 900 °C,

all scale bars in HRTEMs are 50 nm, the red labels indicate the mesopore wall thickness.

ICP-OES was used to monitor the loading amount of  $\text{Fe}_2\text{O}_3$  in 3 types of OMCs. OMCNW can accommodate more  $\text{Fe}(\text{NO}_3)_3$  precursor, hence the  $\text{Fe}_2\text{O}_3$  % of OMCNW/ $\text{Fe}_2\text{O}_3$  (54.2 %) is more than 2.5 times greater than the soft templated FDU-15/ $\text{Fe}_2\text{O}_3$  (20.0 %) and even slightly higher than the hard templated CMK-8/ $\text{Fe}_2\text{O}_3$  (47.1 %). The high mass loading is attributed to the optimized porous structure and pore volume enabled by dual template methodology.

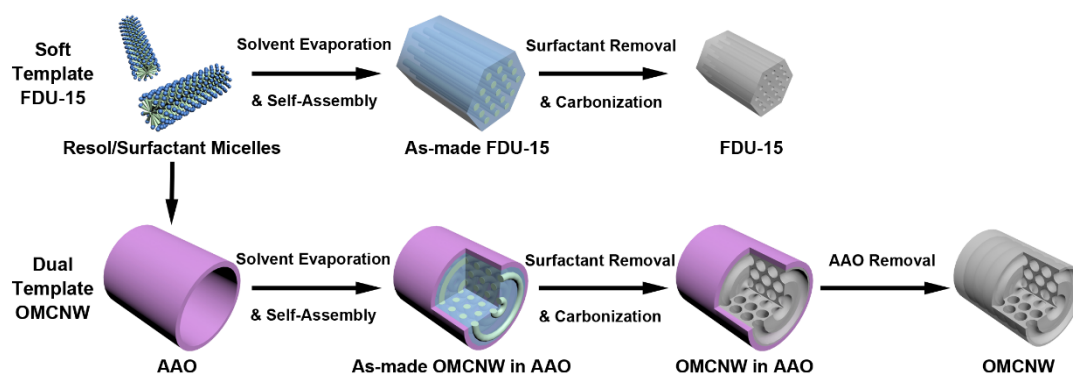


**Figure 3. 6 Schematic illustration of different mesostructure evolutions for mesoporous carbon synthesized with & without AAO.**

Although OMCNW/ $\text{Fe}_2\text{O}_3$  has even higher  $\text{Fe}_2\text{O}_3$  % loading than hard templated CMK-8/ $\text{Fe}_2\text{O}_3$ , it do not suffer mesostructure collapse upon  $\text{Fe}_2\text{O}_3$  loading. In Figure 3.4a, OMCNW-54.2 still shows a type-IV mesoporous characteristic adsorption-desorption curve, with a broad mesopore size distribution range (5 nm – 16 nm) which is similar to the OMCNW (Figure 3.4b), indicate a maintained mesostructure. Similarly, in Figure 3.4d, the pore size of FDU-15-20.0 is 3.8 nm, which is same as FDU-15. In contrast, the pore size decreased from 3.8 nm in CMK-8 to less than 1.7 nm in CMK-8-47.1, indicate a complete loss of mesoporosity.

**Table 3. 2 Mesopore volume change in OMCs & OMC/Fe<sub>2</sub>O<sub>3</sub> composites\***

Sample ID	FDU-15	FDU-15-20.0	CMK-8	CMK-8-47.1	OMCNW	OMCNW-54.2
$V_{meso}$ (cm <sup>3</sup> g <sup>-1</sup> )	0.311	0.199	1.158	0.123	1.715	0.322
$\Delta V_{meso}$ % (%)	-	20.7	-	80.5	-	59.0

\* All data are calculated from adsorption branches.

$V_{meso}$ : mesopore (2 nm <  $d$  < 50 nm) volume;

$\Delta V_{meso}$  %: normalized mesopore volume change after Fe<sub>2</sub>O<sub>3</sub> loading based on original carbon.

The mesostructure change upon Fe<sub>2</sub>O<sub>3</sub> loading is further evaluated by the mesopore volume difference between OMC/Fe<sub>2</sub>O<sub>3</sub> composites and their corresponding OMCs ( $\Delta V_{meso}$  %, see supporting information for detailed calculations). As shown in Table 3.2, the  $\Delta V_{meso}$  % of OMCNW-54.2 (59.0 %) is between soft templated FDU-15-20.0 (20.7 %) and hard templated CMK-8-47.1 (80.5 %). The smaller  $\Delta V_{meso}$  % means more mesopores were preserved, indicating a stable mesostructure upon Fe<sub>2</sub>O<sub>3</sub> loading. Considering that Fe<sub>2</sub>O<sub>3</sub> % loaded in OMCNW-54.2 is more than double the amount in FDU-15-20.0, the  $\Delta V_{meso}$  % in OMCNW-54.2 is proportional higher than in FDU-15-20.0. Therefore, we can clearly conclude that the structure stability of dual templated OMCNW is similar to soft templated FDU-15, and is much more stable than hard templated CMK-8. This is also supported by TEM images: Figure 3.3b and 2f show the well-preserved 1D column mesopores in FDU-15-20.0 and circular mesostructure in OMCNW-54.2, respectively, while in Figure 3.3d, the ordered 3D mesostructure has completely disappeared in CMK-8-47.1. The unstable mesopores of CMK-8 are due to the fragility of structure-supporting nano-bridges derived from the micropores (< 2 nm) in the original silica template.<sup>20</sup> In the Fe<sub>2</sub>O<sub>3</sub> growth process, the released gasses (H<sub>2</sub>O

and NO<sub>x</sub>) or volume changes during the Fe(NO<sub>3</sub>)<sub>3</sub> to Fe<sub>2</sub>O<sub>3</sub> transformation could easily break the nano-bridges and thus the mesoporous architecture.<sup>44</sup> In the case of OMCNW and FDU-15, both of which include surfactant as the mesostructure directing reagent, the rigid carbon networks are formed around the tubular surfactant micelles (Figure 3.6)<sup>110</sup>. Therefore, their structure is more tolerant toward solvent evaporation or salt decomposition in the Fe<sub>2</sub>O<sub>3</sub> growth process. It is worth noting that, owing to the extremely high mesopore volume of OMCNW, even after loading of Fe<sub>2</sub>O<sub>3</sub>, the OMCNW-54.2 still has 0.322 cm<sup>3</sup> g<sup>-1</sup> mesopore volume, which is higher than the other two OMC/Fe<sub>2</sub>O<sub>3</sub> composites derived from single templated carbons. The large reserve of mesopores is anticipated to act as fast ion pathways which will improve ion mobility and accessibility during electrochemical processes.

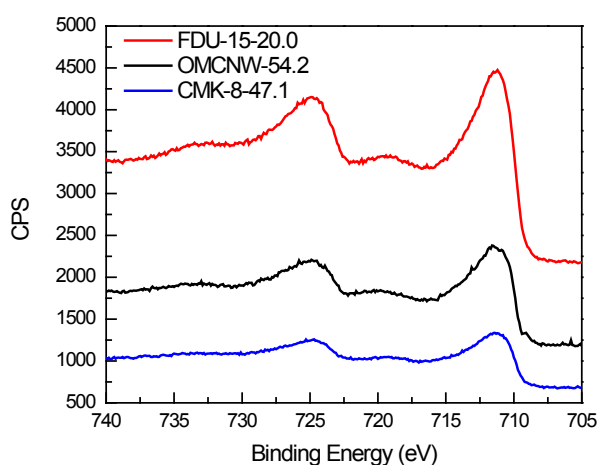


**Figure 3. 7 XPS spectrums of OMC/Fe<sub>2</sub>O<sub>3</sub> composites.**

The valence state of iron oxide in OMCNW/Fe<sub>2</sub>O<sub>3</sub> composite was determined by X-ray photoelectron spectroscopy (XPS) (Figure 3.7). Three broad peaks at 711 eV, 719 eV, and 724 eV are in agreement with the reported value for Fe<sub>2</sub>O<sub>3</sub>,<sup>124</sup> which is

same as single templated FDU-15-20.0 and CMK-8-47.1 derived by similar Fe<sub>2</sub>O<sub>3</sub> incorporation steps. The X-ray diffraction (XRD) of OMC/Fe<sub>2</sub>O<sub>3</sub> composites (data not shown) have no distinguished peak, indicating poor crystallinity of Fe<sub>2</sub>O<sub>3</sub> nanoparticles due to the low anneal temperature of 190 °C.

### **3.3.2 Electrochemical Studies on ion transportation and capacitance performances**

Cyclic voltammetry (CV) responses of the 3 types of OMCs at a scan rate of 5 mV s<sup>-1</sup> are presented in Figure 3.8a. All of the curves have a rectangular shape, which is characteristic of electrochemical double layer capacitance (EDLC). The specific capacitance of OMCNW, CMK-8, and FDU-15 are 145 F g<sup>-1</sup>, 113 F g<sup>-1</sup>, and 87 F g<sup>-1</sup>, respectively, which is a similar trend to the surface area values of the OMCs. The capacitances of different OMCs at various scan rates are presented in Figure 3.8c. The capacitance retention between 200 mV s<sup>-1</sup> and 5 mV s<sup>-1</sup> ( $C_{200\text{mV}}/C_{5\text{mV}}$ ) are similar for the OMCNW (62 %), FDU-15 (59 %), and CMK-8 (57 %), indicating a good electronic conductivity and ionic mobility in all of OMC samples.

The CV curves of OMC/Fe<sub>2</sub>O<sub>3</sub> composites are shown in Figure 3.8b. For all of OMC/Fe<sub>2</sub>O<sub>3</sub>, especially for OMCNW-54.2 and CMK-8-47.1 which have high Fe<sub>2</sub>O<sub>3</sub> content, the peaks at ~ -0.3 V and < -0.6 V are typical for redox reactions from sulfite anions adsorbed on Fe<sub>2</sub>O<sub>3</sub> and redox reactions between Fe(II) and Fe(III).<sup>120, 138-142</sup> The

larger areas of CV curves in OMC/Fe<sub>2</sub>O<sub>3</sub> composites indicate increased capacitance upon Fe<sub>2</sub>O<sub>3</sub> loading.

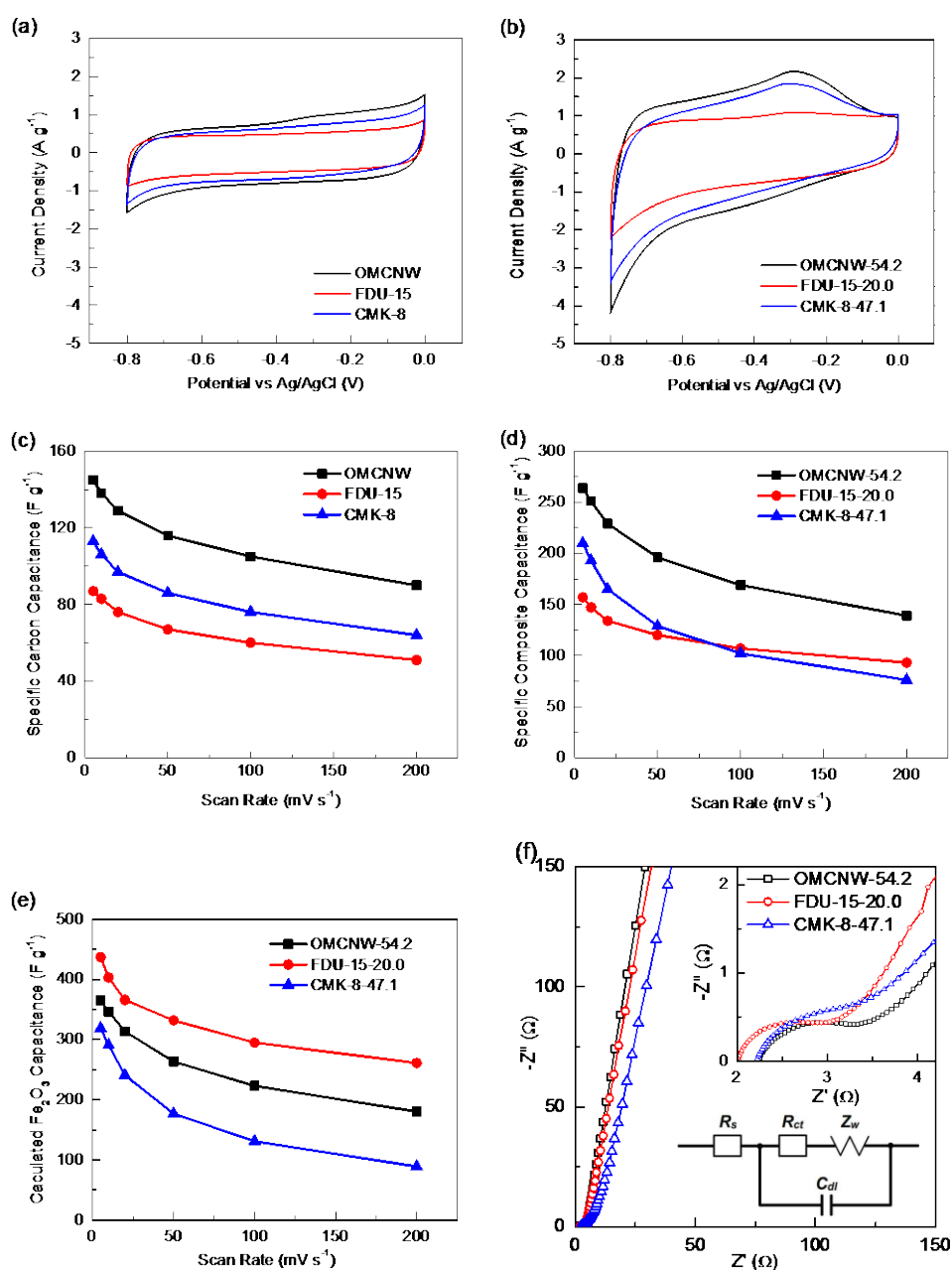


**Figure 3. 8 CV curves, rate performance, and Nyquist plots for different mesostructured OMCs and OMC/Fe<sub>2</sub>O<sub>3</sub> composites.**

(a) CV curves of OMCs (b) CV curves of OMC/Fe<sub>2</sub>O<sub>3</sub> composites in 1M Na<sub>2</sub>SO<sub>3</sub> at scan rate of 5mV s<sup>-1</sup>. (c & d) specific capacitances of OMCs (c) and OMC/Fe<sub>2</sub>O<sub>3</sub>

composites (d) at different scan rates. (e) Calculated  $\text{Fe}_2\text{O}_3$  capacitances in different OMC/ $\text{Fe}_2\text{O}_3$  composites at different scan rates. (f) Nyquist plots of OMC/ $\text{Fe}_2\text{O}_3$  composites, inset: equivalent Randles circuit.

The capacitance of the different mesostructured OMC/ $\text{Fe}_2\text{O}_3$  composites at scan rates between 5 mV and 200 mV are shown in Figure 3.8d. Regardless of scan rate, the OMCNW-54.2 exhibits the highest specific capacitance among all three OMC/ $\text{Fe}_2\text{O}_3$  composites. As the OMC/ $\text{Fe}_2\text{O}_3$  composites were made by OMCs and iron oxide, there are three factors which determine the value of composite capacitance ( $C_{total}$ ): the carbon capacitance ( $C_C$ ), the iron oxide capacitance ( $C_{\text{Fe}_2\text{O}_3}$ ), and the loading amount of  $\text{Fe}_2\text{O}_3$  ( $\text{Fe}_2\text{O}_3$  %). As shown in Figure 3.8c, the carbon capacitance of dual templated OMCNW is much higher than single templated FDU-15 and CMK-8, which provides a good starting point to achieve a high capacitance of the OMCNW/ $\text{Fe}_2\text{O}_3$ .

In order to compare the  $\text{Fe}_2\text{O}_3$  capacitance,  $C_{\text{Fe}_2\text{O}_3}$  was calculated using equation 2.5. The calculated  $\text{Fe}_2\text{O}_3$  capacitances are shown in Figure 3.8e. The hard template derived CMK-8-47.1, especially for high scan rates, demonstrated the lowest  $\text{Fe}_2\text{O}_3$  capacitance due to the limited ion transport in the collapsed mesopores. On the other hand, for soft template derived FDU-15-20.0, due to the small  $\text{Fe}_2\text{O}_3$  % and favorable ion transportation in the well preserved mesopores, the  $\text{Fe}_2\text{O}_3$  capacitance is higher than the other two OMC/ $\text{Fe}_2\text{O}_3$  for all scan rates. In the case of dual template derived OMCNW-54.2, the well preserved mesostructure and small nanowire diameter lead to a good ionic transportation, which results in higher  $C_{\text{Fe}_2\text{O}_3}$  than CMK-8-47.1. However,

due to the higher Fe<sub>2</sub>O<sub>3</sub> % and larger pore diameter in OMCNW-54.2, its Fe<sub>2</sub>O<sub>3</sub> nanoparticle size is larger than in FDU-15-20.0, which decrease the utilization of Fe<sub>2</sub>O<sub>3</sub> and results to a smaller  $C_{Fe_2O_3}$  in OMCNW-54.2 than in FDU-15-20.0.

**Table 3. 3 Comparison of the electrochemical performance of iron oxide related nanomaterials**

Materials	Specific Capacitance	Potential Window*	Electrolyte <sup>#</sup>	Ref.
Fe <sub>3</sub> O <sub>4</sub> nanoparticles	58 F g <sup>-1</sup> at 10 mV s <sup>-1</sup>	-0.6 ~ 0.2 V vs. Hg/HgO	6 M KOH	129
Fe <sub>2</sub> O <sub>3</sub> /CMK-3	113 F g <sup>-1</sup> at 2 mV s <sup>-1</sup>	-0.9 ~ 0.9 V, 2 Electrodes	6 M KOH	59
Fe <sub>3</sub> O <sub>4</sub> /MWCNTs	129.3 F g <sup>-1</sup> at 2.5 mA cm <sup>-2</sup>	-1 ~ 0 V vs. SCE	6 M KOH	143
Fe <sub>3</sub> O <sub>4</sub> /C/Si	154.8 F g <sup>-1</sup> at 0.2 A g <sup>-1</sup>	-1 ~ 0.5 V vs. Ag/AgCl	1 M NaOH	159
Fe <sub>3</sub> O <sub>4</sub> sheets/graphene	326 F g <sup>-1</sup> at 0.5 A g <sup>-1</sup>	-1.15 ~ 0.2 V vs. SCE	0.5 M LiOH	160
Fe <sub>2</sub> O <sub>3</sub> nanotubes/carbon fibers	257.8 F g <sup>-1</sup> at 1.3 A g <sup>-1</sup>	-0.8 ~ 0 V vs. Ag/AgCl	5 M LiCl	149
FeO <sub>x</sub> /carbon nanofoam	84 F g <sup>-1</sup> at 5 mV s <sup>-1</sup>	-0.8 ~ 0.2 V vs. Ag/AgCl	2.5 M Li <sub>2</sub> SO <sub>4</sub>	148
Fe <sub>2</sub> O <sub>3</sub> /C <sub>3</sub> N <sub>4</sub> hollow microspheres	260 F g <sup>-1</sup> at 0.5 A g <sup>-1</sup>	-1 ~ 0 V vs. SCE	2.5 M Li <sub>2</sub> SO <sub>4</sub>	161
Fe <sub>2</sub> O <sub>3</sub> nanosheets	116.25 F g <sup>-1</sup> at 0.75 A g <sup>-1</sup>	-0.6 ~ 0 V vs. SCE	1 M Li <sub>2</sub> SO <sub>4</sub>	162
Fe <sub>2</sub> O <sub>3</sub> nanorods & nanosheets	146 F g <sup>-1</sup> at 5 mV s <sup>-1</sup>	-0.8 ~ 0 V vs. SCE	1 M Li <sub>2</sub> SO <sub>4</sub>	163
Fe <sub>2</sub> O <sub>3</sub> nanotubes/rGO	215 F g <sup>-1</sup> at 2.5 mV s <sup>-1</sup>	-1 V ~ 0 V vs. Ag/AgCl	1 M Na <sub>2</sub> SO <sub>4</sub>	164
Fe <sub>2</sub> O <sub>3</sub> /PPy nanowires	190 F g <sup>-1</sup> at 0.2 A g <sup>-1</sup>	-1.2 ~ 0 V vs. SCE	0.1 M Na <sub>2</sub> SO <sub>3</sub>	165
Fe <sub>3</sub> O <sub>4</sub> thin film	174 F g <sup>-1</sup> at 2 mV s <sup>-1</sup>	-0.8 ~ -0.1 V vs. Ag/AgCl	1 M Na <sub>2</sub> SO <sub>3</sub>	142
Fe <sub>3</sub> O <sub>4</sub> nanoparticles	207.7 F g <sup>-1</sup> at 0.4 A g <sup>-1</sup>	-0.9 ~ 0.1 V vs. SCE	1 M Na <sub>2</sub> SO <sub>3</sub>	166
Fe <sub>3</sub> O <sub>4</sub> /carbon nanofibers	135 F g <sup>-1</sup> at 420 mA g <sup>-1</sup>	-0.9 ~ 0.1 V vs. SCE	1 M Na <sub>2</sub> SO <sub>3</sub>	120

**Table 3. 3** (*Continued*)

Materials	Specific Capacitance	Potential Window*	Electrolyte <sup>#</sup>	Ref.
Fe <sub>3</sub> O <sub>4</sub> /carbon nanosheets	163.4 F g <sup>-1</sup> at 1 A g <sup>-1</sup>	-0.8 ~ -0.2 V vs. Ag/AgCl	1 M Na <sub>2</sub> SO <sub>3</sub>	132
Fe <sub>2</sub> O <sub>3</sub> /graphene	76 F g <sup>-1</sup> at 25 mV s <sup>-1</sup>	-0.8 ~ 0 V vs. Ag/AgCl	1 M Na <sub>2</sub> SO <sub>3</sub>	150
Fe <sub>2</sub> O <sub>3</sub> /mesoporous carbon	235 F g <sup>-1</sup> at 0.5 A g <sup>-1</sup>	-1 ~ -0.2 V vs. Ag/AgCl	1 M Na <sub>2</sub> SO <sub>3</sub>	97
Fe <sub>2</sub> O <sub>3</sub> ordered mesoporous	173 F g <sup>-1</sup> at 5 mV s <sup>-1</sup>	-0.8 ~ 0 V vs. Ag/AgCl	1 M Na <sub>2</sub> SO <sub>3</sub>	Chap. 2
Fe <sub>2</sub> O <sub>3</sub> /FDU-15	157 F g <sup>-1</sup> at 5 mV s <sup>-1</sup>	-0.8 ~ 0 V vs. Ag/AgCl	1 M Na <sub>2</sub> SO <sub>3</sub>	Chap. 2
Fe <sub>2</sub> O <sub>3</sub> /CMK-3	195 F g <sup>-1</sup> at 5 mV s <sup>-1</sup>	-0.8 ~ 0 V vs. Ag/AgCl	1 M Na <sub>2</sub> SO <sub>3</sub>	Chap. 2
Fe <sub>2</sub> O <sub>3</sub> /CMK-8	210 F g <sup>-1</sup> at 5 mV s <sup>-1</sup>	-0.8 ~ 0 V vs. Ag/AgCl	1 M Na <sub>2</sub> SO <sub>3</sub>	Chap. 2
Fe <sub>2</sub> O <sub>3</sub> /OMCNW	264 F g <sup>-1</sup> at 5 mV s <sup>-1</sup>	-0.8 ~ 0 V vs. Ag/AgCl	1 M Na <sub>2</sub> SO <sub>3</sub>	This work

\* All materials were tested in the 3 electrode system unless specified.

<sup>#</sup> All were in the aqueous electrolyte.

Overall, the balanced structural properties in the dual templated OMCNW-54.2 ensure the highest carbon capacitance & Fe<sub>2</sub>O<sub>3</sub> loading amount and a moderate iron oxide capacitance, which lead to 264 F g<sup>-1</sup> total capacitance of OMCNW-54.2 at 5 mV s<sup>-1</sup>. This capacitance value is not only higher than the FDU-15-20 (157 F g<sup>-1</sup>) and CMK-3-47.2 (210 F g<sup>-1</sup>), but also higher than most previously reported iron oxide related nanomaterials tested in aqueous electrolytes (Table 3.3). In addition, due to the good electronic conductivity along the nanowires and favorable ionic mobility through the well preserved mesopores in the ~ 100 nm nanowire radius, the OMCNW-54.2 exhibits an excellent rate performance, with specific capacitance of 139 F g<sup>-1</sup> at 200 mV s<sup>-1</sup>.

**Table 3. 4 EIS parameters for different OMC/Fe<sub>2</sub>O<sub>3</sub> composites**

Sample ID	Soft Template FDU-15-20.0	Hard Template CMK-8-47.1	Dual Template OMCNW-54.2
$R_s$ ( $\Omega$ )	2.0	2.2	2.2
$R_{ct}$ ( $\Omega$ )	1.1	1.3	1.3
$Z_w$ ( $\Omega$ )	2.1	6.8	0.8

The good ion mobility in OMCNW-54.2 can be observed by electrochemical impedance spectroscopy (EIS). As shown in Figure 3.8f, all Nyquist plots of OMC/Fe<sub>2</sub>O<sub>3</sub> composites are similar in shape with an arc at high frequencies, followed by a straight line inclined around 45° to the real axis in the medium frequencies, and a nearly vertical line in the low frequency region. Such Nyquist plot pattern is typical for an equivalent Randles circuit (inset of Figure 3.8 f).<sup>119, 121, 126, 127, 129</sup>

Table 3.4 lists the values of each circuit component for the different composites. For all samples, the solution resistance ( $R_s$ ) is similar (2.0 - 2.2  $\Omega$ ). Due to the larger Fe<sub>2</sub>O<sub>3</sub> particle size in OMCNW-54.2 and CMK-8-47.1, the charge transfer resistance ( $R_{ct}$ ) of them (1.3  $\Omega$ ) are slightly larger than in FDU-15-20.0 (1.1  $\Omega$ ). The biggest difference between samples is the Warburg impedance ( $Z_w$ ), which is ascribed to the straight line with 45° angle in the medium frequency region and can directly reflect ion transport process in the porous electrode. As listed in Table 3.4,  $Z_w$  of OMCNW-54.2, FDU-15-20.0 and CMK-8-47.1 are 0.8  $\Omega$ , 2.1  $\Omega$ , and 6.8  $\Omega$ , respectively. The small  $Z_w$  of OMCNW-54.2 proves our previous assumption that the nanowire morphology along with well-preserved mesopores could enhance ion mobility from the nanowire radius.

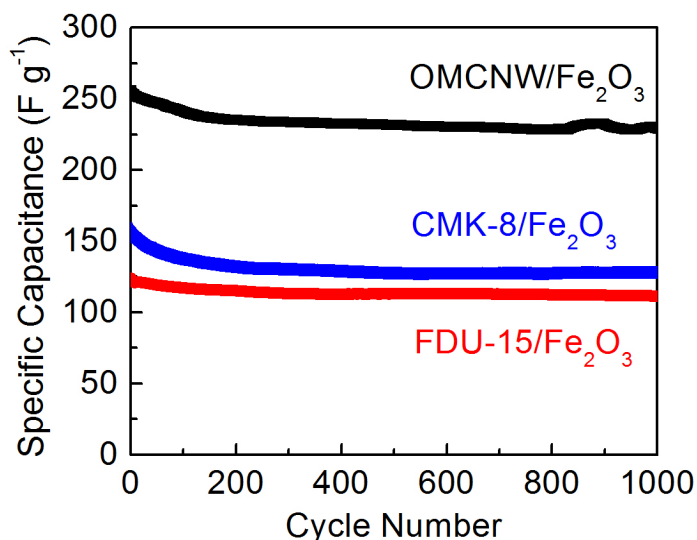


**Figure 3. 9 Cycling performance of different OMC/Fe<sub>2</sub>O<sub>3</sub> composites.**

Finally, we evaluated the capacitance retention upon long term cycling of OMC/Fe<sub>2</sub>O<sub>3</sub> composites by galvanostatic charge-discharge test at a current density of 5 A g<sup>-1</sup>. The specific capacitances as a function of cycle number are summarized and compared in Figure 3.9. After 1000 cycles, the OMCNW-54.2 still has a capacitance of 229 F g<sup>-1</sup>, which shows good capacitance retention of 89.5 %. This capacitance retention is similar to FDU-15-20.0 (89.8 %), and attributed to the good structure stability. In contrast, lower capacitance retention (80.4 %) was found in CMK-8-47.2, indicating a less stable capacitance in the fragile hard template derived carbon framework.

The comparison of the structural properties and electrochemical performance between the three types of OMCs used herein are presented in Table 3.5. Clearly, the dual templated OMCNW presents the structural advantages of both soft and hard templated OMCs and avoids their drawbacks, which leads to the best electrochemical performance of OMCNW/Fe<sub>2</sub>O<sub>3</sub>.

**Table 3. 5 Structural properties and electrochemical performance comparison of OMCs from different synthetic strategies as host materials of Fe<sub>2</sub>O<sub>3</sub>**

Preparation Method		Soft Template (FDU-15)	Hard Template (CMK-8)	Dual Template (OMCNW)
Structural Properties	Surface area (m <sup>2</sup> g <sup>-1</sup> )	Small (554)	Large (992)	Large (1063)
	Pore volume (m <sup>3</sup> g <sup>-1</sup> )	Small (0.327)	Large (1.178)	Large (1.950)
	Pore size (nm)	Small (3.8)	Small (3.8)	Large (8.7)
	Structural stability (from TEM)	Stable	Unstable	Stable
	Morphology	Micron sized particles	Micron sized particles	Nanowires
Electrochemical Performances	Carbon capacitance (F g <sup>-1</sup> at 5 mV s <sup>-1</sup> )	Small (87)	Medium (113)	Large (145)
	Fe <sub>2</sub> O <sub>3</sub> capacitance (F g <sup>-1</sup> at 5 mV s <sup>-1</sup> )	Large (437)	Small (319)	Medium (365)
	Fe <sub>2</sub> O <sub>3</sub> loading amount (%)	Low (20.0)	High (47.1)	High (54.2)
	OMC/Fe <sub>2</sub> O <sub>3</sub> Capacitance (F g <sup>-1</sup> at 5 mV s <sup>-1</sup> )	Small (157)	Medium (210)	Large (264)
	Ion accessibility (evaluated by Z <sub>w</sub> , Ω)	Easy (2.1)	Hard (6.8)	Easy (0.8)
	High rate capacitance retention (C <sub>200mV</sub> /C <sub>5mV</sub> , %)	Large (59)	Small (36)	Large (53)
	Cycling stability (% after 1000 cycles)	Stable (89.8)	Moderate (80.4)	Stable (89.5)

### 3.4 Conclusions

A dual template strategy was used to synthesize ordered mesoporous carbon nanowires by conjugating soft template and hard template methodologies and was applied, for the first time, as an oxide host material to form OMCNW/Fe<sub>2</sub>O<sub>3</sub> composites. The structural properties and electrochemical performance of dual templated OMCNW/Fe<sub>2</sub>O<sub>3</sub> were compared with soft templated and hard templated

OMCs/Fe<sub>2</sub>O<sub>3</sub> composites. The OMCNW from the dual template strategy has double the total surface area, and six times the total pore volume when compared to the soft templated FDU-15. When compared with hard template synthesized CMK-8, the OMCNW still present good mesostructure stability and ion mobility. In addition, the morphology of the hard template was well maintained as the 1D synthesized nanowires were a few microns in length and ~100 nm in radius. All of these structural properties made the OMCNW an ideal scaffold for heterogeneous hosting materials for high performance supercapacitors. The large surface area leads to a high carbon capacitance contribution, while the large pore volume and the stable carbon scaffold provide high Fe<sub>2</sub>O<sub>3</sub> loading of over 50% without the mesostructure degradation. Additionally, the nanowires with micro sized length could form a network to improve electronic conductivity, while the small radius of nanowires together with larger mesopore volume help to enhance the ionic mobility and accessibility, and ensure a high Fe<sub>2</sub>O<sub>3</sub> capacitance. Overall, the OMCNW/Fe<sub>2</sub>O<sub>3</sub> composite was able to deliver the highest specific capacitance of 264 F g<sup>-1</sup> at 5 mV s<sup>-1</sup>, with good rate capability and cycling performance. The synergistic effects of dual template method demonstrated in this work have significant impact on informed design of electrode materials on both mesoscale porous structure and macroscale morphology and could be applied for other electrochemical energy storage systems to improve both energy density and power density.

## **Chapter 4**

### **Dual-Template Ordered Mesoporous Carbon/Fe<sub>2</sub>O<sub>3</sub> Nanowires as Lithium-Ion Batteries Anodes**

## 4.1 Introduction

With the huge demand for portable electronic devices and electric vehicles, the development of rechargeable lithium-ion batteries (LIBs) has gained a worldwide interest in the past decades due to their high energy density, long cycle life, low self-discharge and environmental friendliness.<sup>167</sup> Currently, the commercial graphite anode is limited by its low lithium ion storage capacity ( $372 \text{ mAh g}^{-1}$ ).<sup>10</sup> To improve the energy density of batteries, various metal oxides (MO), such as  $\text{Fe}_2\text{O}_3$ ,  $\text{Fe}_3\text{O}_4$ ,  $\text{MnO}_2$ ,  $\text{Co}_3\text{O}_4$ ,  $\text{SnO}_2$ , and  $\text{NiO}$ , have been investigated to replace graphite as anode materials for their high theoretical capacities.<sup>168, 169</sup> Unfortunately, many metal oxides suffer from low rate performance due to poor electrical conductivity and hindered lithium diffusion pathways. In addition, the structural collapse and particle pulverization arising from drastic volume expansion during  $\text{Li}^+$  insertion/extraction can also result in the loss of electrical connectivity and unstable solid electrolyte interphase (SEI), eventually leading to poor cyclability.<sup>169, 170</sup>

To overcome these drawbacks, one effective approach is to reduce the metal oxide to the nanoscale, which can shorten lithium diffusion pathways and reduce the surface tension from volume expansion.<sup>171</sup> Another effective approach is to combine a metal oxide with a carbonaceous materials to increase the electrical conductivity and eliminate the structural change during cycling.<sup>168</sup> Among these carbonaceous materials, ordered mesoporous carbons (OMCs) have drawn much attention not only due to their good electrical conductivity, high corrosion resistance, high surface area and large pore

volume, but also due to the control of metal oxide nanoparticle size grown inside the well-defined mesopores.<sup>12</sup> In addition, the structure of uniformly distributed metal oxide nanoparticles separated by a carbon framework can help to prevent particle aggregation that often happens in nano-materials during cycling.<sup>13</sup> Therefore, OMC/MO composites exhibit improved electrochemical performance when compared to conventional materials.<sup>104</sup>

Since the capacity of most MO is much higher than the carbon materials, the content of MO should be as high as possible to achieve the maximum capacity performance. However, too much MO loading can lead to depressed electrochemical performances, as has been tested in many systems.<sup>28, 75, 82, 87</sup> Generally, the best cycling and rate performances have been achieved in composites with between 20 % - 35 % MO weight percentage. Exceeding this range results in a capacity drop or decrease of cycling/rate performance. This capacity fading can be attributed to the structural failure during MO loading process and/or electrochemical cycling, as has been proved in OMC/Fe<sub>2</sub>O<sub>3</sub> supercapacitors' systems.<sup>44</sup> Therefore, an OMC with stable structure is required to get a higher MO loading.

The mesostructure stability of OMC strongly depends on their synthesis process.<sup>44</sup> As we discovered in Chapter 2, the hard template OMCs have a large pore volume, which is favorable for a high MO loading content. However, most of the structures in those OMCs are connected by nanobridges that are derived from micropores in the original template. These nanobridges are fragile and easily collapse during loading of

MO and/or due to volume expansion during the charging/discharging process. As a result, many hard templated OMC/MO anodes suffer 30 % - 50 % capacity loss within 100 cycles.<sup>25, 26, 28, 31, 46, 75, 172</sup> In contrast, the soft templated OMCs have arch-like carbon frameworks, which are more stable upon guest nanoparticle loading and electrochemical cycling (Figure 1). However, their relatively small pore volume limits the metal oxide loading amount.<sup>48, 53, 57</sup> Clearly, the hard or soft template strategies have their intrinsic drawbacks and merits, which is also expected to influence their electrochemical performance as LIBs. Similar to supercapacitors, a balanced mesopore volume and structural stability needs to be addressed based on a comprehensive understanding of the relationship between structure properties and electrochemical performances for LIBs. However, there is a lack of detailed studies focusing on structure-induced LIBs' capacity performance differences for OMC/MO composites synthesized from different strategies.

Besides mesostructure, the material morphology also strongly affects the electrochemical performance of LIBs by influencing ion and electron conductivities. Compared with bulk materials and nanoparticles, one dimensional (1D) nanostructures can facilitate ionic transportation through the nano-scale radius while maintaining efficient charge transport through their micro-scale axis,<sup>5, 109, 156, 168</sup> especially when coupled with carbon materials to form heterogeneous 1D nanowire composites<sup>173-175</sup>. Clearly, the combination of ordered mesopores and 1D morphology would greatly favor the ion accessibility and enhance the electrochemical performance of carbon/MO

composites. Unfortunately, neither ordered mesoporous carbon nanowires (OMCNW) nor their derived metal oxide composite has been applied for LIBs.

Although both LIBs and pseudocapacitors store energy by faradic reactions, there are many differences between these two devices. For example, the properties of organic electrolyte used in LIBs is different with aqueous electrolytes used in pseudocapacitors. Since the affinity between the hydrophobic carbon surface and organic electrolytes is acceptable, strong acid treatment for the carbon surface modification is not necessary. Indeed, the surface functional group often increases side reactions and lead to a larger irreversible capacity, which is not good for LIBs. In addition, lithium insertion/desertion is much easier in crystal forms. On the contrary, the capacitance is normally higher in amorphous phase materials due to their larger surface area. Therefore, the annealing temperature is usually higher for LIBs in order to achieve a better crystallization. Moreover, the redox reaction is more thorough in LIBs due to the slow charge-discharge rate and large voltage-window. However, the deep charge-discharge process in LIBs often result in the huge volume change, which can seriously damage the material structure and cause the capacity failure. Hence, improving cyclability for LIBs is often more challenging than supercapacitors. The above factors imply that the conclusions drawn from supercapacitors' systems need to be carefully evaluated before applied to the LIBs.

In this Chapter, using OMC/Fe<sub>2</sub>O<sub>3</sub> composites as a model system, we conduct systematic studies on the effects of synthetic strategies on the structural properties and

electrochemical performances of LIB anodes.  $\text{Fe}_2\text{O}_3$  is chosen again because it can also be applied as anode materials for LIBs with a high theoretical capacity of  $1007 \text{ mAh g}^{-1}$ .<sup>109</sup> FDU-15, CMK-8, and OMCNW were used again to compare the difference between soft template, hard template, and dual template methods. The structural and electrochemical properties of those OMC/ $\text{Fe}_2\text{O}_3$  composites were systematically evaluated, aiming to understand the effects of mesostructure and morphology on the capacity performance and cycling stability. In this chapter, we show that the electrochemical performances of LIBs are more deeply related to the structure degradation and the ion accessibility.

## **4.2 Experiment Sections**

### **4.2.1 Materials Preparation**

1D cylindrically structured FDU-15 was synthesized by a soft template method according to Ref. <sup>110</sup>, using triblock copolymer Pluronic F127 ( $\text{EO}_{106}\text{PO}_{70}\text{EO}_{106}$ , MW=12600) as structure directing reagent and urea and formaldehyde as the carbon source. In a typical process, 1 g F127 was dissolved in 8.0 g ethanol. Then 5 g of 20 % resol precursors, prepared by literature method <sup>110</sup>, were added into the solution. The mixture was stirred for 1 h and then transferred to a glass Petri dish, and left for 5–8 h at room temperature and 24 h at  $100^\circ\text{C}$  to evaporate ethanol. Then the gel was thermopolymerized at  $180^\circ\text{C}$  for 12 h. The as-made product was collected and ground into fine powder. Calcination was carried out in a tubular furnace at  $600^\circ\text{C}$  for 3 h and

subsequently 900 °C for 2 h under Ar flow. The heating rates were 1 °C /min below 600 °C and 5 °C /min above 600 °C.

CMK-8 was synthesized by a hard template method, with mesoporous silica KIT-6 as a template. The KIT-6 was synthesized according to Ref. <sup>123</sup>, with the molar ratio of 0.017 P123 / 1.67 TEOS / 1.67 *n*-butanol / 1.83 HCl / 195 H<sub>2</sub>O. After surfactant removal, 1.2 g of KIT-6 was infiltrated by 1.17 g sucrose, 0.13 g of H<sub>2</sub>SO<sub>4</sub>, and 4.7 g H<sub>2</sub>O, then dried in an oven at 100 °C for 6 h, followed by 160 °C for another 6 h, the sample was treated again by a mixture of 0.62 g of sucrose, 0.07 g of H<sub>2</sub>SO<sub>4</sub> and 3.85 g of H<sub>2</sub>O, followed by the same drying process at 100 °C and 160 °C. The carbonization was carried out in a tubular furnace at 600 °C for 3 h, and subsequently 900 °C for 4 h under Ar flow, the heating rates were 1 °C /min below 600 °C and 5 °C /min above 600 °C. The silica was etched away by a 3 M NaOH solution three times at 50 °C. The template-free carbon product thus obtained was centrifuged and washed by D. I. water.

Dual template ordered mesoporous nanowires (OMCNW) were prepared similarly as soft template FDU-15 <sup>110</sup>, except that AAO membrane were used as the hard template. In general, 1 g F127, 8.0 g ethanol, and 5 g of 20 % resol was mixed and stirred for 1 h and then transferred to a glass Petri dish with an ethanol pre-wetted AAO, and left for 5–8 h at room temperature and 24 h at 100 °C. Then the gel was thermopolymerized in at 180 °C for 12 h, and the top resin outside of AAO was removed by stainless steel blade. The remaining AAO with resin inside were scratched out and annealed in the same process as FDU-15. The AAO membrane was dissolved by 3 M NaOH at 140 °C

for 8 h in a Teflon lined autoclave. The residual product was washed by distilled water several times until the pH is neutral.

In order to grow Fe<sub>2</sub>O<sub>3</sub> nanoparticles inside mesopores, the OMCs were soaked in a 45 wt % Fe(NO<sub>3</sub>)<sub>3</sub> aqueous solution and a low pressure vacuum filtration process was used to remove any extra salt solution outside the mesopores. The OMCs with Fe(NO<sub>3</sub>)<sub>3</sub> solution were heated to 100 °C for 6 h to evaporate water, followed by 400 °C annealing in argon flow for 5 h to decompose Fe(NO<sub>3</sub>)<sub>3</sub> into Fe<sub>2</sub>O<sub>3</sub>.

#### **4.2.2. Characterization**

X-ray diffraction (XRD) patterns were recorded by Bruker Smart1000 (Bruker AXS Inc., USA) using CuK $\alpha$  radiation. X-ray photoelectron spectroscopy (XPS) analysis was done on a Kratos AXIS 165 spectrometer. The C 1s peak was calibrated at 284.8 eV. Images of mesoporous carbon and carbon/Fe<sub>2</sub>O<sub>3</sub> composites were acquired using a scanning electron microscopy (Hitachi SU-70 SEM, operated at an acceleration voltage of 5 keV) and a transmission electron microscopy (JEOL JEM 2100 FE-TEM, 200 keV). Raman scattering spectra were collected at Horiba Yvon LabRam ARAMIS Raman Spectroscope using a helium neon laser excitation (632.8 nm).

Nitrogen (N<sub>2</sub>) adsorption and desorption isotherms were recorded with a Micromeritics ASAP 2020 Porosimeter Test Station. Samples were degassed (in a vacuum) at 200 °C for 12 hours before the test. The specific surface areas were calculated using the BET method from the nitrogen adsorption data in the relative

pressure range ( $P/P_0$ ) of 0.05–0.20. The porosity distribution was calculated from adsorption branch using the BJH (Barrett–Joyner–Halenda) equation.

The loading amount of  $\text{Fe}_2\text{O}_3$  was determined by inductively coupled plasma-atomic emission spectroscopy (ICP-AES) characterization performed on a Perkin Elmer ICP Optima 4700. Intensities were measured at 259.939 nm for Fe. Mesoporous carbon/ $\text{Fe}_2\text{O}_3$  samples were dissolved in a freshly prepared concentrated HCl/ethanol solution and diluted to a known volume before being administered to the plasma. The final concentration of HCl and ethanol were 2 % and 0.8 %, respectively.

#### **4.2.3 Electrochemical Measurements**

All the electrochemical studies were performed in coin-cell batteries which were assembled with Li metal foil as the counter and reference electrodes, Celgard®3501 (Celgard, LLC Corp., USA) as separator, and 1 M  $\text{LiPF}_6$  in a mixture of ethylene carbonate/dimethyl carbonate (EC/DMC, 1:1 by volume) as electrolyte. To make the working electrode, a slurry of the mesoporous material, carbon black, and a poly(vinylidene fluoride) (PVDF) binder at a weight ratio of 80:10:10 dispersed in N-Methyl-2-pyrrolidone (NMP) was cast onto a copper foil with a loading of 0.4 – 0.8 mg  $\text{cm}^{-2}$ . All the samples were dried in 100 °C vacuum oven overnight before assembly into coin-cells in an argon-filled glove box (MBraun, 0.5 ppm  $\text{H}_2\text{O}$ , 0.5 ppm  $\text{O}_2$ ). Galvanostatic lithiation/delithiation was carried out on an Arbin BT-2000 test station (Arbin Instruments, USA) in a potential range of 0.01 - 3 V (versus  $\text{Li/Li}^+$ ) at different

current densities. Cyclic voltammetry (CV) and electrochemical impedance spectroscopy (EIS) were carried out on a bipotentiostat (BI-STAT, Princeton Applied Research). The scan rate of CV is 0.1 mV s<sup>-1</sup>. The EIS data were analyzed by Z-fit software in EC-Lab V10.30.

## **4.3 Results and Discussions**

### **4.3.1 Morphological and Structural Characterization**

Raman spectroscopy was carried out to characterize the carbon structure. In Figure 4.1 a, all OMCs show two distinct bands: the G-band at ~ 1580 cm<sup>-1</sup> which corresponds to the graphite structure,<sup>176</sup> while the D-band at ~ 1330 cm<sup>-1</sup> represents the defect sites in carbon structures.<sup>177</sup> Although the soft and hard templated OMCs were derived from different carbon sources, the shape and intensity of D and G bands are almost same in different samples, indicating similar carbon structures in various OMCs. The integrated intensity ratios between D-band and G-band ( $I_D/I_G$ ) are 2.06 for all samples, which indicates a large number of defects in the carbon frameworks. In addition, the X-ray photoelectron spectroscopy (XPS) was carried out to observe the number of surface heteroatoms in different OMCs (Data not shown). The C/O ratio of FDU-15, CMK-8, and OMCNW is 10.3, 9.2, and 8.9, respectively, indicating similar amount of surface oxygen groups. Defects in the carbon lattice and carbon surface functional groups can affect the structural stability and electrochemical performance of carbon composites.<sup>178</sup> The same defect and functional group density in the synthesized OMC/Fe<sub>2</sub>O<sub>3</sub>

composites excludes the possibility that the distinct electrochemical performances come from these defect sites.

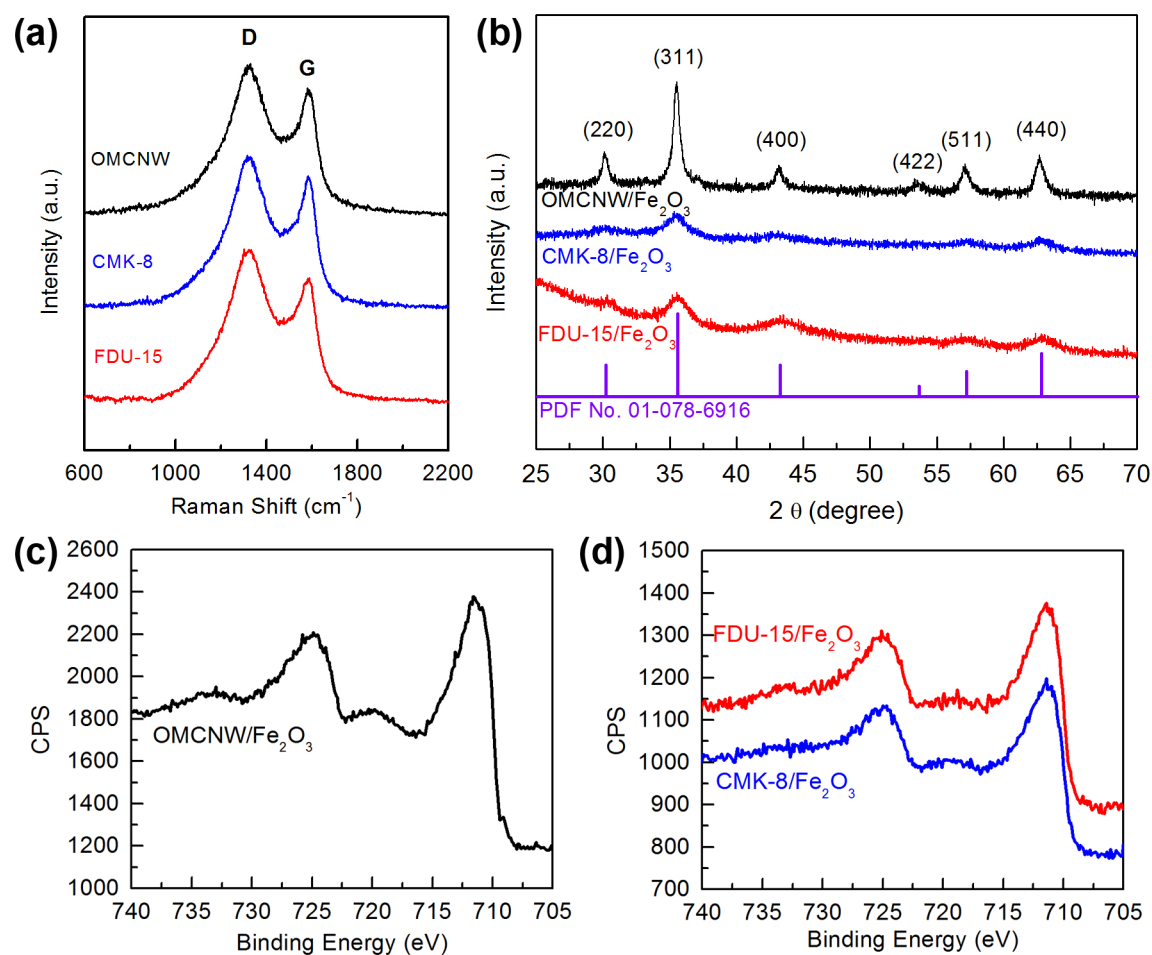


**Figure 4. 1 XRD patterns, Raman Spectra, and XPS spectra of OMC/Fe<sub>2</sub>O<sub>3</sub> composites.**

(a) XRD patterns, (b) Raman Spectra, and (c, d) XPS Fe 2p spectra.

Figure 4.1 b shows the X-ray diffraction (XRD) patterns of three types of OMC/Fe<sub>2</sub>O<sub>3</sub> composites. Due to the high annealing temperature, the Fe<sub>2</sub>O<sub>3</sub> are crystalline structure rather than amorphous. Regardless of the samples, the position and relative intensity of XRD peaks are in good agreement with  $\gamma$ -Fe<sub>2</sub>O<sub>3</sub> (PDF card No. 01-

078-6916).<sup>179</sup> The lower intensity of FDU-15/Fe<sub>2</sub>O<sub>3</sub> and CMK-8/Fe<sub>2</sub>O<sub>3</sub> indicates a smaller Fe<sub>2</sub>O<sub>3</sub> particle growth in the mesopores than in OMCNW/Fe<sub>2</sub>O<sub>3</sub>. To further investigate the iron valence state, the XPS was carried out in Figure 4.1 c,d. For all three types of OMC/Fe<sub>2</sub>O<sub>3</sub> composites, the broad peaks at 711 eV, 719 eV and 724 eV in Fe 2p spectra region match well with the reported values of Fe<sub>2</sub>O<sub>3</sub>.<sup>124</sup>

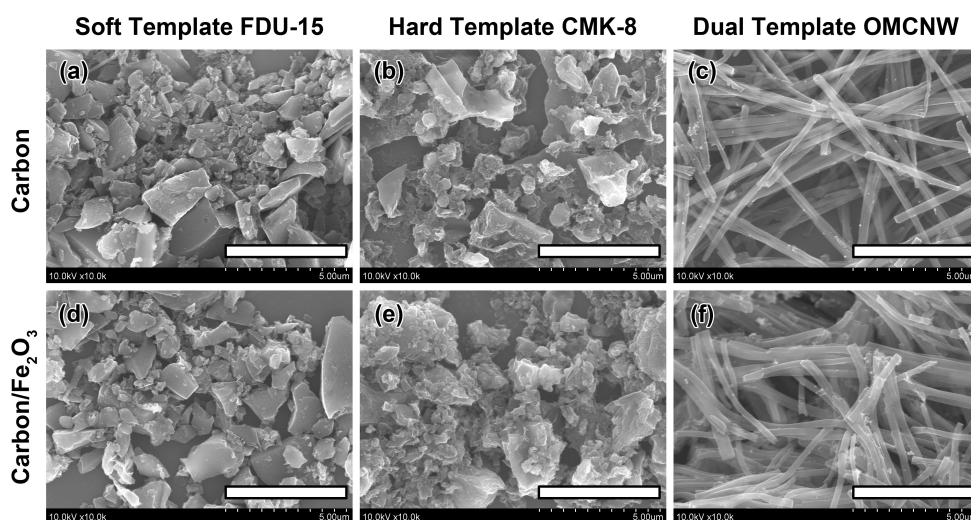


**Figure 4. 2 SEM images of different morphologies in OMCs and OMC/Fe<sub>2</sub>O<sub>3</sub> composites without HNO<sub>3</sub> treatment**

(a) FDU-15, (b) CMK-8, (c) OMCNW, (d) FDU-15/Fe<sub>2</sub>O<sub>3</sub>, (e) CMK-8/Fe<sub>2</sub>O<sub>3</sub>, (f) OMCNW/Fe<sub>2</sub>O<sub>3</sub>. All scale bars are 5  $\mu$ m.

The morphology of three types of OMCs and their derived OMC/Fe<sub>2</sub>O<sub>3</sub> composites were characterized by scanning electron microscopy (SEM). Before loading of Fe<sub>2</sub>O<sub>3</sub>, the soft templated FDU-15 and the hard templated CMK-8 have irregular shapes and particle sizes (Figure 4.2). In contrast, due to the confinement in AAO pores, the dual templated OMCNW shows the typical nanowire morphology with  $\sim$ 200 nm in diameter and  $>$  10  $\mu$ m in length. The growth of Fe<sub>2</sub>O<sub>3</sub> in the mesopores does not change

the original morphologies of all three OMCs. The FDU-15/Fe<sub>2</sub>O<sub>3</sub> and CMK-8/Fe<sub>2</sub>O<sub>3</sub> have a similar irregular shape, while the shape and dimension of the OMCNW were kept in OMCNW/Fe<sub>2</sub>O<sub>3</sub>. The maintained nanowire morphology can help to form interconnected networks which improve the electrical conductivity of the electrode. In addition, compared with the micron-sized particles of bulk OMCs and their derived OMC/Fe<sub>2</sub>O<sub>3</sub>, the nanosized radius of OMCNW and OMCNW/Fe<sub>2</sub>O<sub>3</sub> can significantly enhance the ion accessibility to the center of nanowires.

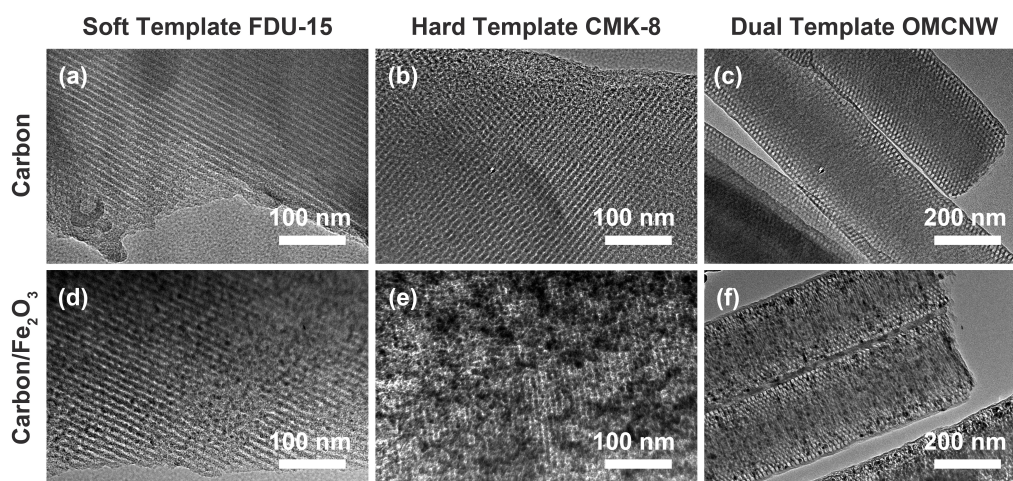


**Figure 4. 3 TEM images of different mesostructured OMCs and OMC/Fe<sub>2</sub>O<sub>3</sub> composites without HNO<sub>3</sub> treatment.**

(a) FDU-15, (b) CMK-8, (c) OMCNW, (d) FDU-15/Fe<sub>2</sub>O<sub>3</sub>, (e) CMK-8/Fe<sub>2</sub>O<sub>3</sub>, (f) OMCNW/Fe<sub>2</sub>O<sub>3</sub>.

The mesostructures of different OMCs and their derived OMC/Fe<sub>2</sub>O<sub>3</sub> composites were characterized by transmission electron microscopy (TEM) and N<sub>2</sub> adsorption-desorption. Figure 4.3a-c shows the three types of mesostructures of OMCs derived from different strategies. The soft templated FDU-15 presents 1D columnar mesopores

(Figure 4.3a) which is derived from parallel array of F127 surfactant micelles. The hard templated CMK-8 shows a typical 3D bi-continuous structure (Figure 4.3b) which is the replica of the original mesoporous silica KIT-6. Both FDU-15 and CMK-8 have a similar pore size of  $\sim 4$  nm. In contrast, although the mesopores of OMCNW are also derived from F127 surfactant micelles, the concentric circular mesopores formed instead of parallel columns due to the curved surface in AAO pores. In addition, the pore diameter of OMCNW is  $\sim 9$  nm, about twice of that in FDU-15 and CMK-8. Based on SEM and TEM images, it is clear that  $\text{HNO}_3$  treatment does not influence the mesostructure and morphologies of OMC materials.

$\text{N}_2$  adsorption-desorption was carried out to quantitatively determine the mesoporous structures of OMCs and OMC/ $\text{Fe}_2\text{O}_3$  composites. The black curves in Figure 4.4a-c shows the isotherms of OMCs, which are all type-IV curve with hysteresis loop typically for mesopores<sup>125</sup>. Based on the adsorption branches, the pore size distributions are drawn in Figure 4.4d-f, and detailed textural parameters are listed in Table 4.1. The pore sizes of FDU-15, CMK-8, and OMCNW are 4.1 nm, 4.0 nm, and 8.9 nm, respectively, which are in good agreement with TEM observations. In addition to the doubled pore size, OMCNW also shows the highest surface area and pore volume among the three OMCs.

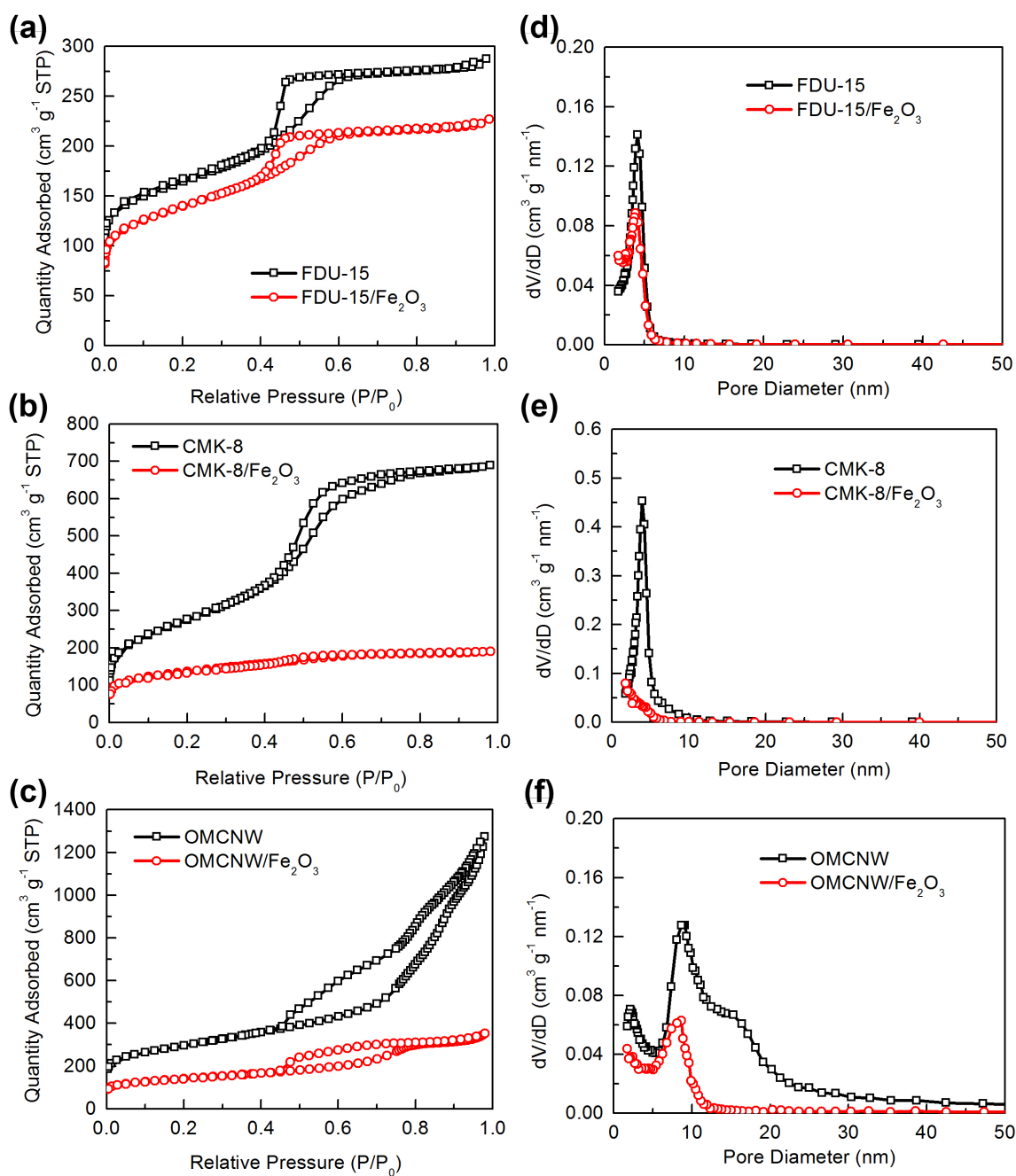


**Figure 4. 4**  $N_2$  adsorption-desorption isotherms and Pore size distributions of OMCs and OMC/ $Fe_2O_3$  composites.

For the LIB materials, the larger pore size is favored for faster ion transport, while the larger surface area enables a better contact between  $Fe_2O_3$  and the carbon framework. In addition, the increased pore volume can uptake more  $Fe(NO_3)_3$

precursors and thus increase the Fe<sub>2</sub>O<sub>3</sub> loading amount, which has been proved by ICP-OES. After treatment by 45 wt % of Fe(NO<sub>3</sub>)<sub>3</sub> aqueous solution, the Fe<sub>2</sub>O<sub>3</sub> loading amount for soft templated FDU-15, hard templated CMK-8, and dual templated OMCNW are 15.1 %, 35.8 % and 45.0 %, respectively, which is consistent with the pore volume sequence of FDU-15 < CMK-8 < OMCNW. It should point out that due to less hydrophilicity in untreated OMCs, their iron oxide loading amount is smaller than the HNO<sub>3</sub> treated ones, regardless of mesostructures and morphologies.

**Table 4. 1 N<sub>2</sub> adsorption-desorption properties of OMCs & OMC/Fe<sub>2</sub>O<sub>3</sub> composites\***

Sample ID	<i>d</i> (nm)	<i>S<sub>t</sub></i> (m <sup>2</sup> g <sup>-1</sup> )	<i>V<sub>t</sub></i> (cm <sup>3</sup> g <sup>-1</sup> )	<i>V<sub>meso</sub></i> (cm <sup>3</sup> g <sup>-1</sup> )	$\Delta V_{meso}$ (%)
FDU-15	4.1	586	0.321	0.310	-
FDU-15/Fe <sub>2</sub> O <sub>3</sub>	3.8	491	0.264	0.235	10.6
CMK-8	4.0	977	0.930	0.915	-
CMK-8/Fe <sub>2</sub> O <sub>3</sub>	< 1.7	480	0.175	0.152	74.1
OMCNW	8.9	1041	1.804	1.557	-
OMCNW/Fe <sub>2</sub> O <sub>3</sub>	8.6	498	0.444	0.399	53.4

\* All data are calculated from adsorption branches.

*d*: pore diameter;

*S<sub>t</sub>* and *V<sub>t</sub>*: total surface area and pore volume;

*V<sub>meso</sub>*: mesopore (2 nm < *d* < 50 nm) volume;

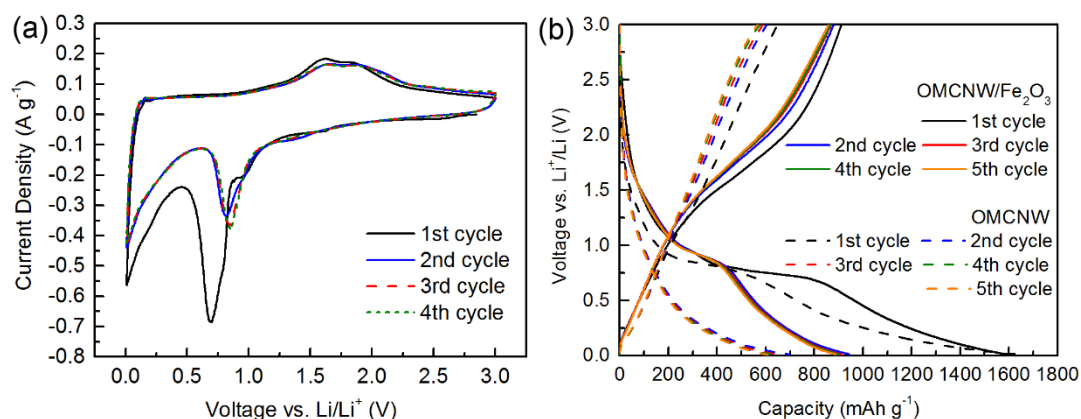
$\Delta V_{meso}$  %: normalized mesopore volume change after Fe<sub>2</sub>O<sub>3</sub> loading based on original carbon.

Figure 4.3 compares the mesostructures of OMCs before and after Fe<sub>2</sub>O<sub>3</sub> loading. As expected, the mesostructure is well preserved in FDU-15 and OMCNW (Figure 4.3d,f), both of which use a soft template as the mesostructure directing agent. In contrast, the mesopores are indistinct after Fe<sub>2</sub>O<sub>3</sub> loading in hard templated CMK-8

(Figure 4.3e), indicating a partial structure collapse happened during the Fe<sub>2</sub>O<sub>3</sub> loading process. However, part of the ordered mesopores can still be found in CMK-8/Fe<sub>2</sub>O<sub>3</sub>, which might due to the smaller Fe<sub>2</sub>O<sub>3</sub> loading amount and thicker nanobridges in CMK-8 without HNO<sub>3</sub> treatment.

The porosity change was quantitatively evaluated by the mesopore volume change shown in Table 4.1. Again, we use  $\Delta V_{meso} \%$  to reflect the relative mesoporous volume decrease in Fe<sub>2</sub>O<sub>3</sub> loading process. As shown in Table 4.1, the 10.6 % of  $\Delta V_{meso} \%$  in FDU-15/Fe<sub>2</sub>O<sub>3</sub> indicates most of the mesopores are well preserved. Considering that the Fe<sub>2</sub>O<sub>3</sub> % in OMCNW/Fe<sub>2</sub>O<sub>3</sub> is three times higher than that in FDU-15/Fe<sub>2</sub>O<sub>3</sub>, the relatively larger  $\Delta V_{meso} \%$  of 53.4 % is expected in OMCNW and indicates the stable mesostructure in OMCNW. Compared with OMCNW/Fe<sub>2</sub>O<sub>3</sub>, although CMK-8/Fe<sub>2</sub>O<sub>3</sub> has a lower Fe<sub>2</sub>O<sub>3</sub> %, the  $\Delta V_{meso} \%$  is much higher (74.1 %), which indicates a collapse of the mesopores after loading Fe<sub>2</sub>O<sub>3</sub>, and is in good agreement with TEM observations. As we discussed before,<sup>44</sup> the unstable mesostructure in CMK-8 is due to the fragile nano-bridges derived from the micropores (<2 nm) in original mesoporous silica KIT-6 template.<sup>123</sup> These nanobridges are easily broken by the H<sub>2</sub>O or NO<sub>x</sub> gasses generated in solvent evaporation and Fe(NO<sub>3</sub>)<sub>3</sub> decomposition processes, leading to the collapse of the CMK-8 structure. The structure degradation is less likely to happen in soft template participated mesostructures such as FDU-15 and OMCNW because the shape of their mesopores is column like (Figure 6) which is very stable upon guest nanoparticle loading.

### 4.3.2 Electrochemical performance as anode materials of LIBs



**Figure 4. 5 CV and GV curves of OMCNW/Fe<sub>2</sub>O<sub>3</sub>.**

(a) CV curves of OMCNW/Fe<sub>2</sub>O<sub>3</sub> at a scan rate of 0.1 mV s<sup>-1</sup>, (b) lithiation/delithiation profiles of OMCNW/Fe<sub>2</sub>O<sub>3</sub> (solid lines) and OMCNW (dash lines) at a current density of 0.1 A g<sup>-1</sup>. All the capacities were calculated based on the mass of entire composites.

To characterize the electrochemical behaviors of OMC/Fe<sub>2</sub>O<sub>3</sub>, cyclic voltammetry (CV) was conducted on the OMCNW/Fe<sub>2</sub>O<sub>3</sub> at ambient temperature at a scan rate of 0.1 mV s<sup>-1</sup> with the voltage window of 0.01–3.0 V vs. Li/Li<sup>+</sup> (Figure 4.5 a). During the cathodic process in the first cycle, two peaks are observed at 0.70 V and 0.94 V, which correspond to lithium ion intercalation, reduction of Fe(III) to Fe(II) and Fe(0), and the irreversible formation of solid electrolyte interface (SEI).<sup>180, 181</sup> Another cathodic peak near 0 V can be attributed to Li<sup>+</sup> insertion into carbon.<sup>106</sup> In the anodic process, two broad overlapping peaks located at 1.62 V and 1.80 V can be assigned to the oxidation of Fe(0) to Fe(II), and subsequently to Fe(III).<sup>182</sup> In the second cycle, only one cathodic peak for Fe is observed at 0.8 V, which is due to the irreversible iron oxide phase transformation and SEI formation. Importantly, after the third cycle, both cathodic and

anodic peak positions and intensities were nearly unchanged, indicating a stable lithiation/delithiation process.

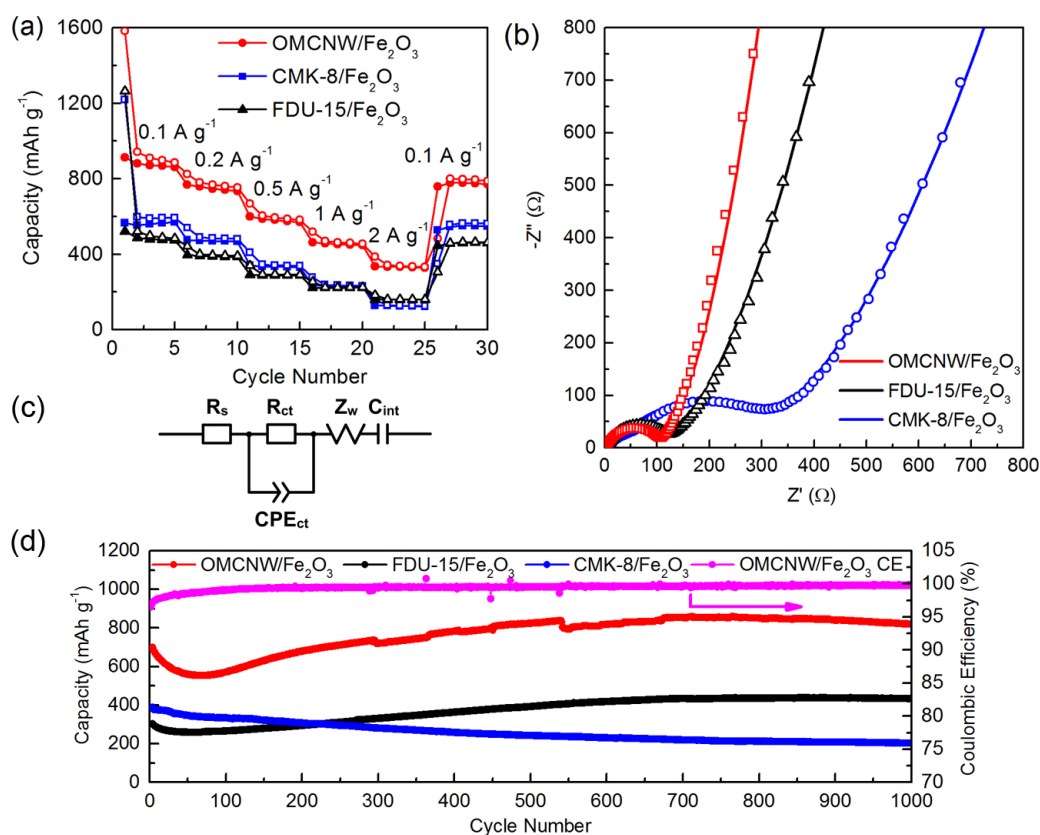


**Figure 4. 6 Rate capability, Nyquist plots, equivalent circuit, Cycling performances, and Coulombic efficiency of OMC/Fe<sub>2</sub>O<sub>3</sub> composites.**

(a) Rate capability, open points: lithiation, solid points: delithiation. (b) Nyquist plots, (c) equivalent circuit. (d) Cycling performances at a current density of 0.5 A g<sup>-1</sup>, pink curve shows the Coulombic efficiency of OMCNW/Fe<sub>2</sub>O<sub>3</sub>, the first 3 cycles are at 0.1 A g<sup>-1</sup> for activation of electrodes (For clarity, data are not shown here).

The capacity improvement from Fe<sub>2</sub>O<sub>3</sub> loading was studied by comparing charge/discharge curves of OMCNW and OMCNW/Fe<sub>2</sub>O<sub>3</sub> at a current density of 0.1 A g<sup>-1</sup> and a voltage window of 0.01 – 3.00 V vs. Li/Li<sup>+</sup>. As shown in Figure 4.5 b, the

initial lithiation and delithiation capacities are 1621 and 650 mAh g<sup>-1</sup>. In the second lithiation, the capacity drops to 698 mAh g<sup>-1</sup> and then remains stable in the following cycles. This reversible capacity is much higher than the theoretical capacity of graphite (372 mAh g<sup>-1</sup>, corresponding to LiC<sub>6</sub>). Such a large capacity is mainly due to the large surface area which provides more structural defects and the heteroatom (N, O) doping in graphitic structures.<sup>183</sup> However, the large surface area also leads to more interaction between electrode and electrolyte, which promotes electrolyte decomposition and SEI formation.<sup>184</sup> Therefore, there is a relatively large irreversible capacity of 923 mAh g<sup>-1</sup> during the first cycle. In comparison, after loaded with Fe<sub>2</sub>O<sub>3</sub>, the OMCNW/Fe<sub>2</sub>O<sub>3</sub> shows first lithiation and delithiation capacities of 1583 and 913 mAh g<sup>-1</sup>. In the 2<sup>nd</sup> cycle, 943 mAh g<sup>-1</sup> lithiation capacity is preserved, corresponding to a 640 and 943 mAh g<sup>-1</sup> irreversible and reversible capacities, respectively. The decreased irreversible capacity is mainly due to the smaller surface area in OMCNW/Fe<sub>2</sub>O<sub>3</sub>, which is only half of OMCNW (Table 4.1) and can effectively reduce the side reactions and SEI formation. Importantly, the decreased surface area did not reduce the reversible capacity of OMCNW/Fe<sub>2</sub>O<sub>3</sub> composite. Instead, the OMCNW/Fe<sub>2</sub>O<sub>3</sub> shows a 50 % capacity improvement. Comparing the charge-discharge curves of OMCNW and OMCNW/Fe<sub>2</sub>O<sub>3</sub> in Figure 4.5b, this significant capacity increase is mainly due to the discharge and charge plateau at 0.8 V and 1.7 V, which correspond to the lithiation and delithiation of Fe<sub>2</sub>O<sub>3</sub> in CV curves. Therefore, the enhancement of capacity in OMCNW/Fe<sub>2</sub>O<sub>3</sub> is due to the introduction of Fe<sub>2</sub>O<sub>3</sub>, which has a high theoretical Li<sup>+</sup>

capacity of 1007 mAh g<sup>-1</sup>. Remarkably, the capacities are almost same between the 2<sup>nd</sup> and the 5<sup>th</sup> cycles, indicating a highly reversible lithium intercalation process after the second cycle.

To highlight the superiority of the unique OMCNW/Fe<sub>2</sub>O<sub>3</sub> composite as a LIB anode material, the capacity performance of soft templated FDU-15/Fe<sub>2</sub>O<sub>3</sub> and hard templated CMK-8/Fe<sub>2</sub>O<sub>3</sub> were tested and compared in Figure 4.6a. The capacity of dual templated OMCNW/Fe<sub>2</sub>O<sub>3</sub> is much higher than the other two composites derived from single template method. More importantly, the rate capability of OMCNW/Fe<sub>2</sub>O<sub>3</sub> is much better than other two OMC/Fe<sub>2</sub>O<sub>3</sub>. In particular, after 5 cycles at 0.1 A g<sup>-1</sup>, the lithiation capacity of OMCNW/Fe<sub>2</sub>O<sub>3</sub> is stabilized at 886 mAh g<sup>-1</sup>. Even at a high current density of 2 A g<sup>-1</sup>, it still retains a specific capacity of 342 mAh g<sup>-1</sup>, which is 39 % of the capacity at 0.1 A g<sup>-1</sup>. In comparison, the lithiation capacity of FDU-15/Fe<sub>2</sub>O<sub>3</sub> and CMK-8/Fe<sub>2</sub>O<sub>3</sub> are only 485 and 592 mAh g<sup>-1</sup> at 0.1 A g<sup>-1</sup>, which is only about half of the OMCNW/Fe<sub>2</sub>O<sub>3</sub>. At a high current density of 2 A g<sup>-1</sup>, the capacities of FDU-15/Fe<sub>2</sub>O<sub>3</sub> and CMK-8/Fe<sub>2</sub>O<sub>3</sub> dramatically decreased to 160 and 125 mAh g<sup>-1</sup>, respectively, corresponding to 33 % and 21 % of their slow rate capacities.

To better understand the reason for the large electrochemical performance difference, the rate capability of three different mesostructures OMC/Fe<sub>2</sub>O<sub>3</sub> and their originate OMCs are compared in Figure 4.7. For the soft templated FDU-15 which has the stable mesopores after loading of Fe<sub>2</sub>O<sub>3</sub>, the ordered porous structure is maintained for good Li<sup>+</sup> accessibility of the inner carbon and Fe<sub>2</sub>O<sub>3</sub>. Therefore, FDU-15/Fe<sub>2</sub>O<sub>3</sub> illustrates a capacity improvement compared with bare FDU-15 (Figure 4.7a). However,

due to the small loading amount of  $\text{Fe}_2\text{O}_3$  in the small pore volume, the capacity gained from  $\text{Fe}_2\text{O}_3$  is limited, and the total capacity is still not very high. On the contrary, although the large pore volume in hard templated CMK-8 results in a higher loading of  $\text{Fe}_2\text{O}_3$ , the capacity of CMK-8/ $\text{Fe}_2\text{O}_3$  is even smaller than its originate CMK-8 (Figure 4.7b), and lost most of its capacity at high current density. This capacity loss is mostly due to the partially collapsed mesostructures shown in Figure 4.3e, which prohibited the ion mobility inside the materials. As a combination of soft and hard template methods, the dual template strategy exhibits the advantages of both templates. The OMCNW herein have a large pore volume which allows high  $\text{Fe}_2\text{O}_3$  loading, while the stable carbon framework keeps the ordered mesostructure in OMCNW/ $\text{Fe}_2\text{O}_3$ . In addition to the ordered mesopores and high pore volume, the nanowire morphology also facilitates the ion transportation along its nano-sized radius. Therefore, as shown in Figure 4.7c, the OMCNW shows a  $\sim 50\%$  capacity improvement with a good rate capability.

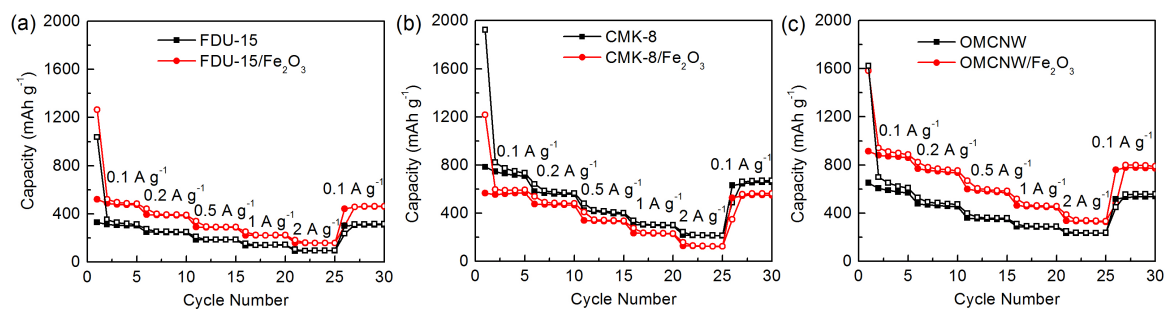


**Figure 4. 7 Comparison of rate performance in different structures OMCs.**

(a) FDU-15 and FDU-15/ $\text{Fe}_2\text{O}_3$ , (b) CMK-8 and CMK-8/ $\text{Fe}_2\text{O}_3$ , and (c) OMCNW and OMCNW/ $\text{Fe}_2\text{O}_3$ . Open points: lithiation, solid points: delithiation

The good ion accessibility of OMCNW/ $\text{Fe}_2\text{O}_3$  is proven by the electrochemical impedance spectroscopy (EIS). Figure 4.6 b shows the Nyquist plots of different

OMC/Fe<sub>2</sub>O<sub>3</sub>, where the experimental data are displayed in symbols and the fitted spectra are drawn in lines. All samples show similar shape and can be fitted to an equivalent circuit (Figure 4.6c) used for various metal oxide anode systems.<sup>180, 185</sup>

The equivalent circuit consists of several components. The solution resistance ( $R_s$ ) represents the electrolyte and other cell component resistance. The charge transfer ( $R_{ct}$ ) resistances can be used to evaluate Li<sup>+</sup> transfer through the electrode-electrolyte interface. The Warburg impedance ( $Z_w$ ) is used to evaluate the Li<sup>+</sup> transportation through the pores between particles/nanowires and within the mesopores inside the particles/nanowires. The intercalation capacitance ( $C_{int}$ ) and a constant phase element ( $CPE_{ct}$ ) represent the capacitance in the intercalation process and at the electrode-electrolyte interface, respectively. The  $R_{ct}$  and  $Z_w$  are particularly important to evaluate the lithium ion accessibility. The  $R_{ct}$  is related with the depressed semicircle in the high-frequency region. The fitting results show that the  $R_{ct}$  is similar in dual template OMCNW/Fe<sub>2</sub>O<sub>3</sub> (97  $\Omega$ ) and soft template FDU-15/Fe<sub>2</sub>O<sub>3</sub> (113  $\Omega$ ), but is much larger in hard template CMK-8/Fe<sub>2</sub>O<sub>3</sub> (302  $\Omega$ ), which indicates a favorable ion transportation through uniform and stable SEI layers in soft and dual templated OMC/Fe<sub>2</sub>O<sub>3</sub> composites. The Warburg impedance ( $Z_w$ ) is related to the tilted line in the low-frequency region. Since more mesopores remain in FDU-15/Fe<sub>2</sub>O<sub>3</sub> than in CMK-8/Fe<sub>2</sub>O<sub>3</sub>, the  $Z_w$  of FDU-15/Fe<sub>2</sub>O<sub>3</sub> (188  $\Omega$ ) is only half of the CMK-8/Fe<sub>2</sub>O<sub>3</sub> (391  $\Omega$ ). For OMCNW/Fe<sub>2</sub>O<sub>3</sub>, in addition to the well-preserved mesoporous systems, the small radius of nanowire and larger porosity also improve ion mobility. Therefore,

OMCNW/Fe<sub>2</sub>O<sub>3</sub> shows the smallest  $Z_w$  of 111  $\Omega$ . The overall Li<sup>+</sup> transfer resistances is OMCNW/Fe<sub>2</sub>O<sub>3</sub> > FDU-15/Fe<sub>2</sub>O<sub>3</sub> > CMK-8/Fe<sub>2</sub>O<sub>3</sub>, which is in good agreement with their rate capability of OMCNW/Fe<sub>2</sub>O<sub>3</sub> > FDU-15/Fe<sub>2</sub>O<sub>3</sub> > CMK-8/Fe<sub>2</sub>O<sub>3</sub>.

The excellent cyclability and Coulombic efficiency of OMCNW/Fe<sub>2</sub>O<sub>3</sub> were demonstrated in Figure 4.6d. The electrode were cycled at a current density of 0.5 A g<sup>-1</sup> for 1000 cycles after being activated for 3 cycles at 0.1 A g<sup>-1</sup>. During the first 70 cycles, there is a slow capacity decay, which might be due to the further formation of SEI layer inside the mesopores, and the gradual irreversible phase transformation of Fe<sub>2</sub>O<sub>3</sub> (reaction 4.1).<sup>186, 187</sup> After the 70<sup>th</sup> cycle, the electrode keeps a very long and stable cycling with a reversible capacity of 819 mAh g<sup>-1</sup> after 1000 cycles. Some little capacity variation at about 300<sup>th</sup> and 550<sup>th</sup> cycles are due to the vibration of test station. It is noteworthy that the capacity slowly increases after 100 cycles, which is very common for the metal oxide electrodes.<sup>175, 187-189</sup> The reason for this capacity increase might be the reversible formation of a gel-like polymeric layer from electrolyte decomposition (reaction 4.2),<sup>29, 190</sup> or the activation of active materials.<sup>174, 191</sup> Remarkably, the OMCNW/Fe<sub>2</sub>O<sub>3</sub> presents good Coulombic efficiency (CE) throughout the cycling. The CE at the 5<sup>th</sup> cycle is 96.5 %, and quickly increased to 98.7 % at the 70<sup>th</sup> cycle, then increased to 99.8 % at the 1000<sup>th</sup> cycle. This high Coulombic efficiency indicates highly reversible lithium ion insertion/extraction in OMCNW/Fe<sub>2</sub>O<sub>3</sub> composite electrode. The excellent cyclability and CE are ascribed to the interconnected nanowire network that favors fast electron transport, and effective ion transportation through nano-sized radius

into well preserved mesopores. In addition, as the  $\text{Fe}_2\text{O}_3$  nanoparticles are homogeneously encapsulated in the mesopores, the stable carbon framework and the large mesopore volume can effectively buffer lithiation-induced volume expansion of  $\text{Fe}_2\text{O}_3$  and prevent aggregation of  $\text{Fe}_2\text{O}_3$  nanoparticles. All of these factors ensure an excellent electrochemical cycling performance.

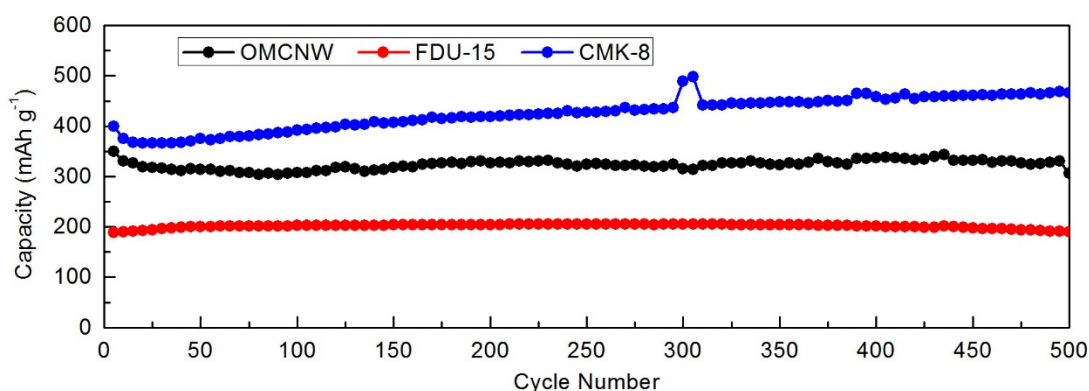
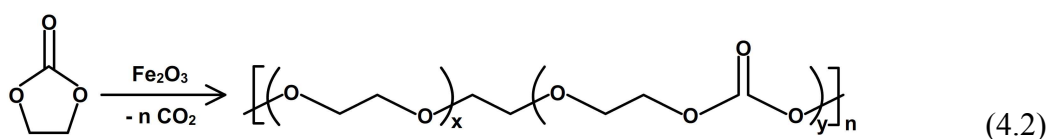


**Figure 4. 8** Cycling performance of FDU-15, CMK-8, and OMCNW.

The first 3 cycles are at 0.1 A g<sup>-1</sup> for activation of electrodes (For clarity, data are not shown).

In comparison, the cycling performance of soft templated FDU-15/ $\text{Fe}_2\text{O}_3$  and hard templated CMK-8/ $\text{Fe}_2\text{O}_3$  tested under the same conditions are also displayed in Figure 4.6d. Despite the much smaller capacity, the FDU-15/ $\text{Fe}_2\text{O}_3$  shows a similar trend as OMCNW/ $\text{Fe}_2\text{O}_3$ . The capacity decreases in the first 60 cycles, then slowly increases

and is stabilized in the following cycles. The capacity after 1000 cycles is 434 mAh g<sup>-1</sup>, which is larger than the initial capacity. In contrast, the capacity of CMK-8/Fe<sub>2</sub>O<sub>3</sub> decreases throughout the 1000 cycles. The capacity at the 4<sup>th</sup> and the 1000<sup>th</sup> cycles are 388 and 203 mAh g<sup>-1</sup>, respectively, implying a capacity retention of 52.3 %.

In order to discover the reason for the poor cyclability of CMK-8/Fe<sub>2</sub>O<sub>3</sub>, the cycling performance of three different OMCs were tested (Figure 4.8). Clearly, all OMCs maintain stable capacities up to 500 cycles, indicating that the unstable cyclability in CMK-8/Fe<sub>2</sub>O<sub>3</sub> is not originated from CMK-8 itself, but due to the introduced Fe<sub>2</sub>O<sub>3</sub>.

**Table 4. 2 Estimated volume changes during lithiation process in OMC/Fe<sub>2</sub>O<sub>3</sub> composites**

Sample ID	$V_{Fe_2O_3}$ (cm <sup>3</sup> g <sup>-1</sup> )	$\Delta V_{Fe_2O_3}$ (cm <sup>3</sup> g <sup>-1</sup> )	$V_C$ (cm <sup>3</sup> g <sup>-1</sup> )	$\Delta V_C$ (cm <sup>3</sup> g <sup>-1</sup> )	$\Delta V_t$ (cm <sup>3</sup> g <sup>-1</sup> )	$V_t$ (cm <sup>3</sup> g <sup>-1</sup> )	$\Delta V_t/V_t$ (%)
OMCNW/Fe <sub>2</sub> O <sub>3</sub>	0.0858	0.172	0.24	0.024	0.196	0.444	44
FDU-15/Fe <sub>2</sub> O <sub>3</sub>	0.0288	0.058	0.38	0.037	0.095	0.264	36
CMK-8/Fe <sub>2</sub> O <sub>3</sub>	0.0683	0.137	0.28	0.028	0.165	0.175	94

$V_{Fe_2O_3}$ : Fe<sub>2</sub>O<sub>3</sub> volume based on Fe<sub>2</sub>O<sub>3</sub> density of 5.242 g cm<sup>-3</sup>;

$V_C$ : carbon volume based on graphite density of 2.267 g cm<sup>-3</sup>;

$\Delta V_{Fe_2O_3}$ : Fe<sub>2</sub>O<sub>3</sub> volume expansion estimated from 200 % Fe<sub>2</sub>O<sub>3</sub> volume increase;<sup>75</sup>

$\Delta V_C$ : carbon volume expansion estimated from 10 % graphite volume increase;<sup>192</sup>

$\Delta V_t$ : total volume expansion from  $\Delta V_{Fe_2O_3}$  and  $\Delta V_C$ ;

$V_t$ : total volume from N<sub>2</sub> sorption-desorption;

$\Delta V_t/V_t$ : ration between changed volume and total volume.

In fact, as reported previously, the major reasons for rapid capacity decay of the iron oxide are the large volume change and particle aggregation of iron oxide during electrochemical cycling.<sup>189</sup> Considering the small mesopore volume and unstable

mesostructure in CMK-8/Fe<sub>2</sub>O<sub>3</sub>, it is likely that the poor cyclability results from the Fe<sub>2</sub>O<sub>3</sub> volume expansion and structural collapse. Here, we estimate the volume change during the lithiation process and compare them with the total volume in each of the OMC/Fe<sub>2</sub>O<sub>3</sub> composites (Table 4.2). During lithium intercalation, the volume increases in dual templated OMCNW/Fe<sub>2</sub>O<sub>3</sub> (0.196 cm<sup>3</sup> g<sup>-1</sup>) and soft templated FDU-15/Fe<sub>2</sub>O<sub>3</sub> (0.095 cm<sup>3</sup> g<sup>-1</sup>) are less than half of the total volume they can buffer (0.444 and 0.264 cm<sup>3</sup> g<sup>-1</sup>, respectively). Therefore, their mesostructures can endure the volume change during cycling. However, the volume expansion of CMK-8/Fe<sub>2</sub>O<sub>3</sub> (0.165 cm<sup>3</sup> g<sup>-1</sup>) is very close to the total volume (0.175 cm<sup>3</sup> g<sup>-1</sup>) it can afford. Considering the fragile carbon framework, the remaining mesostructure will gradually collapse upon cycling. This different structure stability in various OMC/Fe<sub>2</sub>O<sub>3</sub> composites is proven by the TEM( Figure 4.9). The soft templated FDU-15/Fe<sub>2</sub>O<sub>3</sub> and dual templated OMCNW/Fe<sub>2</sub>O<sub>3</sub> still preserve their typical cylindrical and circular mesostructures even after 500 cycles. In contrast, the partially preserved ordered 3D mesopores in CMK-8/Fe<sub>2</sub>O<sub>3</sub> completely disappears after 500 cycles (Figure 4.9b). The gradually collapsed mesoporous network in hard templated CMK-8/Fe<sub>2</sub>O<sub>3</sub> would block some part of materials from lithium ions or electrons, leading to a continuous capacity decay upon electrochemical cycling.

Overall, the remaining capacity of OMCNW/Fe<sub>2</sub>O<sub>3</sub> is 819 mAh g<sup>-1</sup> after 1000 cycles at 0.5 A g<sup>-1</sup>. This high capacity as well as good cyclability are not only better than our control samples, namely, FDU-15/Fe<sub>2</sub>O<sub>3</sub> (434 mAh g<sup>-1</sup> after 1000 cycles at 0.5

A  $\text{g}^{-1}$ ), and CMK-8/ $\text{Fe}_2\text{O}_3$  (203 mAh  $\text{g}^{-1}$  after 1000 cycles at 0.5 A  $\text{g}^{-1}$ ), but also better than other previous reported OMC/iron oxide composites, such as OMC/ $\text{Fe}_3\text{O}_4$  (697.4 mAh  $\text{g}^{-1}$  at 0.5 A  $\text{g}^{-1}$  after 130 cycles in different rates),<sup>96</sup> CMK-5/ $\text{Fe}_2\text{O}_3$  (683 mAh  $\text{g}^{-1}$  after 100 cycles at 0.2 A  $\text{g}^{-1}$ ),<sup>24</sup> CMK-5/ $\text{Fe}_2\text{O}_3$ /PPy (785 mAh  $\text{g}^{-1}$  after 100 cycles at 0.2 A  $\text{g}^{-1}$ ),<sup>75</sup> CMK-3/ $\text{Fe}_3\text{O}_4$  (670 mAh  $\text{g}^{-1}$  after 100 cycles at 1 A  $\text{g}^{-1}$ ),<sup>38</sup> and CMK-3/ $\text{FeO}_x$  (660 mAh  $\text{g}^{-1}$  at 0.1 A  $\text{g}^{-1}$  after 50 cycles in different rates).<sup>25</sup> The better electrochemical performance of OMCNW/ $\text{Fe}_2\text{O}_3$  composite results from its unique nanowire morphology with good conductivity and excellent ion accessibility, as well as its balanced mesostructure with large pore volume and stable carbon.

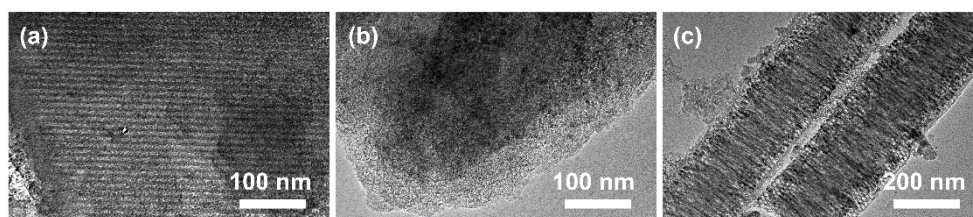


**Figure 4. 9 TEM images of different OMC/ $\text{Fe}_2\text{O}_3$  composites after 500 cycles at a current density of 0.5 A  $\text{g}^{-1}$ .**

(a) FDU-15/ $\text{Fe}_2\text{O}_3$ , (b) CMK/ $\text{Fe}_2\text{O}_3$ , (c) OMCNW/ $\text{Fe}_2\text{O}_3$ .

#### 4.4 Conclusions

In summary, we have synthesized OMCNW/ $\text{Fe}_2\text{O}_3$  composite by incorporating  $\text{Fe}_2\text{O}_3$  nanoparticles into the soft-hard dual template derived ordered mesoporous carbon nanowires. For the first time, OMCNW/ $\text{Fe}_2\text{O}_3$  was used as an anode material for LIBs. The structural properties and electrochemical performances of dual templated

OMCNW/Fe<sub>2</sub>O<sub>3</sub> were compared with soft templated and hard templated OMCs/Fe<sub>2</sub>O<sub>3</sub> composites. Compared with the single templated bulk materials, the nanowire morphology can contribute to a better electrical conductivity and ion accessibility through its micro-sized length and nano-sized radius. Additionally, the pore volume of dual templated OMCNW is five times higher than the soft templated FDU-15, which ensures higher Fe<sub>2</sub>O<sub>3</sub> loading and therefore a larger lithium ion storage capacity. When compared with hard templated CMK-8, the OMCNW presents good mesostructural stability, preventing mesopore collapse under high Fe<sub>2</sub>O<sub>3</sub> content and leading to excellent rate capability and cyclability. Overall, even after 1000 cycles, the OMCNW/Fe<sub>2</sub>O<sub>3</sub> composite was still able to deliver a capacity up to 819 mAh g<sup>-1</sup> under a current density of 0.5 A g<sup>-1</sup>. Our results highlight the synergistic effects of the dual template method, which could be applied to other electrochemical energy storage systems to improve both energy density and power density from an optimized meso-scale porous structure and macro-scale morphology.

## **Chapter 5 Summary and Outlook**

The overall goal of this dissertation is to understand and optimize OMC architecture for a better accommodation and utilization of Fe<sub>2</sub>O<sub>3</sub> guest nanoparticles, and enhance the overall electrochemical energy storage properties of the whole composite. This goal is achieved by the following three steps:

1. Investigate the relationship between mesoporous structures and electrochemical performance of OMC/Fe<sub>2</sub>O<sub>3</sub> composites.

2. Build up one-dimensional OMCNW/Fe<sub>2</sub>O<sub>3</sub> nanowires with balanced mesoporous properties and unique morphologies for the best capacitance performance.

3. Evaluate OMC/Fe<sub>2</sub>O<sub>3</sub> composites as LIBs anode, discover the morphology and porosity effects on LIBs' capacity, rate capability, and cycling stability.

Summary of each chapter include:

From Chapter 2:

I. The collapse of mesopores during the guest NPs loading is discovered. This mesostructure degradation is dependent on Fe<sub>2</sub>O<sub>3</sub> % and OMCs' framework stabilities.

II. The soft template derived OMCs are more stable than the commonly used hard template OMCs.

III. The mesostructure degradation will prohibit ion accessibility in the mesopores, which will strongly influence the electrochemical performance, particularly at a high scan rate.

IV. The surface area, pore volume, and pore tortuosity can determine the carbon capacitance, maximum Fe<sub>2</sub>O<sub>3</sub> %, and ion mobility, respectively, and these effects also

need to be considered when choosing the right carbon structure for the best performance.

From Chapter 3:

I. The dual-template OMCNW have large surface area and pore volume and stable meso-architecture, combining advantages of the two others template methods.

II. The nanowire morphology together with well-preserved mesopores leads to a good ion accessibility, which results in an excellent rate performance.

III. The stable mesostructure also has a positive effect on long-term cycling stability.

From Chapter 4:

I. The nanowire morphology and high pore volume contribute to a better  $\text{Li}^+$  accessibility and higher  $\text{Fe}_2\text{O}_3$  utilization in OMCNW/ $\text{Fe}_2\text{O}_3$ , result in a large overall capacity and rate performance.

II. The partially collapsed mesostructure in CMK-8/ $\text{Fe}_2\text{O}_3$  composite inhibits its ion transportation into the particles, resulting in an even worse capacitive performance compared with CMK-8.

III. The FDU-15/ $\text{Fe}_2\text{O}_3$  and the OMCNW/ $\text{Fe}_2\text{O}_3$  can last 1000 cycles without capacity fading, but the CMK-8/ $\text{Fe}_2\text{O}_3$  lost half of its original capacity after 1000 cycles. The *ex Situ* TEM showed the major reason for the unstable cycling performance in CMK-8/ $\text{Fe}_2\text{O}_3$  is the structure collapse arising from the insufficient pore volume and the fragile framework.

As summarized in Figure 5.1, this dissertation has been focused on understanding

the roles of structures to improve the ionic and electronic transfer processes in energy storage. Our results emphasize the new considerations regarding material morphology, mesoporous symmetry, and structure degradation. The impact of this work is not limited to supercapacitors and LIBs only, and the methodology can be utilized by others for diverse composites material and various applications.

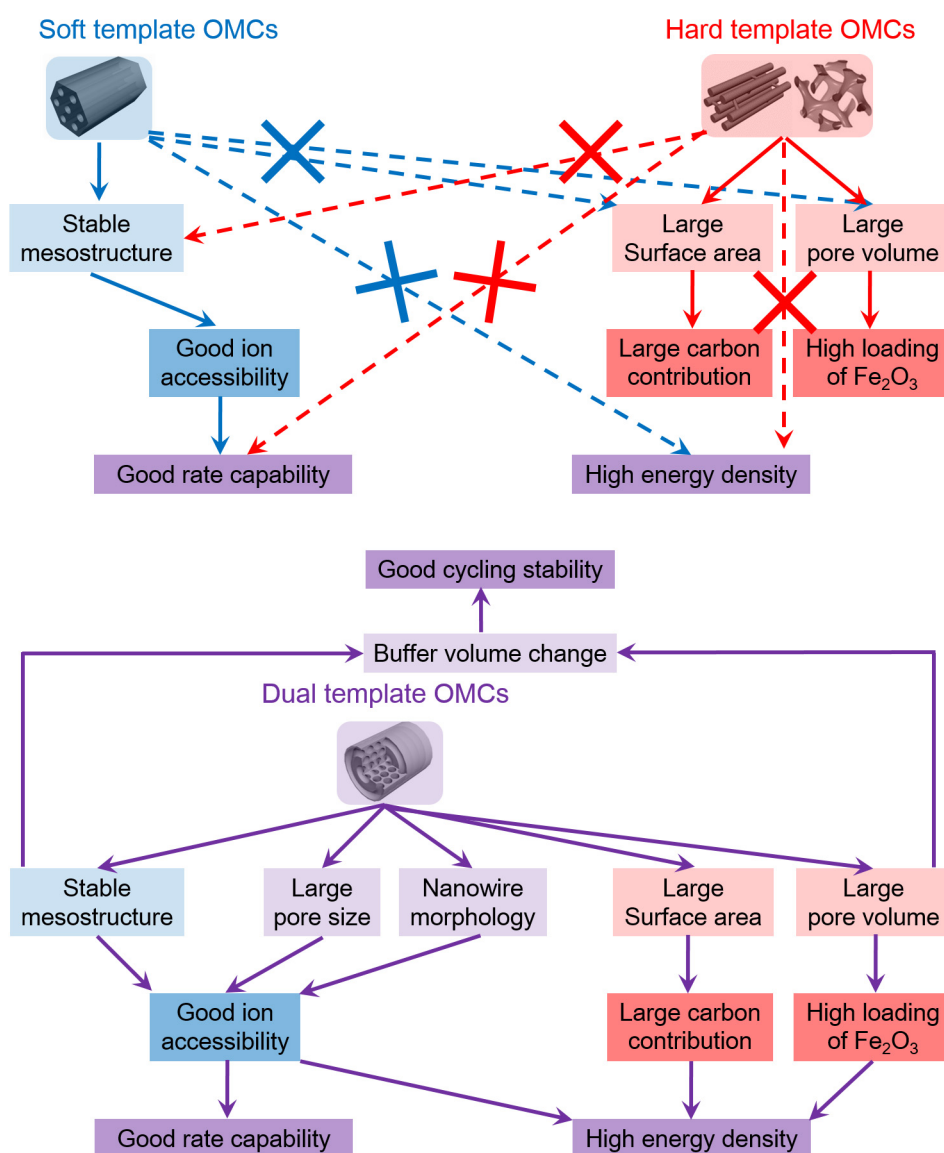


**Figure 5. 1 Comparison of structure and electrochemical properties of OMCs from different synthesis strategies.**

## Publication

Portions of Chapter 2 have been published in

Hu, J.; Noked, M.; Gillette, E.; Gui, Z.; Lee, S. B., *Carbon* **2015**, *93* (0), 903-914.

## References

1. Miller, J. R.; Simon, P., *Science* **2008**, *321* (5889), 651-652.
2. Zhang, L. L.; Zhao, X. S., *Chemical Society Reviews* **2009**, *38* (9), 2520-2531.
3. Wang, G. P.; Zhang, L.; Zhang, J. J., *Chemical Society Reviews* **2012**, *41* (2), 797-828.
4. Wu, T. H.; Hesp, D.; Dhanak, V.; Collins, C.; Braga, F.; Hardwick, L. J.; Hu, C. C., *Journal of Materials Chemistry A* **2015**, *3* (24), 12786-12795.
5. Gui, Z.; Duay, J.; Hu, J.; Lee, S. B., *Physical Chemistry Chemical Physics* **2014**, *16* (24), 12332-12340.
6. .
7. Lokhande, C. D.; Dubal, D. P.; Joo, O. S., *Current Applied Physics* **2011**, *11* (3), 255-270.
8. Athouel, L.; Moser, F.; Dugas, R.; Crosnier, O.; Belanger, D.; Brousse, T., *Journal of Physical Chemistry C* **2008**, *112* (18), 7270-7277; Binitha, G.; Soumya, M. S.; Madhavan, A. A.; Praveen, P.; Balakrishnan, A.; Subramanian, K. R. V.; Reddy, M. V.; Nair, S. V.; Nair, A. S.; Sivakumar, N., *Journal of Materials Chemistry A* **2013**, *1* (38), 11698-11704; Xiong, S. L.; Yuan, C. Z.; Zhang, M. F.; Xi, B. J.; Qian, Y. T., *Chemistry-a European Journal* **2009**, *15* (21), 5320-5326; Saravanakumar, B.; Purushothaman, K. K.; Muralidharan, G., *Acs Applied Materials & Interfaces* **2012**, *4* (9), 4484-4490.
9. Ragone, D. V., *Sae Transactions* **1968**, *77*, 131-&.
10. Arico, A. S.; Bruce, P.; Scrosati, B.; Tarascon, J. M.; Van Schalkwijk, W., *Nature Materials* **2005**, *4* (5), 366-377.
11. Lee, K. T.; Cho, J., *Nano Today* **2011**, *6* (1), 28-41.
12. Ji, X. L.; Lee, K. T.; Holden, R.; Zhang, L.; Zhang, J. J.; Botton, G. A.; Couillard, M.; Nazar, L. F., *Nature Chemistry* **2010**, *2* (4), 286-293.
13. Cabana, J.; Monconduit, L.; Larcher, D.; Palacin, M. R., *Advanced Materials* **2010**, *22* (35), E170-E192.
14. Liang, C. D.; Li, Z. J.; Dai, S., *Angewandte Chemie-International Edition* **2008**, *47* (20), 3696-3717.
15. Lee, J. S.; Joo, S. H.; Ryoo, R., *Journal of the American Chemical Society* **2002**, *124* (7), 1156-1157; Kruk, M.; Jaroniec, M.; Ryoo, R.; Joo, S. H., *Journal of Physical Chemistry B* **2000**, *104* (33), 7960-7968.
16. Fang, B. Z.; Kim, J. H.; Kim, M.; Yu, J. S., *Chemistry of Materials* **2009**, *21* (5), 789-796; Gierszal, K. P.; Yoon, S. B.; Yu, J. S.; Jaroniec, M., *Journal of Materials Chemistry* **2006**, *16* (27), 2819-2823.
17. Kyotani, T.; Tsai, L. F.; Tomita, A., *Chemistry of Materials* **1996**, *8* (8), 2109-2113.
18. Wan, Y.; Shi, Y. F.; Zhao, D. Y., *Chemistry of Materials* **2008**, *20* (3), 932-945.
19. Ma, T. Y.; Liu, L.; Yuan, Z. Y., *Chemical Society Reviews* **2013**, *42* (9), 3977-4003; Yang, H. F.; Zhao, D. Y., *Journal of Materials Chemistry* **2005**, *15* (12), 1217-1231.
20. Kim, T. W.; Solovyov, L. A., *Journal of Materials Chemistry* **2006**, *16* (15), 1445-

1455.

21. Jun, S.; Joo, S. H.; Ryoo, R.; Kruk, M.; Jaroniec, M.; Liu, Z.; Ohsuna, T.; Terasaki, O., *Journal of the American Chemical Society* **2000**, *122* (43), 10712-10713.
22. Joo, S. H.; Choi, S. J.; Oh, I.; Kwak, J.; Liu, Z.; Terasaki, O.; Ryoo, R., *Nature* **2001**, *414* (6862), 470-470.
23. Meng, Y.; Gu, D.; Zhang, F. Q.; Shi, Y. F.; Cheng, L.; Feng, D.; Wu, Z. X.; Chen, Z. X.; Wan, Y.; Stein, A.; Zhao, D. Y., *Chemistry of Materials* **2006**, *18* (18), 4447-4464.
24. Han, F.; Li, W. C.; Li, D.; Lu, A. H., *Journal of Energy Chemistry* **2013**, *22* (2), 329-335.
25. Li, Z. Q.; Wang, X. K.; Wang, C. B.; Yin, L. W., *Rsc Advances* **2013**, *3* (38), 17097-17104.
26. Hassan, F. M.; Chen, Z. W.; Yu, A. P.; Chen, Z.; Xiao, X. C., *Electrochimica Acta* **2013**, *87*, 844-852.
27. Xu, G. L.; Chen, S. R.; Li, J. T.; Ke, F. S.; Huang, L.; Sun, S. G., *Journal of Electroanalytical Chemistry* **2011**, *656* (1-2), 185-191.
28. Wang, X. K.; Li, Z. Q.; Yin, L. W., *Crystengcomm* **2013**, *15* (37), 7589-7597.
29. Han, F.; Li, W. C.; Li, M. R.; Lu, A. H., *Journal of Materials Chemistry* **2012**, *22* (19), 9645-9651.
30. Guo, Z. Y.; Zhou, D. D.; Liu, H. J.; Dong, X. L.; Yuan, S. Y.; Yu, A. S.; Wang, Y. G.; Xia, Y. Y., *Journal of Power Sources* **2015**, *276*, 181-188.
31. Ma, J. Y.; Xiang, D.; Li, Z. Q.; Li, Q.; Wang, X. K.; Yin, L. W., *Crystengcomm* **2013**, *15* (34), 6800-6807.
32. Chen, A. L.; Li, C. X.; Tang, R.; Yin, L. W.; Qi, Y. X., *Physical Chemistry Chemical Physics* **2013**, *15* (32), 13601-13610.
33. Yang, M.; Gao, Q. M., *Microporous and Mesoporous Materials* **2011**, *143* (1), 230-235.
34. Zhang, J.; Kong, L. B.; Cai, J. J.; Luo, Y. C.; Kang, L., *Journal of Solid State Electrochemistry* **2010**, *14* (11), 2065-2075.
35. Qu, W. H.; Han, F.; Lu, A. H.; Xing, C.; Qiao, M.; Li, W. C., *Journal of Materials Chemistry A* **2014**, *2* (18), 6549-6557.
36. Zeng, L. X.; Zheng, C.; Deng, C. L.; Ding, X. K.; Wei, M. D., *Acs Applied Materials & Interfaces* **2013**, *5* (6), 2182-2187.
37. Shen, L. F.; Zhang, X. G.; Uchaker, E.; Yuan, C. Z.; Cao, G. Z., *Advanced Energy Materials* **2012**, *2* (6), 691-698.
38. Wu, F.; Huang, R.; Mu, D. B.; Shen, X. Y.; Wu, B. R., *Journal of Alloys and Compounds* **2014**, *585*, 783-789.
39. Grigoriants, I.; Sominski, L.; Li, H. L.; Ifargan, I.; Aurbach, D.; Gedanken, A., *Chemical Communications* **2005**, (7), 921-923.
40. Zhou, Y.; Ko, S.; Lee, C. W.; Pyo, S. G.; Kim, S. K.; Yoon, S., *Journal of Power Sources* **2013**, *244*, 777-782.
41. Cheng, M. Y.; Hwang, B. J., *Journal of Power Sources* **2010**, *195* (15), 4977-4983.
42. Jahel, A.; Darwiche, A.; Ghimbeu, C. M.; Vix-Guterl, C.; Monconduit, L., *Journal of Power Sources* **2014**, *269*, 755-759.

43. Jahel, A.; Ghimbeu, C. M.; Monconduit, L.; Vix-Guterl, C., *Advanced Energy Materials* **2014**, *4* (11).
44. Hu, J.; Noked, M.; Gillette, E.; Gui, Z.; Lee, S. B., *Carbon* **2015**, *93* (0), 903-914.
45. Chae, C.; Kim, J. H.; Kim, J. M.; Sun, Y. K.; Lee, J. K., *Journal of Materials Chemistry* **2012**, *22* (34), 17870-17877.
46. Zeng, L. X.; Zheng, C.; Xi, J. C.; Fei, H. L.; Wei, M. D., *Carbon* **2013**, *62*, 382-388.
47. Sun, B.; Liu, H.; Munroe, P.; Ahn, H.; Wang, G. X., *Nano Research* **2012**, *5* (7), 460-469.
48. Yuan, D.; Zeng, J.; Kristian, N.; Wang, Y.; Wang, X., *Electrochemistry Communications* **2009**, *11* (2), 313-317.
49. Lu, Y.; Wen, Z. Y.; Jin, J.; Cui, Y. M.; Wu, M. F.; Sun, S. J., *Journal of Solid State Electrochemistry* **2012**, *16* (5), 1863-1868.
50. Bastakoti, B. P.; Oveisi, H.; Hu, C. C.; Wu, K. C. W.; Suzuki, N.; Takai, K.; Kamachi, Y.; Imura, M.; Yamauchi, Y., *European Journal of Inorganic Chemistry* **2013**, (7), 1109-1112.
51. Zhao, C. X.; Chen, S. J.; Chen, W.; Yang, Y. X.; Cao, Q., *Ecs Solid State Letters* **2013**, *2* (4), M29-M32.
52. Yu, L.; Zhao, C. X.; Long, X.; Chen, W., *Microporous and Mesoporous Materials* **2009**, *126* (1-2), 58-64.
53. Zhou, Y.; Lee, C. W.; Yoon, S., *Electrochemical and Solid State Letters* **2011**, *14* (10), A157-A160.
54. Cheng, F.; Li, D.; Lu, A. H.; Li, W. C., *Journal of Energy Chemistry* **2013**, *22* (6), 907-913.
55. Jung, H.; Shin, J.; Chae, C.; Lee, J. K.; Kim, J., *Journal of Physical Chemistry C* **2013**, *117* (29), 14939-14946.
56. Dong, X. P.; Shen, W. H.; Gu, J. L.; Xiong, L. M.; Zhu, Y. F.; Li, Z.; Shi, J. L., *Journal of Physical Chemistry B* **2006**, *110* (12), 6015-6019.
57. Patel, M. N.; Wang, X. Q.; Wilson, B.; Ferrer, D. A.; Dai, S.; Stevenson, K. J.; Johnston, K. P., *Journal of Materials Chemistry* **2010**, *20* (2), 390-398.
58. Patel, M. N.; Wang, X. Q.; Slanac, D. A.; Ferrer, D. A.; Dai, S.; Johnston, K. P.; Stevenson, K. J., *Journal of Materials Chemistry* **2012**, *22* (7), 3160-3169.
59. Pinkert, K.; Giebeler, L.; Herklotz, M.; Oswald, S.; Thomas, J.; Meier, A.; Borchardt, L.; Kaskel, S.; Ehrenberg, H.; Eckert, J., *Journal of Materials Chemistry A* **2013**, *1* (15), 4904-4910.
60. Ji, X. L.; Lee, K. T.; Nazar, L. F., *Nature Materials* **2009**, *8* (6), 500-506; Schuster, J.; He, G.; Mandlmeier, B.; Yim, T.; Lee, K. T.; Bein, T.; Nazar, L. F., *Angewandte Chemie-International Edition* **2012**, *51* (15), 3591-3595; See, K. A.; Jun, Y. S.; Gerbec, J. A.; Sprafke, J. K.; Wudl, F.; Stucky, G. D.; Seshadri, R., *Acs Applied Materials & Interfaces* **2014**, *6* (14), 10908-10916.
61. Liang, X. A.; Wen, Z. Y.; Liu, Y.; Zhang, H.; Huang, L. Z.; Jin, J., *Journal of Power Sources* **2011**, *196* (7), 3655-3658; Li, X. L.; Cao, Y. L.; Qi, W.; Saraf, L. V.; Xiao, J.; Nie, Z. M.; Mietek, J.; Zhang, J. G.; Schwenzer, B.; Liu, J., *Journal of Materials*

- Chemistry* **2011**, *21* (41), 16603-16610; Chen, S. R.; Zhai, Y. P.; Xu, G. L.; Jiang, Y. X.; Zhao, D. Y.; Li, J. T.; Huang, L.; Sun, S. G., *Electrochimica Acta* **2011**, *56* (26), 9549-9555; He, G.; Mandlmeier, B.; Schuster, J.; Nazar, L. F.; Bein, T., *Chemistry of Materials* **2014**, *26* (13), 3879-3886.
62. Choi, H. J.; Zhao, X. H.; Kim, D. S.; Ahn, H. J.; Kim, K. W.; Cho, K. K.; Ahn, J. H., *Materials Research Bulletin* **2014**, *58*, 199-203; Nagao, M.; Imade, Y.; Narisawa, H.; Watanabe, R.; Yokoi, T.; Tatsumi, T.; Kanno, R., *Journal of Power Sources* **2013**, *243*, 60-64; Wang, H.; Zhang, C.; Chen, Z.; Liu, H. K.; Guo, Z., *Carbon* **2015**, *81*, 782-787.
63. Lee, J. T.; Kim, H.; Oschatz, M.; Lee, D.-C.; Wu, F.; Lin, H.-T.; Zdyrko, B.; Cho, W. I.; Kaskel, S.; Yushin, G., *Advanced Energy Materials* **2015**, *5* (1).
64. Hu, L. M.; Yu, L.; Zhao, C. X.; Long, X.; Chen, W., *Journal of Wuhan University of Technology-Materials Science Edition* **2010**, *25* (4), 574-578.
65. Kwon, M. S.; Choi, A.; Park, Y.; Cheon, J. Y.; Kang, H.; Jo, Y. N.; Kim, Y. J.; Hong, S. Y.; Joo, S. H.; Yang, C.; Lee, K. T., *Scientific Reports* **2014**, *4*.
66. Wang, Y. G.; Li, H. Q.; Xia, Y. Y., *Advanced Materials* **2006**, *18* (19), 2619-+.
67. Zhang, J.; Kong, L.-B.; Cai, J.-J.; Luo, Y.-C.; Kang, L., *Electrochimica Acta* **2010**, *55* (27), 8067-8073.
68. Wang, J. C.; Yu, X. F.; Li, Y. X.; Liu, Q., *Journal of Physical Chemistry C* **2007**, *111* (49), 18073-18077.
69. Li, L. X.; Song, H. H.; Zhang, Q. C.; Yao, J. Y.; Chen, X. H., *Journal of Power Sources* **2009**, *187* (1), 268-274.
70. Dou, Y. Q.; Zhai, Y. P.; Liu, H. J.; Xia, Y. Y.; Tu, B.; Zhao, D. Y.; Liu, X. X., *Journal of Power Sources* **2011**, *196* (3), 1608-1614.
71. Zhang, Z.; Wang, G.; Li, Y.; Zhang, X.; Qiao, N.; Wang, J.; Zhou, J.; Liu, Z.; Hao, Z., *Journal of Materials Chemistry A* **2014**, *2* (39), 16715-16722.
72. Yan, Y. F.; Cheng, Q. L.; Zhu, Z. J.; Pavlinek, V.; Saha, P.; Li, C. Z., *Journal of Power Sources* **2013**, *240*, 544-550.
73. Yan, Y. F.; Cheng, Q. L.; Wang, G. C.; Li, C. Z., *Journal of Power Sources* **2011**, *196* (18), 7835-7840.
74. Yan, Y. F.; Cheng, Q. L.; Pavlinek, V.; Saha, P.; Li, C. Z., *Electrochimica Acta* **2012**, *71*, 27-32.
75. Han, F.; Li, D.; Li, W.-C.; Lei, C.; Sun, Q.; Lu, A.-H., *Advanced Functional Materials* **2013**, *23* (13), 1692-1700.
76. Ma, G. Q.; Wen, Z. Y.; Jin, J.; Lu, Y.; Rui, K.; Wu, X. W.; Wu, M. F.; Zhang, J. C., *Journal of Power Sources* **2014**, *254*, 353-359.
77. Kim, H.; Cho, J., *Nano Letters* **2008**, *8* (11), 3688-3691.
78. Cao, Y. L.; Cao, J. M.; Zheng, M. B.; Liu, J. S.; Ji, G. B., *Journal of Solid State Chemistry* **2007**, *180* (2), 792-798.
79. Wang, Y. G.; Li, B.; Zhang, C. L.; Tao, H.; Kang, S. F.; Jiang, S.; Li, X., *Journal of Power Sources* **2012**, *219*, 89-93.
80. Li, Z. Q.; Liu, N. N.; Wang, X. K.; Wang, C. B.; Qi, Y. X.; Yin, L. W., *Journal of Materials Chemistry* **2012**, *22* (32), 16640-16648.

81. Liu, R. L.; Shi, Y. F.; Wan, Y.; Meng, Y.; Zhang, F. Q.; Gu, D.; Chen, Z. X.; Tu, B.; Zhao, D. Y., *Journal of the American Chemical Society* **2006**, *128* (35), 11652-11662.
82. Chang, P. Y.; Huang, C. H.; Doong, R. A., *Carbon* **2012**, *50* (11), 4259-4268.
83. Lee, J.; Jung, Y. S.; Warren, S. C.; Kamperman, M.; Oh, S. M.; DiSalvo, F. J.; Wiesner, U., *Macromolecular Chemistry and Physics* **2011**, *212* (4), 383-390.
84. Ishii, Y.; Kanamori, Y.; Kawashita, T.; Mukhopadhyay, I.; Kawasaki, S., *Journal of Physics and Chemistry of Solids* **2010**, *71* (4), 511-514.
85. Lin, Z. X.; Zheng, M. B.; Zhao, B.; Pan, L. J.; Pu, L.; Shi, Y., *Rsc Advances* **2013**, *3* (47), 24882-24885.
86. Zhou, Y.; Kim, Y.; Jo, C.; Lee, J.; Lee, C. W.; Yoon, S., *Chemical Communications* **2011**, *47* (17), 4944-4946.
87. Zhou, Y.; Lee, I.; Lee, C. W.; Park, H. S.; Son, H.; Yoon, S., *Bulletin of the Korean Chemical Society* **2014**, *35* (1), 257-260.
88. Zhou, Y.; Lee, C. W.; Kim, S. K.; Yoon, S., *Ecs Electrochemistry Letters* **2012**, *1* (1), A17-A20.
89. Park, J.; Kim, G. P.; Umh, H. N.; Nam, I.; Park, S.; Kim, Y.; Yi, J., *Journal of Nanoparticle Research* **2013**, *15* (9).
90. .
91. Jo, C.; Hwang, J.; Song, H.; Dao, A. H.; Kim, Y. T.; Lee, S. H.; Hong, S. W.; Yoon, S.; Lee, J., *Advanced Functional Materials* **2013**, *23* (30), 3747-3754.
92. Lim, E.; Kim, H.; Jo, C.; Chun, J.; Ku, K.; Kim, S.; Lee, H. I.; Nam, I. S.; Yoon, S.; Kang, K.; Lee, J., *Acs Nano* **2014**, *8* (9), 8968-8978.
93. Yao, J. Y.; Li, L. X.; Song, H. H.; Liu, C. Y.; Chen, X. H., *Carbon* **2009**, *47* (2), 436-444.
94. Park, J.; Kim, G. P.; Nam, I.; Park, S.; Yi, J., *Nanotechnology* **2013**, *24* (2).
95. Xu, Y. H.; Zhu, Y. J.; Wang, C. S., *Journal of Materials Chemistry A* **2014**, *2* (25), 9751-9757.
96. Chen, Y.; Song, B. H.; Li, M.; Lu, L.; Xue, J. M., *Advanced Functional Materials* **2014**, *24* (3), 319-326.
97. Lin, Y.; Wang, X. Y.; Qian, G.; Watkins, J. J., *Chemistry of Materials* **2014**, *26* (6), 2128-2137.
98. Wang, T. Y.; Peng, Z.; Wang, Y. H.; Tang, J.; Zheng, G. F., *Scientific Reports* **2013**, *3*.
99. Borchardt, L.; Oschatz, M.; Kaskel, S., *Materials Horizons* **2014**, *1* (2), 157-168.
100. Li, H. F.; Wang, R. D.; Cao, R., *Microporous and Mesoporous Materials* **2008**, *111* (1-3), 32-38.
101. Lei, Z.; Sun, X.; Wang, H.; Liu, Z.; Zhao, X. S., *Acs Applied Materials & Interfaces* **2013**, *5* (15), 7501-7508.
102. Toupin, M.; Brousse, T.; Belanger, D., *Chemistry of Materials* **2004**, *16* (16), 3184-3190.
103. Zhu, Y. W.; Murali, S.; Stoller, M. D.; Ganesh, K. J.; Cai, W. W.; Ferreira, P. J.; Pirkle, A.; Wallace, R. M.; Cychosz, K. A.; Thommes, M.; Su, D.; Stach, E. A.; Ruoff, R. S., *Science* **2011**, *332* (6037), 1537-1541.

104. Yang, Z.; Ren, J.; Zhang, Z.; Chen, X.; Guan, G.; Qin, L.; Zhang, Y.; Peng, H., *Chemical Reviews* **2015**, *115* (11), 5159-5223.
105. Snook, G. A.; Kao, P.; Best, A. S., *Journal of Power Sources* **2011**, *196* (1), 1-12.
106. Zhou, H. S.; Zhu, S. M.; Hibino, M.; Honma, I.; Ichihara, M., *Advanced Materials* **2003**, *15* (24), 2107-+.
107. Jung, H. J.; Park, M.; Yoon, Y. G.; Kim, G. B.; Joo, S. K., *Journal of Power Sources* **2003**, *115* (2), 346-351.
108. Liang, Y.; Cai, L.; Chen, L.; Lin, X.; Fu, R.; Zhang, M.; Wu, D., *Nanoscale* **2015**, *7* (9), 3971-3975.
109. Liu, J. P.; Li, Y. Y.; Fan, H. J.; Zhu, Z. H.; Jiang, J.; Ding, R. M.; Hu, Y. Y.; Huang, X. T., *Chemistry of Materials* **2010**, *22* (1), 212-217.
110. Meng, Y.; Gu, D.; Zhang, F. Q.; Shi, Y. F.; Yang, H. F.; Li, Z.; Yu, C. Z.; Tu, B.; Zhao, D. Y., *Angewandte Chemie-International Edition* **2005**, *44* (43), 7053-7059.
111. Kleitz, F.; Choi, S. H.; Ryoo, R., *Chemical Communications* **2003**, (17), 2136-2137.
112. Ryoo, R.; Joo, S. H.; Jun, S., *Journal of Physical Chemistry B* **1999**, *103* (37), 7743-7746.
113. Xiang, D.; Yin, L. W., *Journal of Materials Chemistry* **2012**, *22* (19), 9584-9593.
114. Prasad, K. P. S.; Dhawale, D. S.; Joseph, S.; Anand, C.; Wahab, M. A.; Mano, A.; Sathish, C. I.; Balasubramanian, V. V.; Sivakumar, T.; Vinu, A., *Microporous and Mesoporous Materials* **2013**, *172*, 77-86.
115. Zhu, S. M.; Gu, J. J.; Chen, Z. X.; Dong, J. P.; Liu, X. Y.; Chen, C. X.; Zhang, D., *Journal of Materials Chemistry* **2010**, *20* (24), 5123-5128.
116. Xue, Z. H.; Zhang, F.; Qin, D. D.; Wang, Y. L.; Zhang, J. X.; Liu, J.; Feng, Y. J.; Lu, X. Q., *Carbon* **2014**, *69*, 481-489.
117. Jiang, H.; Ma, J.; Li, C. Z., *Advanced Materials* **2012**, *24* (30), 4197-4202.
118. Philippe, B.; Valvo, M.; Lindgren, F.; Rensmo, H.; Edstrom, K., *Chemistry of Materials* **2014**, *26* (17), 5028-5041; Tucek, J.; Kemp, K. C.; Kim, K. S.; Zboril, R., *Acs Nano* **2014**, *8* (8), 7571-7612; Lin, J.; Raji, A. R. O.; Nan, K. W.; Peng, Z. W.; Yan, Z.; Samuel, E. L. G.; Natelson, D.; Tour, J. M., *Advanced Functional Materials* **2014**, *24* (14), 2044-2048; Yang, Y.; Fan, X. J.; Casillas, G.; Peng, Z. W.; Ruan, G. D.; Wang, G.; Yacaman, M. J.; Tour, J. M., *Acs Nano* **2014**, *8* (4), 3939-3946; Chen, J.; Xu, L. N.; Li, W. Y.; Gou, X. L., *Advanced Materials* **2005**, *17* (5), 582-+; Komaba, S.; Mikumo, T.; Yabuuchi, N.; Ogata, A.; Yoshida, H.; Yamada, Y., *Journal of the Electrochemical Society* **2010**, *157* (1), A60-A65.
119. Zhao, X.; Johnston, C.; Grant, P. S., *Journal of Materials Chemistry* **2009**, *19* (46), 8755-8760.
120. Mu, J. B.; Chen, B.; Guo, Z. C.; Zhang, M. Y.; Zhang, Z. Y.; Zhang, P.; Shao, C. L.; Liu, Y. C., *Nanoscale* **2011**, *3* (12), 5034-5040.
121. Wang, Q. H.; Jiao, L. F.; Du, H. M.; Wang, Y. J.; Yuan, H. T., *Journal of Power Sources* **2014**, *245*, 101-106.
122. Luan, Z. H.; Maes, E. M.; van der Heide, P. A. W.; Zhao, D. Y.; Czernuszewicz,

- R. S.; Kevan, L., *Chemistry of Materials* **1999**, *11* (12), 3680-3686.
123. Kim, T. W.; Kleitz, F.; Paul, B.; Ryoo, R., *Journal of the American Chemical Society* **2005**, *127* (20), 7601-7610.
124. Chambers, S. A.; Kim, Y. J.; Gao, Y., Fe 2p Core-Level Spectra for Pure, Epitaxial  $\alpha$ -Fe<sub>2</sub>O<sub>3</sub>(0001),  $\gamma$ -Fe<sub>2</sub>O<sub>3</sub>(001), and Fe<sub>3</sub>O<sub>4</sub>(001). *Surf. Sci. Spectra*, 1998; Vol. 5, pp 219-228.
125. Corma, A., *Chemical Reviews* **1997**, *97* (6), 2373-2419.
126. Barsoukov, E.; Macdonald, J. R., *Impedance spectroscopy : theory, experiment, and applications*. 2nd ed.; John Wiley: Hoboken, N.J., 2005; p xvii, 595 p; Masarapu, C.; Zeng, H. F.; Hung, K. H.; Wei, B. Q., *Acs Nano* **2009**, *3* (8), 2199-2206; Patel, M.; Wang, X.; Slanac, D.; Ferrer, D.; Dai, S.; Johnston, K.; Stevenson, K., *Journal of Materials Chemistry* **2012**, *22* (7), 3160-3169; Xu, M. W.; Jia, W.; Bao, S. J.; Su, Z.; Dong, B., *Electrochimica Acta* **2010**, *55* (18), 5117-5122; Sun, G. W.; Wang, J. T.; Liu, X. J.; Long, D. H.; Qiao, W. M.; Ling, L. H., *Journal of Physical Chemistry C* **2010**, *114* (43), 18745-18751; Li, R. Z.; Ren, X.; Zhang, F.; Du, C.; Liu, J. P., *Chemical Communications* **2012**, *48* (41), 5010-5012.
127. Bard, A. J.; Faulkner, L. R., *Electrochemical methods : fundamentals and applications*. 2nd ed.; John Wiley: New York, 2001; p xxi, 833 p; Portet, C.; Yushin, G.; Gogotsi, Y., *Carbon* **2007**, *45* (13), 2511-2518.
128. Fischer, A. E.; Saunders, M. P.; Pettigrew, K. A.; Rolison, D. R.; Long, J. W., *Journal of the Electrochemical Society* **2008**, *155* (3), A246-A252.
129. Du, X.; Wang, C.; Chen, M.; Jiao, Y.; Wang, J., *Journal of Physical Chemistry C* **2009**, *113* (6), 2643-2646.
130. Taberna, P. L.; Simon, P.; Fauvarque, J. F., *Journal of the Electrochemical Society* **2003**, *150* (3), A292-A300; Portet, C.; Taberna, P. L.; Simon, P.; Flahaut, E., *Journal of Power Sources* **2005**, *139* (1-2), 371-378.
131. Kim, Y.-H.; Park, S.-J., *Current Applied Physics* **2011**, *11* (3), 462-466.
132. Liu, D.; Wang, X.; Wang, X.; Tian, W.; Liu, J.; Zhi, C.; He, D.; Bando, Y.; Golberg, D., *Journal of Materials Chemistry A* **2013**, *1* (6), 1952-1955.
133. Wang, L.; Zhou, Y.; Qiu, J., *Microporous and Mesoporous Materials* **2013**, *174*, 67-73.
134. Lv, Y.; Zhang, F.; Dou, Y.; Zhai, Y.; Wang, J.; Liu, H.; Xia, Y.; Tu, B.; Zhao, D., *Journal of Materials Chemistry* **2012**, *22* (1), 93-99.
135. Xing, W.; Qiao, S. Z.; Ding, R. G.; Li, F.; Lu, G. Q.; Yan, Z. F.; Cheng, H. M., *Carbon* **2006**, *44* (2), 216-224; Vix-Guterl, C.; Frackowiak, E.; Jurewicz, K.; Friebe, M.; Parmentier, J.; Beguin, F., *Carbon* **2005**, *43* (6), 1293-1302.
136. Xia, K. S.; Gao, Q. M.; Jiang, J. H.; Hu, J., *Carbon* **2008**, *46* (13), 1718-1726.
137. Lang, J.-w.; Yan, X.-b.; Liu, W.-w.; Wang, R.-t.; Xue, Q.-j., *Journal of Power Sources* **2012**, *204*, 220-229.
138. Chen, J.; Huang, K.; Liu, S., *Electrochimica Acta* **2009**, *55* (1), 1-5.
139. Liu, J.; Liu, S.; Zhuang, S.; Wang, X.; Tu, F., *Ionics* **2013**, *19* (9), 1255-1261.
140. Nagarajan, N.; Zhitomirsky, I., *Journal of Applied Electrochemistry* **2006**, *36* (12), 1399-1405.

141. Oh, I.; Kim, M.; Kim, J., *Microelectronics Reliability* **2015**, *55* (1), 114-122.
142. Wang, S. Y.; Ho, K. C.; Kuo, S. L.; Wu, N. L., *Journal of the Electrochemical Society* **2006**, *153* (1), A75-A80.
143. Guan, D.; Gao, Z.; Yang, W.; Wang, J.; Yuan, Y.; Wang, B.; Zhang, M.; Liu, L., *Materials Science and Engineering B-Advanced Functional Solid-State Materials* **2013**, *178* (10), 736-743.
144. Zhang, C.; Xie, Y.; Zhao, M.; Pentecost, A. E.; Ling, Z.; Wang, J.; Long, D.; Ling, L.; Qiao, W., *Acs Applied Materials & Interfaces* **2014**, *6* (12), 9751-9759.
145. Zhi, J.; Wang, Y.; Deng, S.; Hu, A., *Rsc Advances* **2014**, *4* (76), 40296-40300.
146. Kaempgen, M.; Chan, C. K.; Ma, J.; Cui, Y.; Gruner, G., *Nano Letters* **2009**, *9* (5), 1872-1876; Fan, Z. J.; Yan, J.; Zhi, L. J.; Zhang, Q.; Wei, T.; Feng, J.; Zhang, M. L.; Qian, W. Z.; Wei, F., *Advanced Materials* **2010**, *22* (33), 3723-+.
147. Lee, J. W.; Hall, A. S.; Kim, J.-D.; Mallouk, T. E., *Chemistry of Materials* **2012**, *24* (6), 1158-1164; Zhou, X. F.; Liu, W. J.; Yu, X. Y.; Liu, Y. J.; Fang, Y. P.; Klankowski, S.; Yang, Y. Q.; Brown, J. E.; Li, J., *Acs Applied Materials & Interfaces* **2014**, *6* (10), 7434-7443; Chen, S.; Zhu, J. W.; Wu, X. D.; Han, Q. F.; Wang, X., *Acs Nano* **2010**, *4* (5), 2822-2830; Chen, Z.; Augustyn, V.; Wen, J.; Zhang, Y. W.; Shen, M. Q.; Dunn, B.; Lu, Y. F., *Advanced Materials* **2011**, *23* (6), 791-+; Liu, R.; Duay, J.; Lee, S. B., *Chemical Communications* **2011**, *47* (5), 1384-1404; Chou, T. C.; Doong, R. A.; Hu, C. C.; Zhang, B. S.; Su, D. S., *Chemsuschem* **2014**, *7* (3), 841-847.
148. Sassin, M. B.; Mansour, A. N.; Pettigrew, K. A.; Rolison, D. R.; Long, J. W., *Acs Nano* **2010**, *4* (8), 4505-4514.
149. Yang, P. H.; Ding, Y.; Lin, Z. Y.; Chen, Z. W.; Li, Y. Z.; Qiang, P. F.; Ebrahimi, M.; Mai, W. J.; Wong, C. P.; Wang, Z. L., *Nano Letters* **2014**, *14* (2), 731-736.
150. Chen, H. C.; Wang, C. C.; Lu, S. Y., *Journal of Materials Chemistry A* **2014**, *2* (40), 16955-16962.
151. Li, H. Q.; Liu, R. L.; Zhao, D. Y.; Xia, Y. Y., *Carbon* **2007**, *45* (13), 2628-2635.
152. Li, H.; Luo, J.; Zhou, X.; Yu, C.; Xia, Y., *Journal of the Electrochemical Society* **2007**, *154* (8), A731-A736.
153. Wang, D. W.; Li, F.; Liu, M.; Lu, G. Q.; Cheng, H. M., *Journal of Physical Chemistry C* **2008**, *112* (26), 9950-9955.
154. Yang, C. Z.; Li, C. Y. V.; Li, F. J.; Chan, K. Y., *Journal of the Electrochemical Society* **2013**, *160* (4), H271-H278; Li, F. J.; Morris, M.; Chan, K. Y., *Journal of Materials Chemistry* **2011**, *21* (24), 8880-8886.
155. Gao, Z. D.; Zhu, X.; Li, Y. H.; Zhou, X. M.; Song, Y. Y.; Schmuki, P., *Chemical Communications* **2015**, *51* (36), 7614-7617; Wang, K.; Wang, Y.; Wang, Y.; Hosono, E.; Zhou, H., *Journal of Physical Chemistry C* **2009**, *113* (3), 1093-1097; Cao, Y.; Mallouk, T. E., *Chemistry of Materials* **2008**, *20* (16), 5260-5265.
156. Duay, J.; Gillette, E.; Hu, J. K.; Lee, S. B., *Physical Chemistry Chemical Physics* **2013**, *15* (21), 7976-7993.
157. Jang, J.; Bae, J., *Advanced Functional Materials* **2005**, *15* (11), 1877-1882; Alexander, M. R.; Beamson, G.; Bailey, P.; Noakes, T. C. Q.; Skeldon, P.; Thompson, G. E., *Surface and Interface Analysis* **2003**, *35* (8), 649-657; Zheng, M. B.; Cao, J. M.;

- Ke, X. F.; Ji, G. B.; Chen, Y. P.; Shen, K.; Tao, J., *Carbon* **2007**, *45* (5), 1111-1113.
158. Zheng, M.; Ji, G.; Wang, Y.; Cao, J.; Feng, S.; Liao, L.; Du, Q.; Zhang, L.; Ling, Z.; Liu, J.; Yu, T.; Cao, J.; Tao, J., *Chemical Communications* **2009**, (33), 5033-5035.
159. Oh, I.; Kim, M.; Kim, J., *Applied Surface Science* **2015**, *328*, 222-228.
160. Qu, Q.; Yang, S.; Feng, X., *Advanced Materials* **2011**, *23* (46), 5574-+.
161. Xu, L.; Xia, J.; Xu, H.; Yin, S.; Wang, K.; Huang, L.; Wang, L.; Li, H., *Journal of Power Sources* **2014**, *245*, 866-874.
162. Wang, D.; Wang, Q.; Wang, T., *Nanotechnology* **2011**, *22* (13).
163. Wu, M.-S.; Lee, R.-H., *Journal of the Electrochemical Society* **2009**, *156* (9), A737-A743.
164. Lee, K. K.; Deng, S.; Fan, H. M.; Mhaisalkar, S.; Tan, H. R.; Tok, E. S.; Loh, K. P.; Chin, W. S.; Sow, C. H., *Nanoscale* **2012**, *4* (9), 2958-2961.
165. Zhao, X.; Johnston, C.; Crossley, A.; Grant, P. S., *Journal of Materials Chemistry* **2010**, *20* (36), 7637-7644.
166. Wang, L.; Ji, H. M.; Wang, S. S.; Kong, L. J.; Jiang, X. F.; Yang, G., *Nanoscale* **2013**, *5* (9), 3793-3799.
167. Bruce, P. G.; Scrosati, B.; Tarascon, J. M., *Angewandte Chemie-International Edition* **2008**, *47* (16), 2930-2946.
168. Jiang, J.; Li, Y.; Liu, J.; Huang, X.; Yuan, C.; Lou, X. W., *Advanced Materials* **2012**, *24* (38), 5166-5180.
169. Wang, Z.; Zhou, L.; Lou, X. W., *Advanced Materials* **2012**, *24* (14), 1903-1911.
170. Cheng, F. Y.; Liang, J.; Tao, Z. L.; Chen, J., *Advanced Materials* **2011**, *23* (15), 1695-1715.
171. Wang, B.; Chen, J. S.; Wu, H. B.; Wang, Z.; Lou, X. W., *Journal of the American Chemical Society* **2011**, *133* (43), 17146-17148.
172. Nagao, M.; Otani, M.; Tomita, H.; Kanzaki, S.; Yamada, A.; Kanno, R., *Journal of Power Sources* **2011**, *196* (10), 4741-4746.
173. Park, S.-H.; Lee, W.-J., *Scientific Reports* **2015**, *5*; Wang, Y.; Wen, X.; Chen, J.; Wang, S., *Journal of Power Sources* **2015**, *281*, 285-292.
174. Wang, Z. Y.; Luan, D. Y.; Madhavi, S.; Hu, Y.; Lou, X. W., *Energy & Environmental Science* **2012**, *5* (1), 5252-5256.
175. Yu, W. J.; Hou, P. X.; Li, F.; Liu, C., *Journal of Materials Chemistry* **2012**, *22* (27), 13756-13763.
176. Vidano, R. P.; Fischbach, D. B.; Willis, L. J.; Loehr, T. M., *Solid State Communications* **1981**, *39* (2), 341-344.
177. Tuinstra, F.; Koenig, J. L., *Journal of Chemical Physics* **1970**, *53* (3), 1126-&.
178. Sun, C.-F.; Zhu, H.; Okada, M.; Gaskell, K.; Inoue, Y.; Hu, L.; Wang, Y., *Nano Letters* **2015**, *15* (1), 703-708; Sun, C.-F.; Karki, K.; Jia, Z.; Liao, H.; Zhang, Y.; Li, T.; Qi, Y.; Cumings, J.; Rubloff, G. W.; Wang, Y., *Acs Nano* **2013**, *7* (3), 2717-2724.
179. Petkov, V.; Cozzoli, P. D.; Buonsanti, R.; Cingolani, R.; Ren, Y., *Journal of the American Chemical Society* **2009**, *131* (40), 14264-+.
180. Reddy, M. V.; Yu, T.; Sow, C. H.; Shen, Z. X.; Lim, C. T.; Rao, G. V. S.;

- Chowdari, B. V. R., *Advanced Functional Materials* **2007**, *17* (15), 2792-2799.
181. Chou, S.-L.; Wang, J.-Z.; Wexler, D.; Konstantinov, K.; Zhong, C.; Liu, H.-K.; Dou, S.-X., *Journal of Materials Chemistry* **2010**, *20* (11), 2092-2098.
182. Yan, N.; Zhou, X.; Li, Y.; Wang, F.; Zhong, H.; Wang, H.; Chen, Q., *Scientific Reports* **2013**, *3*.
183. Song, R.; Song, H.; Chen, X.; Cui, Y.; Zhou, J.; Zhang, S., *Electrochimica Acta* **2014**, *127*, 186-192.
184. Lahiri, I.; Choi, W., *Critical Reviews in Solid State and Materials Sciences* **2013**, *38* (2), 128-166.
185. Sharma, N.; Plevart, J.; Rao, G. V. S.; Chowdari, B. V. R.; White, T. J., *Chemistry of Materials* **2005**, *17* (18), 4700-4710.
186. Chen, M.; Li, W.; Shen, X.; Diao, G. W., *Acs Applied Materials & Interfaces* **2014**, *6* (6), 4514-4523.
187. Liu, X. H.; Si, W. P.; Zhang, J.; Sun, X. L.; Deng, J. W.; Baunack, S.; Oswald, S.; Liu, L. F.; Yan, C. L.; Schmidt, O. G., *Scientific Reports* **2014**, *4*.
188. Zhou, G. M.; Wang, D. W.; Li, F.; Zhang, L. L.; Li, N.; Wu, Z. S.; Wen, L.; Lu, G. Q.; Cheng, H. M., *Chemistry of Materials* **2010**, *22* (18), 5306-5313; Wu, Y.; Wei, Y.; Wang, J. P.; Jiang, K. L.; Fan, S. S., *Nano Letters* **2013**, *13* (2), 818-823; Wang, H. J.; Liu, S.; Yang, X.; Yuan, R.; Chai, Y. Q., *Journal of Power Sources* **2015**, *276*, 170-175.
189. Lei, C.; Han, F.; Li, D.; Li, W. C.; Sun, Q.; Zhang, X. Q.; Lu, A. H., *Nanoscale* **2013**, *5* (3), 1168-1175; Fei, H. L.; Peng, Z. W.; Li, L.; Yang, Y.; Lu, W.; Samuel, E. L. G.; Fan, X. J.; Tour, J. M., *Nano Research* **2014**, *7* (4), 502-510; Li, X. Y.; Ma, Y. Y.; Qin, L.; Zhang, Z. Y.; Zhang, Z.; Zheng, Y. Z.; Qu, Y. Q., *Journal of Materials Chemistry A* **2015**, *3* (5), 2158-2165.
190. Laruelle, S.; Grugeon, S.; Poizot, P.; Dolle, M.; Dupont, L.; Tarascon, J. M., *Journal of the Electrochemical Society* **2002**, *149* (5), A627-A634; Grugeon, S.; Laruelle, S.; Dupont, L.; Tarascon, J. M., *Solid State Sciences* **2003**, *5* (6), 895-904; Aravindan, V.; Gnanaraj, J.; Madhavi, S.; Liu, H. K., *Chemistry-a European Journal* **2011**, *17* (51), 14326-14346.
191. Hu, Y. Y.; Liu, Z. G.; Nam, K. W.; Borkiewicz, O. J.; Cheng, J.; Hua, X.; Dunstan, M. T.; Yu, X. Q.; Wiaderek, K. M.; Du, L. S.; Chapman, K. W.; Chupas, P. J.; Yang, X. Q.; Grey, C. P., *Nature Materials* **2013**, *12* (12), 1130-1136.
192. Qi, Y.; Guo, H. B.; Hector, L. G.; Timmons, A., *Journal of the Electrochemical Society* **2010**, *157* (5), A558-A566.